A Study of Low-Dimensional Inhomogeneous Systems

Dissertation
zur
Erlangung des Doktorgrades (Dr. rer. nat.)
der
Mathematisch-Naturwissenschaftlichen Fakultät
der
Rheinischen Friedrich-Wilhelms-Universität Bonn

vorgelegt von
Yesenia Arredondo Leon

aus
Mexiko

Bonn, Oktober 2008

Tag der Promotion: 13. Januar 2009
Erscheinungsjahr 2009

Angefertigt mit Genehmigung der Mathematisch-Naturwissenschaftlichen
Fakultät der Rheinischen Friedrich-Wilhelms-Universität Bonn.

Referent: Prof. Dr. Hartmut Monien
Korreferent: Prof. Dr. Herbert Dreiner

Abstract

In the last decades there has been enormous progress in the fabrication of nanoscopic quasi-one-dimensional systems, e.g., carbon nanotubes, semiconducting quantum wires, and conducting organic molecules. These materials have an inhomogeneous composition due to defects, impurities, or because they are formed by several types of atoms. In such systems, the strong electron correlations, inherent to their low-dimensional structure, and large quantum fluctuations induce new and interesting quantum phases, for example superconductivity, quantum Hall edge states, and magnetic ordering.

While the properties of homogeneous one dimensional systems, even with disorder, are relatively well-understood, very little is known about the properties of strongly interacting inhomogeneous systems. Their high-energy physics is determined by the underlying chemistry which, in the atomic scale, introduces Coulomb correlations and local potentials. On the other hand, at large length scales, the physics has to be described by the Tomonaga-Luttinger liquid (TLL) model. In order to establish a connection between the low-energy TLL and the quasi-one-dimensional systems synthesized in the laboratory, we investigate the density-density correlation function in inhomogeneous one-dimensional systems in the asymptotic region. Position dependent on-site Coulomb interaction $U(x)$ and local potentials $V(x)$ are used to model the changes in the local chemistry of the inhomogeneous systems. To investigate homogeneous as well as inhomogeneous systems, we will use the density-matrix renormalization group (DMRG) method.

We will present results for ground state properties, such as the density-density correlation function and the parameter K_c, which characterizes its decay at large distances. Results on some dynamic properties such as spectral density and optical conductivity will be presented as well.

Contents

Introduction

Condensed matter deals with aggregates of units, such as bosons or fermions, subject to interactions with each other, and to internal or external fields. The goal being the understanding of the phases that such interactions induce. The first remark that can be made out of this definition is that the systems of our interest have many degrees of freedom. Next, it is necessary to model the interactions following the rules of the quantum mechanics. Thus, much of the work consists in constructing a Hamiltonian with the desired characteristics of being analytically solvable and encompassing a fully description of the investigated system, which also allows one to make predictions. Such a scenario is still unachievable and we have to settle for simple Hamiltonians for which an analytical solution is not always at hand, and a numerical one is the best we can pursuit of. Even more, such a solution renders a partial understanding of the properties of the system of interest. But sometimes, and for the beginning, this is all which is needed. Surprisingly enough, adequate simplifications have led to plausible, experimental-compatible results. If not all of the degrees of freedom play an essential role and if the particles interact only weakly, simplifications can be made. Examples of this are the P. Drude and A. Sommerfeld and theories of metals in the beginning of the 20th century. Electron-electron interactions were then not considered because a positive-charged cloud surrounding an electron would screen the interaction with its neighbors, transforming an interacting bare electron into a free "dressed" one. The effect of the crystal lattice was taken into account by F. Bloch, who showed that the wavefunction of a particle placed in a periodic potential, like that of a crystal lattice, can be written as the product of a plane wavefunction and a periodic function which has the same periodicity as the potential. All these results being summarized in what is called the *Fermi gas* of free electrons. A step further was taken as L. Landau investigated the effects of electron-electron interactions. The result is the so called *Fermi liquid*, which included interactions (even strong) among the particles, and showed that the description of the system remains analog to that of the Fermi gas if considering *quasiparticles*, which are particle-hole low-energy excitations, instead of (dressed) electrons. Our present understanding of interacting fermionic systems rests still mainly on the Fermi liquid theory.

Phenomena such as high temperature superconductivity, magnetic ordering, Kondo effect, and the fractional quantum Hall effect, which involve inherently strong correlations, have kept the scientific community busy for a while. Whenever possible, the usual approach to deal with many-interacting-particle systems is to start from a non-interacting system and assume that the interactions are weak enough to treat them perturbatively. At some point, this procedure becomes unreliable. Several models have been developed to treat interacting systems. Most of them are based on the structure of the Hubbard model, an elegant description of two competing processes: the hopping of valence electrons from one site of the lattice to another, parameterized by the coupling t, and the local interaction of two electrons sitting in the same site given by the on-site Coulomb potential U. Limiting cases for the ratio U/t, e.g., $U/t \gg 1$, give rise to further interesting models such as the $t-J$ model, in which doubly occupied sites are forbidden, or the spin-1/2 Heisenberg model. The later can be solved exactly by the Bethe Ansatz, which is one of the most celebrated methods to find an analytical solution for the ground state. But even if it allows to obtain exact results, which are not accessible by perturbative methods, it is not possible to calculate correlation functions, which characterize the presence or lack of long-range order in the systems. Access to other properties of many-body interacting systems, such as correlation functions and

low-energy excited states, has been gained through the use of numerical methods. In the case of (quasi) one-dimensional systems, the density-matrix renormalization group (DMRG) developed by S. White has proved to be a powerful method. Its algorithm was originally developed to overcome the problems that arise in one-dimensional interacting systems when standard renormalization group techniques are applied. This method is designed to diagonalize the Hamiltonian of large systems by restricting the basis states to a smaller sector of the Hilbert space.

Condensed matter physics has also being linked to the design and fabrication of new materials, and in this area there has been significant progress. For example in creating low-dimensional systems with interesting electric and magnetic properties, such as carbon nanotubes and quantum wires. The discovery of superconductivity in organic molecules also triggered the investigation of their normal state properties. Finding that such materials are electric conductors with the electrons propagating in a preferred direction, making it an example of a low-dimensional system. Another aspect to be considered is the underlying inhomogeneous chemical composition of these materials, much more complex than simple homogeneous systems such as the Fermi gas. Their chemical composition introduces potential barriers which alter the transport properties drastically. Technically it is important to know how to control the transport and equilibrium properties. Besides, dimensionality profoundly affects the tractability and physical properties of the systems. The strong electron correlations, inherent to the low-dimensional structure, and large quantum fluctuations induce new and interesting quantum phases. In one dimension (1D), the low-energy electronic single-particle excitations posses vanishing spectral weight at the Fermi surface, i.e., there are no quasiparticles present. The physics of such systems, in the homogeneous low-energy regime, is described by the Tomonaga-Luttinger liquid (TLL) model introduced by Haldane[1]. Within this model, it is found that all correlation functions exhibit a power-law decay with the distance, which is specified only by the parameters $K_{c,s}$, where c refers to the charge regime and s to the spin regime.

In this thesis we investigate the properties of one-dimensional strong correlated fermionic systems and study their low-energy physics by means of the TLL theory and the density-matrix renormalization group, which is a reliable method to handle an otherwise exponentially-increasing Hilbert space of a many-body system. This thesis is organized as follows: chapter 1 is devoted to dimensionality effects. We review the concept of dimensionality, and present some examples of the low-dimensional materials obtained in the laboratory and their properties. We also discuss the stability of the Fermi liquid and see that it is no longer suitable to describe low-dimensional systems. For such systems the relevant degrees of freedom are no longer the single particle electronic states but collective spin and charge density waves propagating with different group velocities. This phenomenon is known as *spin-charge separation*. As we already mentioned, the physics of one-dimensional systems, in the homogeneous low-energy regime, is well described by the Tomonaga-Luttinger liquid model, which will be introduced in an intuitive way in chapter 2 and will be solved by means of the method known as *Bosonization* in chapter 3, where the power-law decay of correlation functions will be found in terms of the $K_{c,s}$ parameters. In chapter 4 the Bethe Ansatz solution for the one-dimensional Hubbard model is presented for systems under periodic and open boundary conditions. In this chapter we also introduce the inhomogeneous structures, called *heterostructures*, that we want to study using as well a form of the one-dimensional Hubbard Hamiltonian. Different heterostructures, whose configuration is modeled varying parameters such as the on-site Coulomb potential and introducing local confining potentials, are investigated . By means of the K_c parameter, we want to investigate how valid the TLL is in the inhomogeneous regime. In chapter 5 the density-matrix renormalization group

[1]The Tomonaga-Luttinger liquid is also simply called Luttinger liquid.

method is described in detail. The method has two algorithms, the infinite-size and the finite-size algorithms. The first one lets us grow the system to a desired length. The second one keeps the size of the system fixed, while refining the values of, for example, the ground state energy. Measurement of density-density correlation functions can be then performed and the K_c parameter estimated. The DMRG method allows for calculation not only of static but also of dynamic properties. This is done by implementing the Lanczos vector method to obtain spectral densities, and the correction vector method to calculate, for example, the optical conductivity. Such quantities enable to compare theory to experiment and vice versa. We recall that benchmarks of the TLL are the power law decay of the correlation functions and the spin-charge separation. With this in mind, we present in chapter 6 the results obtained for both homogeneous and inhomogeneous regimes. We will present the density-density correlation function for different heterostructures and discuss the parameters intervals in which a TLL description still holds. The case of systems at half-filling, $k_F = \pi/2$, deserves special treatment, as there is a gap in the charge excitation spectrum. The systems are then insulating. Since in 1D there are no quasiparticles, no peak is expected to appear in the spectral function. Instead, two divergences due to spin-charge separation located at $\pm u_{s,c}q$ ($u_{s,c}$ are the velocities for spin and charge fluctuations, and q is the momentum) have been predicted. However, clear experimental signatures of spin-charge separation are scarce in quasi-one dimensional materials. We will also present results for spectral densities and optical conductivity. A final discussion and outlook will be left for the conclusions chapter.

Parts of this thesis have been published in:

Y. Arredondo and H. Monien, *" Study of the charge correlation function in one-dimensional Hubbard heterostructures"*, Phys. Rev. B **78**, 115425 (2008)

Chapter 1

One-dimensional systems

1.1 Dimensionality

Real materials are in general 3-dimensional. However, when talking about the dimensionality of a system, one emphasizes the lack or presence of a certain anisotropy in the system. In this work, such anisotropy is related to the propagation of the electrons as being constrained to just one direction. Thus, we will consider a material a 1D system if the conduction takes place along one preferred direction. In a first approach, the physics of the electrons can be described in terms of non-interacting electrons in a regular lattice (crystal) in any dimension, as is done within the independent-electron approximation. One possibility to study the effect of dimensionality can be by considering the density of states (DOS) ρ, in 1, 2, and 3 dimensions[1]. The DOS, which counts the discrete energy levels within a unit energy, is given by

$$\rho(E) = 2\frac{V}{(2\pi)^3}\int_{E=E_k} \mathrm{d}\Omega_k \frac{1}{|\nabla_k E_k|}, \tag{1.1}$$

where V stands for volume and $\mathrm{d}\Omega_k$ is an element of volume in momentum space. The integral is done over a surface of fixed energy $E = E_k$, with wavevector k. The 3D, 2D and 1D DOS being:

$$\begin{aligned}
\rho_{3D}(E) &= \frac{V}{\pi^2}k^2\left(\frac{\mathrm{d}E_k}{\mathrm{d}k}\right)^{-1}, \\
\rho_{2D}(E) &= \frac{A}{\pi}k\left(\frac{\mathrm{d}E_k}{\mathrm{d}k}\right)^{-1}, \\
\rho_{1D}(E) &= \frac{L}{\pi}\left(\frac{\mathrm{d}E_k}{\mathrm{d}k}\right)^{-1},
\end{aligned} \tag{1.2}$$

V, A, and L stand for volume, area, and length, respectively. If, as mentioned above, we take a model of (quasi)free-electrons, the energy dispersion relation is given by the parabolic form $E_k = \hbar^2k^2/2m^*$, with $\hbar = h/2\pi$, the reduced Planck's constant, and m^*, the effective mass of the electrons. The resulting DOS for the corresponding dimensions are,

$$\begin{aligned}
\rho_{3D}(E)\mathrm{d}E &= \frac{V}{2\pi^2}\left(\frac{2m^*}{\hbar^2}\right)^{\frac{3}{2}}\sqrt{E}\mathrm{d}E, \\
\rho_{2D}(E)\mathrm{d}E &= \frac{A}{\pi}\left(\frac{2m^*}{\hbar^2}\right)\mathrm{d}E, \\
\rho_{1D}(E)\mathrm{d}E &= \frac{L}{2\pi}\left(\frac{2m^*}{\hbar^2}\right)^{\frac{1}{2}}\frac{\mathrm{d}E}{\sqrt{E}}.
\end{aligned} \tag{1.3}$$

[1] Since we are actually interested in the effects of the reduction of dimensions, we will describe, in the following, the physics starting at 3D moving towards 1D.

We can see in Fig. 1.1 that in 1D the states close to the bottom of the band play a more important role than in 3D, where the higher energy states predominantly contribute to determining the DOS. The effect of the reduction of phase space, which accompanies the reduction of dimensions, is tremendously significant in the physics of materials. This is exemplified also in Fig. 1.1, where the table classifies some of the models for free systems, described by a band structure formalism; and interacting systems, described by the Fermi and Tomonaga-Luttinger liquids. We include in the table examples of the observed phenomena in different dimensions. Changes in the dimensionality introduce as well corresponding boundary conditions, which will eventually generate a specific quantization scheme, for example, in the electronic properties of 2D and 1D systems, as we will discuss in section - 1.3.

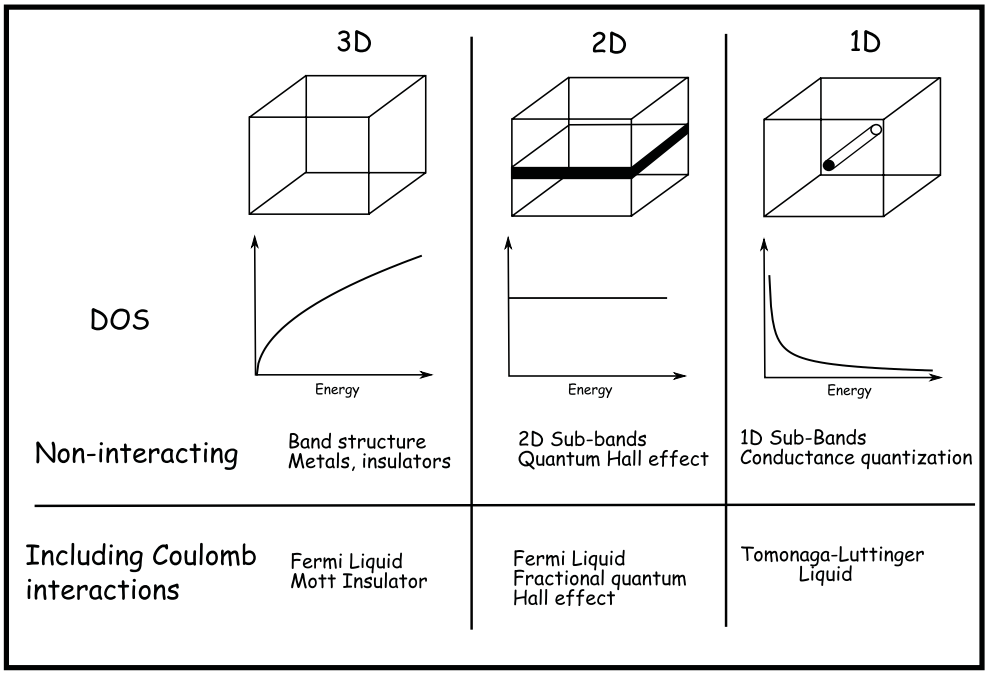

Figure 1.1: Effects on the physics of materials due to the reduction of dimensions.

The dimensionality has a deep impact on the electron-electron interactions. For a 3D electron system, the low energy excitations can be essentially described by weakly interacting quasiparticles, one reason for this is the large phase space available in 3D, which produces a very dilute gas of excitations, the quasiparticles, where the interactions are harmless enough. This is one of the main results of the well-known Fermi liquid theory, which we will discuss in the next section. This idea can also be expressed by stating that electron-electron interactions do not qualitatively change the picture given by the independent-electron approximation. In order to illustrate the role of electron-electron interactions, let us consider the next: In the case of 2D systems as, for example, the 2D electron gases in GaAs heterojunctions, two important phenomena may take place: the integer or the fractional quantum Hall effect, IQHE and FQHE, respectively. This depends on the magnitude of the applied magnetic field ($\mathbf{B}$) perpendicular to the surface of the gas. The application of a magnetic field leads to Landau quantization, and therefore to a discrete energy spectrum $E_{0,N} = E_0 + (N + 1/2)\hbar\omega_c$, with $N = 1, 2, \ldots$ and cyclotron frequency $\omega_c = eB/mc$. The Landau levels are highly degenerate, with filling factor ν, defined as the number of electrons per Landau level. At low magnetic fields ($\leq 10T$) and low temperatures, ν is an integer greater than one, rendering the IQHE. When high magnetic fields are applied ($\approx 20T$), only one Landau level is partially filled, with fractional values for ν,

for which this phenomenon is known as the FQHE. The IQHE can be described by non-interacting quantum mechanics, where the Hamiltonian for a single particle of momentum p_i and vector potential[2] $A(x_i)$ is

$$H_0 = \sum_i^N \frac{\left(\mathrm{p_i} - e\mathrm{A(x_i)}\right)^2}{2m}. \tag{1.4}$$

Since, for the FQHE, the fractional values occurred in the middle of a highly degenerate Landau level, where no gap was apparently present, the observation of the FQHE could not be explained by the same model as the one of Eq. (1.4), therefore it was necessary to include electron-electron interactions,

$$H_{int} = \sum_i^N \frac{\left(\mathrm{p_i} - e\mathrm{A(x_i)}\right)^2}{2m} + \sum_{i<j}^N \frac{e^2}{|x_i - x_j|}. \tag{1.5}$$

In this case, the potential energy $e^2/|x_i - x_j|$ is no longer a small term compared to the cyclotron energy and cannot be neglected, breaking in this way the degeneracy of the lowest Landau level and leading to a well-defined ground state and a gap for excitations, which can be very different as compared to those of bare electrons.

1D electron systems occur in carbon nanotubes, semiconducting wires, and organic conductors. They are promising laboratories to investigate the predicted effects of electron-electron interactions in reduced dimensions. Alone the intuitive picture of electrons aligned in one direction makes the single-particle excitations no longer possible. One electron propagating will definitely "push" its neighbors due to the electron-electron interactions. In this way, single-particle excitations are replaced by *collective* ones. Such collective excitations, which take the form of either spin or charge density waves, are predicted to be dispersing with different group velocities, as opposed to the expected in the Fermi liquid theory. The reduction of phase space in 1D results in a Fermi surface consisting of two points. Furthermore, well-defined low-energy particle-hole excitations are found *only* close to the Fermi surface, thus making a crucial simplification possible, namely the linearization of the fermionic dispersion relation. Another predicted signature of 1D systems is the power-law scaling of correlation functions, which we will study in detail in this thesis. These qualitative properties in the low-energy regime of 1D systems will be formalized in the next chapters as we discuss the Tomonaga-Luttinger model. In the next section we will briefly discuss the Fermi liquid theory for interacting systems and try to understand why this description is not suitable for 1D systems.

1.2 Stability of the Fermi liquid

In the introduction we sketched the development of the understanding of many-particle physics following the different models and methods. These evolved in their degree of difficulty and gained comprehension of the condensed matter physics. This, of course, was by no means a lineal development. The Fermi gas model, which described a homogeneous gas of almost-independently-moving electrons, was followed by the Fermi liquid theory by Landau, which includes the effect of interactions in n-dimensional systems, for $n > 1$. In the ideal Fermi gas, the electrons have a kinetic energy equal to the thermal energy $k_B T$, with k_B the Boltzmann constant and T the temperature. Since one neglects all interactions, the energy levels E of the gas in terms of the single-particle kinetic energies ε_k and of the number n_k of electrons in a single-particle state at energy ε_k are $E = \sum_k n_k \varepsilon_k$. With

[2]Such vector potential is associated to the gauge $A(x_i) = 1/2\ B(y_i - x_i)$, with $\mathbf{B}= B_z$.

the momentum and spin of each electron specified by the label k. Furthermore, the Pauli exclusion principle restricts the values that n_k may take for particles of half-integer spin to $n_k = 0$ or 1 (see the broken line in Fig. 1.2). If we consider a cell of volume V in phase space[3], it can contain at most two electrons with opposite spins, so that in the ground state at $T = 0$ the electrons must have a spread of momenta in a range up to a maximum value p_F, also called the "Fermi momentum". For N electrons with up and down spins inside the volume V –and upon definition of $k_F = p_F/\hbar$ – the density $n = N/V$ can be written as $n = k_F^3/3\pi^2$. The wave number k_F is the radius of a spherical surface, also called the "Fermi surface", and the energy of an electron with momentum corresponding to the Fermi surface is the Fermi energy ε_F. This defines the lowest energy with which one may add a further electron to the gas (ε_F is also referred to as the chemical potential of the gas at $T = 0$). k_F increases with the electron density according to $k_F = (3\pi^2 n)^{1/3}$. The notion of the Fermi sphere, or surface, turns out to be a helpful picture of the ground state and excitations in a Fermi fluid. At $T = 0$, the single-particle states inside the Fermi sphere are fully occupied by the fermions and the states outside are empty. The momentum distribution thus takes a discontinuous change from 1 to 0 as the momentum crosses the Fermi surface. Thermal excitations at finite temperature bring fermions from states inside to states outside the Fermi surface with well-defined momentum k and energy $\epsilon(k)$, leaving "holes" behind and lowering the chemical potential of the gas.

Surprisingly, a number of properties of the free Fermi gas are observed (with modified parameters) when interactions are "switched on" in the system. Landau postulated a one-to-one mapping of the low-energy eigenstates of the interacting electrons to those of the non-interacting Fermi gas. Landau assumed that in a Fermi liquid the net effect of the (short-range) interactions[4] would result in an excited particle "dressed" by a cloud of surrounding particle-hole excitations, building up what is known as a "quasiparticle", with modified inertial mass m^*. The Fermi liquid concept concentrates on the low-temperature regime, i.e., $T < T_F = \varepsilon_F/k_B$ and weakly excited states. One begins by determining the system energy change $\delta E = \sum_{k\sigma} \varepsilon_{k\sigma} \delta n_{k\sigma}$[5], induced by the small density distribution change $\delta n_{k\sigma} = n_{k\sigma} - n^0_{k\sigma} \ll 1$, due to thermal excitations and interactions between particles. $n^0_{k\sigma}$ is the ground state distribution. In this limit the change of energy in the system is given by

$$\begin{aligned} \delta E &= \sum_{k\sigma} \big(\varepsilon_k - \mu\big)\delta n_{k\sigma} + \frac{1}{2} \sum_{kk'\sigma\sigma'} f^{\sigma\sigma'}_{kk'} \delta n_{k\sigma} \delta n_{k'\sigma'} + \dots \\ &\sim \sum_{k\sigma} \left\{ \varepsilon_k - \mu + \frac{1}{2} \sum_{kk'\sigma\sigma'} f^{\sigma\sigma'}_{kk'} \delta n_{k'\sigma'} \right\} \delta n_{k\sigma} \\ &\equiv \sum_{k\sigma} E_{k\sigma} \delta n_{k\sigma}, \end{aligned} \tag{1.6}$$

where $E_{k\sigma}$ is the energy of a quasiparticle and $f^{\sigma\sigma'}_{kk'}$ quantifies the scattering process of a quasiparticle $(k\sigma)$ interacting with another quasiparticle $(k'\sigma')$. Quasiparticles (and holes) are nevertheless approximate eigenstates of the system, and we can estimate their lifetime τ using the Fermi's golden rule to obtain the decay rate of a quasiparticle with energy ε above the Fermi surface at $T = 0$. In such a case we have,

$$\frac{1}{\tau_\varepsilon} = \frac{2\pi}{\hbar} \int_0^\varepsilon \mathrm{d}\omega N(\varepsilon_F)\omega \int_{\omega/\hbar v_F}^{2k_F} \frac{\mathrm{d}k\ k^{d-1} |D(k,\omega)|^2}{(2\pi/L)^d (\hbar v_F k)^2}, \tag{1.7}$$

[3] In general it can be consider a n-dimensional volume but we will usually refer to the $3D$ volume, $V = L^3$.
[4] Unfortunately, the Fermi liquid theory does not work for long-range interactions either.
[5] $\sigma = \downarrow, \uparrow$ is the spin degree of freedom.

with $N(\varepsilon_F)$ the density of states at the Fermi surface and v_F the Fermi velocity. The integral over ω accounts for the number of possible hole excitations that can be created, and $D(k,\omega)$ is the matrix element for the scattering process[6]. Thus in 3D, the lifetime is given by

$$\begin{aligned}\frac{1}{\tau_\varepsilon} &= \frac{2\pi}{\hbar}\sum_f |V_{if}|^2\delta(\varepsilon-\varepsilon_F) \\ &\sim \frac{\pi}{\hbar}|V|^2 N(\varepsilon_F)^3\varepsilon^2,\end{aligned} \tag{1.8}$$

where the sum is performed over the possible final states and $|V_{if}|$ are the scattering matrix elements (considered constant) between the initial (i) and final (f) states. From this result one concludes that, close to the Fermi surface where ε is small, the quasiparticle is always well-defined since its decay rate ($\propto \varepsilon^2$) is much smaller than its excitation energy (ε). From Eq. (1.7) we see that in 1D, even for a constant $D(k,\omega)$, the decay is proportional to ε, i.e., there is no limit where the quasiparticle energy is well-defined, thus there are no 1D-Fermi liquids.

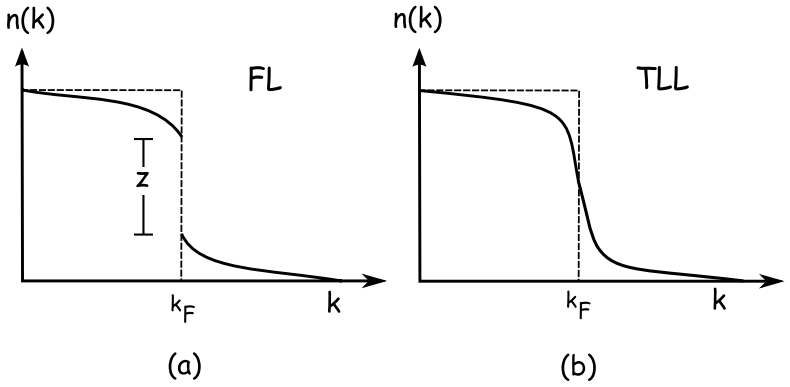

Figure 1.2: Single-particle momentum distribution $n_\sigma(k)$ at $T=0$. (a) For electrons in a Fermi liquid. The discontinuity at the Fermi energy ε_F is of magnitude $z<1$. (b) The absence of a discontinuity in a 1D, interacting system signalizes the lack of quasiparticles. The broken line shows the discontinuity in the case of a free Fermi gas.

When dealing with quasiparticles rather than with bare electrons, the excitations of the system can be described as an ideal gas of free quasiparticles. Furthermore, such quasiparticles obey Fermi statistics, so that at low-temperature the low-lying excited states can be described in terms of the excitation of the quasiparticles across the Fermi surface, still finding a discontinuity at this point, though with an amplitude $z<1$, as it was the case for the free gas of electrons[7] (see Fig. 1.2). For a free fermion gas the one-particle Green's function has a pole on the real axis describing the one-particle excitation of well-defined energy $\varepsilon_0(k)$:

$$G(k,\omega) = \frac{1}{\omega-\varepsilon_0(k)+i\delta}. \tag{1.9}$$

[6] In this form, the integral is also independent of the direction of the momentum. The integration resulted precisely in the term $(\hbar\nu_F k)^2$.

[7] Giamarchi refers in his book to this amplitude as the one related to "the 'fraction' of the electrons that remains in this quasiparticle state." [13].

When interactions are switched on, the Green's function specifies the many-body effects by including the self-energy term $\Sigma(k,\omega)$,

$$G(k,\omega) = \frac{1}{\omega + i\delta - \varepsilon_0(k) - \Sigma(k,\omega)}. \tag{1.10}$$

Then, the Fermi liquid is characterized by a solution which is a pole of finite residue

$$z^{-1} = 1 - \left.\frac{\partial \Sigma}{\partial \omega}\right|_{\substack{\omega=0 \\ k=k_F}} \leq 1, \tag{1.11}$$

with the amplitude of z_k giving the magnitude of the discontinuity of the momentum distribution at the Fermi surface. z_k can be considered as the order parameter of the Fermi liquid. The failure in 1D of the Fermi liquid appears in the form of a continuous momentum distribution function, meaning that no single-quasiparticle excitations are to be found, and another description has to be introduced for 1D systems.

1.3 Quasi-one-dimensional systems in the laboratory

A couple of decades ago, the observation of low-dimensional effects was not possible due to the lack of suitable 1D materials. By now, novel material processes have successfully created a palette of quasi-one-dimensional structures. There one can explore electron transport among other effects. A comprehension of such devices, on both levels theoretical and experimental, is a quite ambitious project with promising applications in the new fields of nanotechnology and spintronics. In the rest of this chapter we want to introduce three examples of 1D systems and briefly describe their structure and other known properties.

1.3.1 Carbon nanotubes

Carbon nanotubes were discovered in 1991 by Iijima in the form of multi-walled carbon nanotubes (MWNT) [17]. The basic constituent of carbon nanotubes are graphite layers, which are 2D honeycomb lattices made up of carbon atoms, wrapped to form a cylinder. A single graphite layer is also called *graphene*. A typical radius is $1-2$ nm and a typical length is of the order of several microns (see Fig. 1.3 a). Single-walled carbon nanotubes (SWNT) were observed also by Iijima [18] and independently by Bethune [5] [8] (see Fig. 1.3 b). In this thesis we will concentrate on the so-called *defect free* nanotubes, i.e., tubes formed with graphite layers whose network is only hexagonal. Topological defects such as pentagons and heptagons in the lattice are unavoidable in the case of bent, branched or capped nanotubes. A SWNT can be uniquely characterized by a vector $\mathbf{C}$ in terms of a set of two integers (n,m) corresponding to graphene vectors $\mathbf{a}$ and $\mathbf{b}$ (see Fig. 1.4), with $\mathbf{C} = n\mathbf{a} + m\mathbf{b}$, and $a = |\mathbf{a}| = |\mathbf{b}|$ the lattice constant of the graphene. A SWNT is constructed by rolling up the graphene sheet such that the two extremes of the vector $\mathbf{C}$ are superimposed. If $m = n$, the tubes are called *armchair tubes*, if $m = 0$, they are *zigzag tubes*. A third structure is the one with $n > m > 0$, called *chiral tubes*. In general, these structures can be characterized by the chiral angle θ defined as

$$\cos(\theta) = \frac{m + 2n}{2\sqrt{n^2 + m^2 + nm}}. \tag{1.12}$$

[8] Chronologically, there is record of previous work done by M. Endo and A. Oberlin who reported on the observation of what was most probably multi-walled carbon nanotubes in 1976, although for the time being it was not clear for them what it meant.

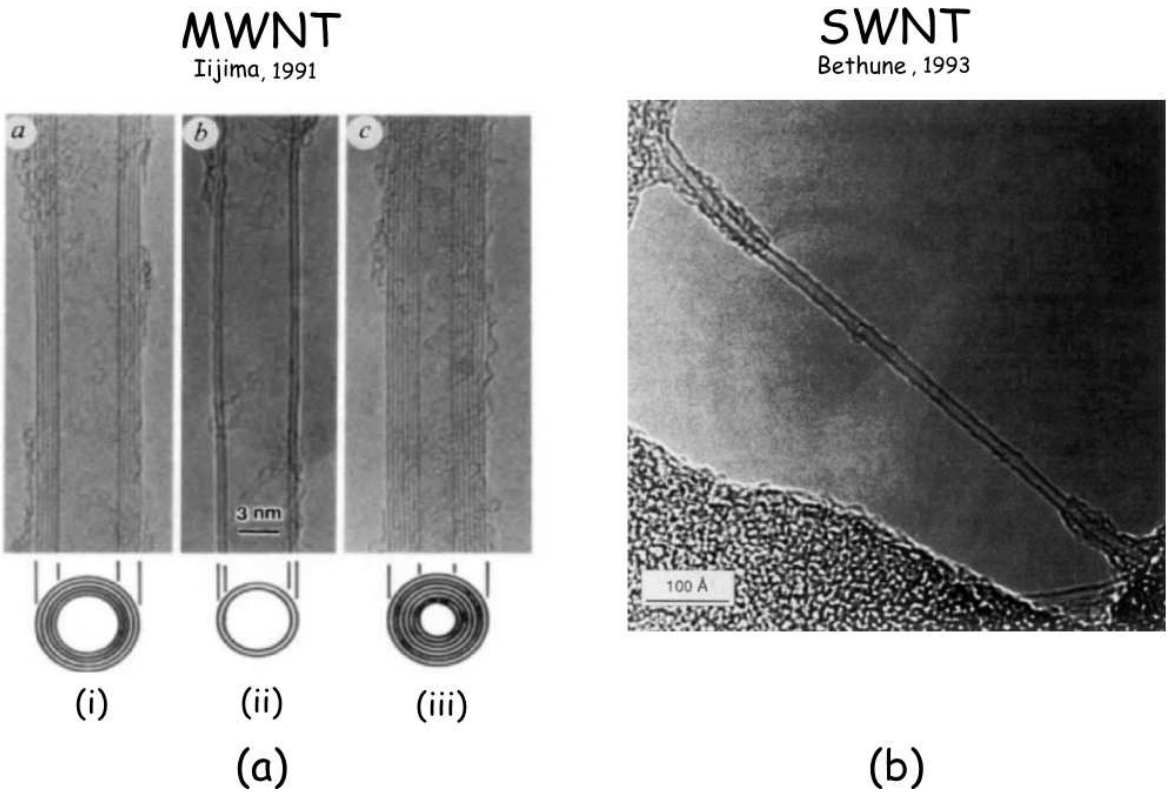

Figure 1.3: (a) High resolution electron micrograph of homogeneous multiwalled nanotubes consisting of five (i), two (ii), and seven (iii) graphene sheets. With cross sections of diameter between 5.5 and 6.7nm [17]. (b) TEM image of single-walled nanotube of diameter ∼1.2nm [5].

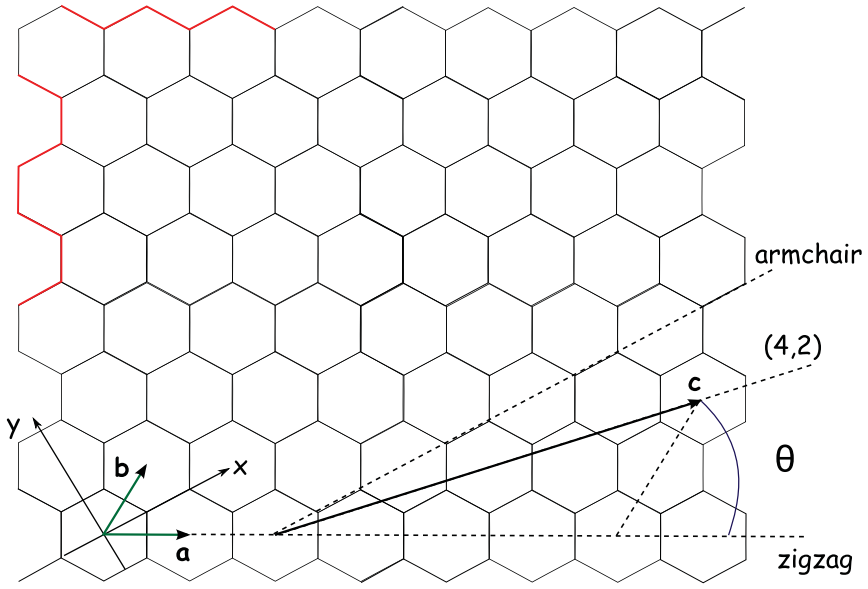

Figure 1.4: Unrolled honeycomb lattice (graphene sheet). The vectors **a** and **b** form the unit cell of graphene. A nanotube (n,m) forms by rolling the graphene sheet along the chiral vector $\mathbf{C} = n\mathbf{a} + m\mathbf{b}$. The nanotube can be also characterized by the diameter $|\mathbf{C}|$ and the chiral angle θ with respect to the zigzag axis. The diagram is constructed for a (4,2) nanotube.

the angle θ ranges from 0 for zigzag tubes, to a maximum of 30° for $n = m$ (armchair tubes). In Fig. 1.5 and Fig. 1.6 we show examples of nanotube models. The importance of the direction of the rolling is emphasized by the fact that it determines if the nanotube will be metallic or semiconducting. When the graphene is rolled over to form the nanotube, periodic boundary conditions are imposed, quantizing in this way the two-dimensional vector $\mathbf{k}$ according to $\mathbf{k} \cdot \mathbf{C} = 2\pi n$, where n is an integer. If the wavevector is expressed as the sum of a component along the tube circumference, $\mathbf{k}_\perp$, and a component in the direction $\mathbf{z}$ of the tube, $\mathbf{k}_z$, the boundary condition results in the quantization condition $\mathbf{k}_\perp = 2\pi n$, whereas the wavevector $\mathbf{k}_z$ remains a continuous variable (see Fig. 1.7). From this, we can classify the electronic properties of the nanotubes in terms of the parameters n and m. If $n - m = 3q$, i.e., for zigzag nanotubes, the dispersion close to the Fermi level has a gap, thus the tubes correspond to small-gap semiconductors. If $n = m$, i.e, in the case of the armchair nanotubes, the band structure can be approximated by a linear dispersion close to the Fermi level. The system is then metallic. All other combinations of n, m turn out to be large-gap semiconductors. If the material is metallic, ballistic conductance is observed with the value of $4e^2/h$ at low temperatures. The mean-free path in this case corresponds to a room temperature resistivity of the order of 10^{-6}cm. This means that the conductivity of metallic nanotubes is at least as good as the conductivity of the best metals at room temperature. The main reason for this is the reduced phase space for scattering due to acoustic phonons. In higher dimensions the scattering events eventually reverse the direction of the electrons, which is not possible in 1D, where the only direction left to propagate is forwards or backwards, making carbon nanotubes excellent laboratories to investigate the motion of electrons in one dimension. The semiconducting behavior in the nanotubes has also been reported, showing that the nanotube conducts at negative values of the gate voltage and turns off when positive voltage is applied. The resistance changes between the on and off state over many orders of magnitude. Such behavior is analogous to that of a metal-oxide-semiconductor transistor, with the carbon nanotube as a one-dimensional analog of the two-dimensional device.

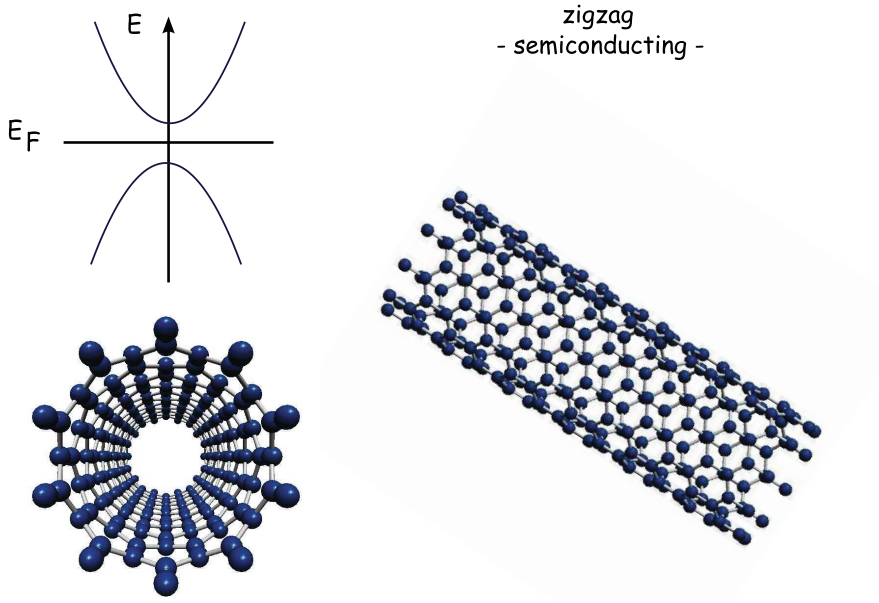

Figure 1.5: Zigzag structure of a nanotube with chirality indices (10,0). The material is in this case semiconducting.

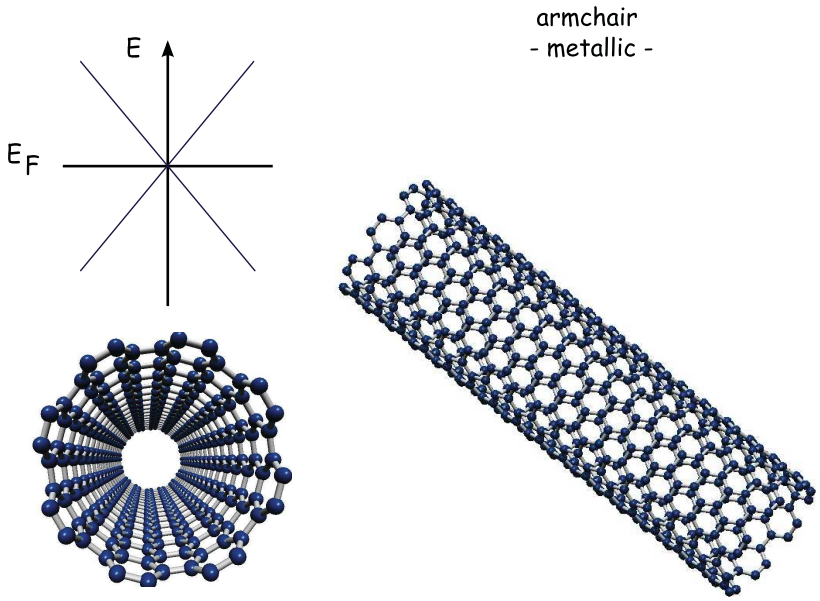

Figure 1.6: Armchair structure of a nanotube with chirality indices (8,8). The material is in this case metallic.

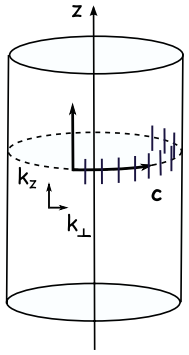

Figure 1.7: Carbon nanotubes can be represented by a cylinder built on the chiral vector **C**. While the wavevector k_z along the tube axis (z) takes continuous values, the wavevector $k_\perp$ along the tube circumference can only take discrete values.

The extremely small size and highly symmetric structure of the nanotubes are the underlying reason for their interesting properties. The electronic properties of a nanotube are inherited from those of the graphene, for which the dispersion relation[9] as a function of the wavevector $\mathbf{k} = (k_x, k_y)$ is

$$E(k_x, k_y) = \pm t\Big[1 + 4\cos\big(\frac{\sqrt{3}k_x a}{2}\big)\cos\big(\frac{k_y a}{2}\big) + 4\cos^2\big(\frac{k_y a}{2}\big)\Big]^{\frac{1}{2}}, \tag{1.13}$$

here t is the nearest-neighbor hopping parameter and a is the lattice constant. Examples for these parameters are $t = 2.5 - 3.2$ eV and $a = 0.246$ nm. Carbon nanotubes are often seen as straight or elastic bending structures by transmission electron microscopy (TEM), scanning electron microscopy (SEM), atomic force microscopy (AFM), and scanning tunneling microscopy (STM). To study their structural features techniques have been employed such

[9] Obtained using a tight-binding model, which is the simplest one that one can handle.

as electron diffraction (EDR), x-ray diffraction (XRD), and Raman spectroscopy, among others [8, 1].

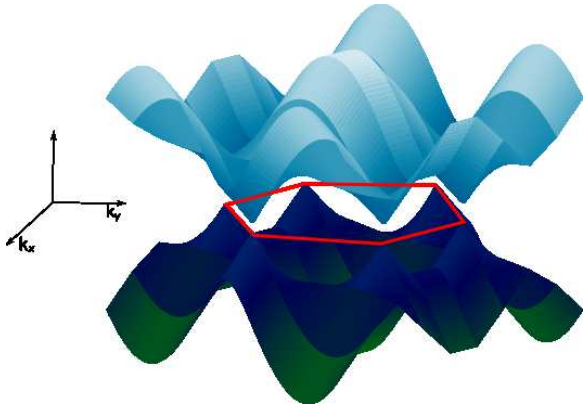

Figure 1.8: Dispersion relation of graphene in the k_x, k_y plane as given by Eq. (1.13).

A Luttinger liquid behavior in nanotubes has been reported on bundles of nanotubes by Bockrath [6] and on single nanotubes by Yao [54]. Both works support the prediction of the Luttinger liquid theory, predicting that the differential conductance scales as a power law. From Bockrath, the differential conductance was fitted using

$$\frac{\mathrm{d}I}{\mathrm{d}V} = AT^{\alpha} \sinh\left(\frac{eV}{2k_BT}\right)\left|\Gamma\left(\frac{1+\alpha}{2}+\gamma\frac{ieV}{2\pi k_BT}\right)\right|^2, \tag{1.14}$$

with $\Gamma(x)$ the gamma function, γ is a fitting parameter related to the choice of the contacts between the ropes (bulk- or end-contacted), and A is a constant. In Fig. 1.9, the results of both workgroups are shown. In the work by Yao et al, heterostructures of the type metal-metal and metal-semiconductor were fabricated by introducing defects in the graphene sheet.

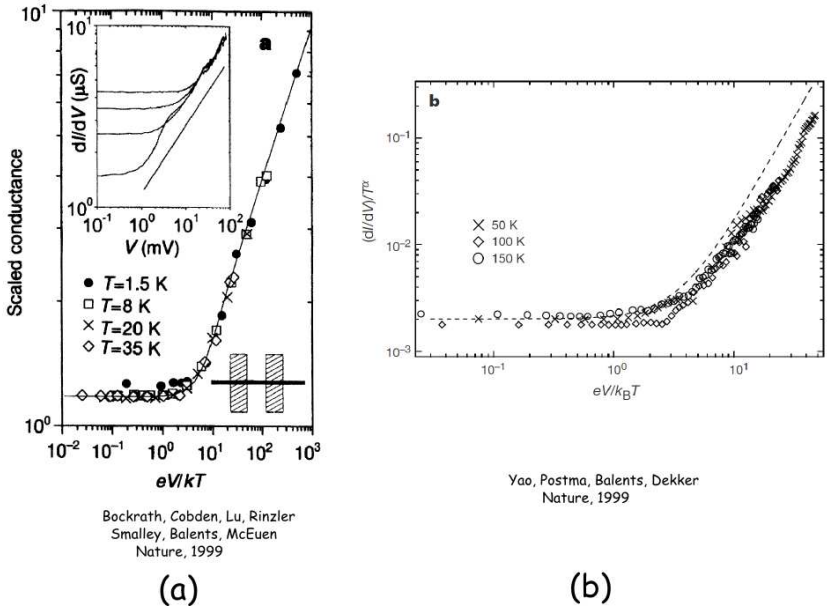

Figure 1.9: By dividing Eq. (1.14) between T^{α}, the remainder is a function of eV/k_BT. (a) Differential conductance for a bulk-contacted tube for different temperatures. The inset shows results for $T = 1.6K, 8K, 20K$ and $35K$, where the straight line on a log-log plot is a guide to the eye to indicate the power law behavior. The graph was taken from Bockrath [6]. (b) Results by Yao [54] showing the universal feature of the differential conductance in carbon nanotubes.

1.3.2 Quantum wires

The success in growing layered semiconducting 2D devices boosted the creation of low-dimensional systems. These 2D devices, whose basic structure is sketched in Fig. 1.10, are based on aluminum-gallium-arsenide (AlGaAs) and gallium-arsenide (GaAs) layers stacked along the vertical direction. They are, in general, denoted as AlGaAs/GaAs heterojunctions. Layers of AlGaAs, usually doped with silicon (Si), trap a much thinner layer of GaAs and confine the carriers in this region, therefore the GaAs is commonly called a quantum well, i.e., a realization of a 2D electron gas (2DEG). Fabricated using molecular beam epitaxy (MBE), these structures show an electron mobility of the order of $10^6 \mathrm{cm}^2/\mathrm{Vs}$, and serve as basis for the fabrication of 1D wires. The use of the carrier spin as an additional degree of freedom in semiconducting devices, with their electronic properties depending on external magnetic fields, has open up a new branch of electronics called "spintronics". In this section we will briefly describe some examples of quantum wires: cleaved edge wires, split gate devices, and V groove wires.

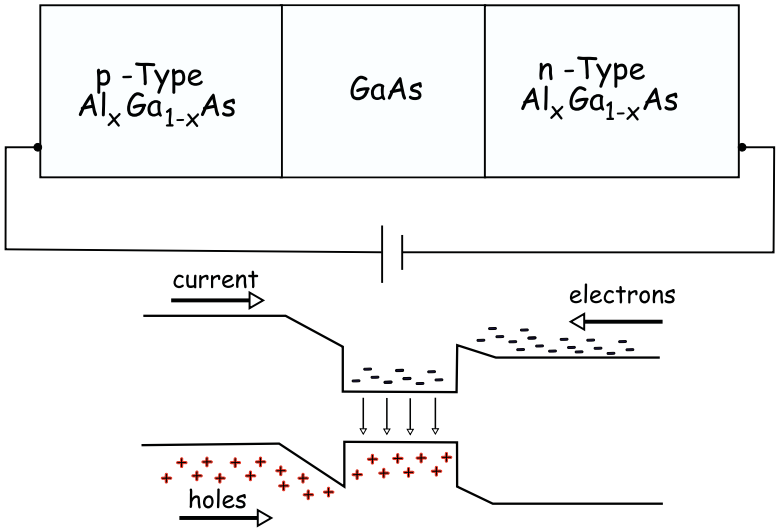

Figure 1.10: Semiconducting device designed to confine the charge carriers in the *active* region, the GaAs region. The active region is sandwiched by the barrier regions of AlGaAs, which have wider band gaps than the active region and are oppositely doped to inject electrons and holes separately.

Cleaved edge wires.- The sample basic preparation consists of a GaAs base and a first overgrowing of an AlGaAs wafer (of a few hundred microns) [28]. Over the AlGaAs layer a thin doped GaAs layer ($14 - 40\mu$m thick) is grown, followed by a second doped AlGaAs layer. The result is a 2DEG along the embedded GaAs layer, with electron mobility of the order of $10^6 \mathrm{cm}^2/\mathrm{Vs}$. On top of this, a long and narrow tungsten stripe (tungsten gate T, see Figs. 1.11 a,b) is evaporated. This stripe separates the 2DEG into two halves that act as source and drain contacts to the wire. It will also determine the length of the wire, 1μm-20μm. In order to provide the cleanest possible surface (edge) on which to proceed with further epitaxial growth, the former structure is to be cleaved in ultra high vacuum using a thallium (Ta) metal bar. After cleaving, a doped AlGaAs setback is grown on the cleaved plane, which will introduce electrons at the edge of the GaAs surface. Over this, a final cap of Ti-Au is deposited, which will serve as a side gate (S) to increase the carrier density in the wire. With a gate voltage $V_T = 0$, the 2DEG is continuous and the 2D contact areas are not yet separated (see Fig. 1.11 d). For a negative voltage $V_T = V_D$, called the depletion voltage, the top gate has separated the contact area but the connecting wire remains weakly confined. For even more negative values of V_T the 1D wire is well developed and completely confined: by the GaAs surface in the **z** direction, and by the strong potential in the **y** direction (see Figs. 1.11 e,f). The quantization of the conductance

has been clearly observed in the laboratory and some results are shown in Fig. 1.12 [53].

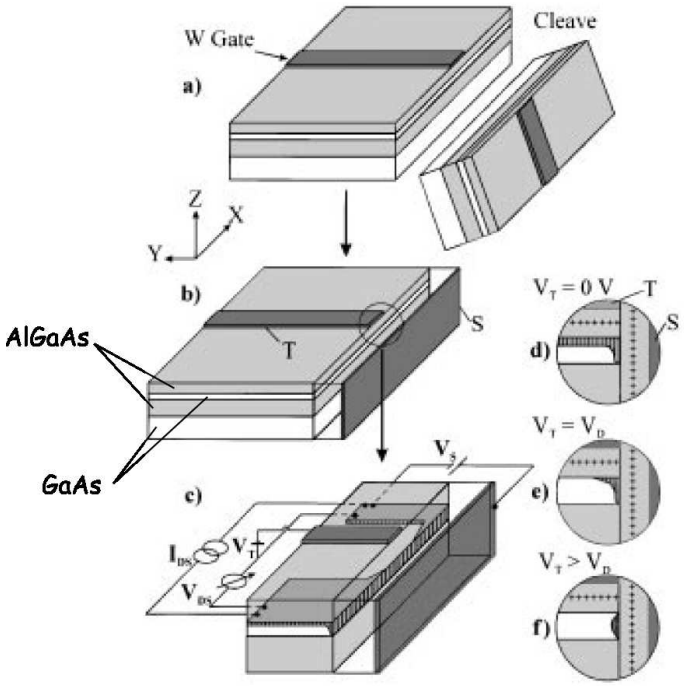

Figure 1.11: Cleaved edge wire geometry and set up for measurements. The figure was taken from [53]. Extra labels were introduced to clarify the structure of the device. (a) Sample geometry with long and narrow tungsten stripe (T). (b) After cleaving, a doped AlGaAs is grown along the 110 direction (transparent layer). A Ti-Au gate (S) is deposited over the entire 110 surface. (c) The top gate (T) is biased to deplete the 2DEG underneath, leaving only the wire as a possible channel. (d) Cross section through the YZ plane in the wire region for unbiased conditions. The 2DEG is coupled directly to the electrons along the cleaved edge. (e) The 2DEG is depleted by the top gate. (f) For larger (negative) values of the top gate the wire confinement improves.

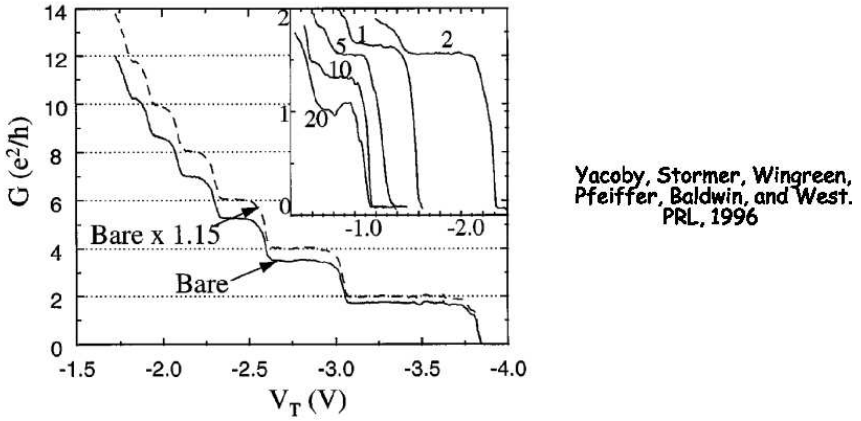

Figure 1.12: Linear response conductance of a 2 μm long wire in a 25 nm quantum well vs the top-gate voltage (V_T) measured at a temperature of 0.3 K. The solid line is the measured conductance. The dashed curve is the measured conductance multiplied by an empirical factor of 1.15. Inset: Linear response conductance of the last plateau for wires of different lengths fabricated consecutively along the edge of a single 25 nm cleaved edge overgrowth specimen. The numbers denote the wire length in microns.

Split gate devices.- A split gate device consists of a GaAs/AlGaAs heterostructure, where the later one is doped. The heterostructure is grown by MBE. The material serving as gate, for example gold, is deposited by electron-beam lithography, followed by thermal evaporation on top of the heterostructure in the form of a stripe of a length L of a few μm, and with the particular characteristic that it has a gap of width $W < 0.5$ μm. Under

application of a negative voltage to the two gates, the 2DEG formed on the GaAs is depleted of electrons and current flows then through the narrow region not covered by the gate metal. If the elastic mean free path l_e is much greater than W or L, the transport through the 1D channel is ballistic and the conductance is quantized in units of $2e^2/h$. Some results for this are shown in Fig. 1.13 [44].

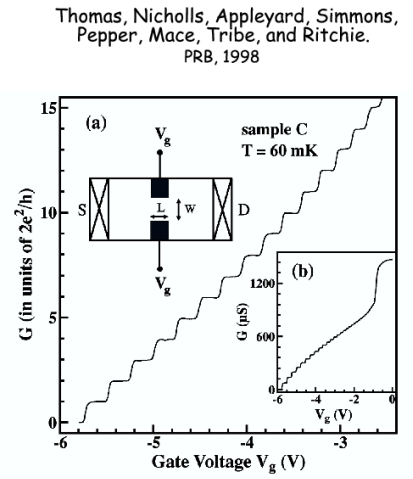

Figure 1.13: Conductance quantization in a split-gate wire as function of the gate voltage. The inset (a) shows a diagram of the device. D and S stand for *drain* and *source*, respectively. In (b) the raw data is plotted against the gate voltage.

V groove wires.- The V groove wires take their name from the corrugated pattern on which the GaAs/AlGaAs heterostructure is deposited [48]. The basic layer is an undoped (100)GaAs substrate patterned with a 3μm-pitch grating, with grooves ($\sim 2\mu$m deep) oriented along the $[00\bar{1}]$ direction, made by chemical etching. The layer structure consists of a Si-doped AlGaAs layer (24-50 μm) followed by one or several thin (2-5 μm) GaAs quantum wells, separated also by Si-doped AlGaAs barrier layers (see Fig. 1.14). The structure is grown using the method called organometallic chemical vapor deposition (OMCVP) - under conditions of ambient pressure or under low pressure (~ 1 μbar). The results are 2DEGs on planar GaAs as well as on the sidewall of the corrugated structure, with mobility values of the order of $10^5 \mathrm{cm}^2/\mathrm{Vs}$. The 1D (crescent-shaped) quantum wire is created at the bottom of the groove, due to both the groove sharpening during the AlGaAs growth and segregation of the Ga species on the bottom of the groove. The cross-section of the heterostructure has been captured in TEM images (see Fig. 1.15).

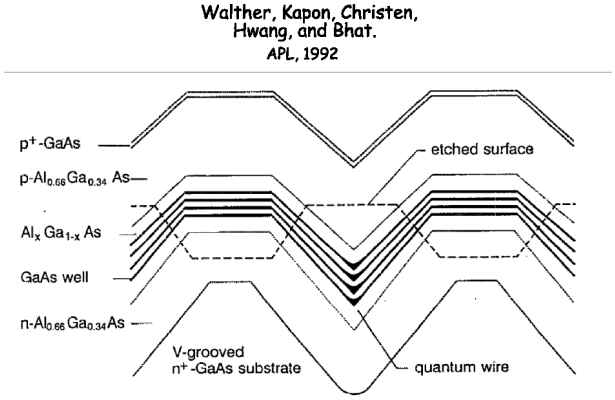

Figure 1.14: Schematic view of a V-groove wire growth. The broken line indicates the surface after etching [48].

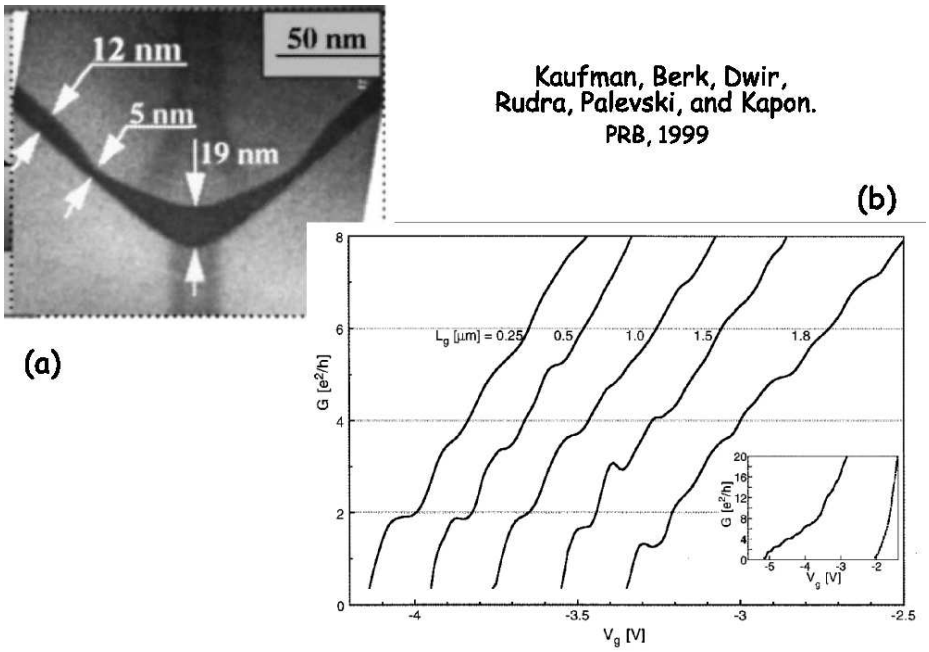

Figure 1.15: (a) Cross-sectional TEM images of a quantum wire with a nominal thickness of 12μm. (b) Conductance vs. gate voltage for different values of L_g, the gate width, with wire thicknes $t = 26$nm. The inset shows the conductance vs. gate voltage for a wire of thickness $t = 21$nm and $L_g = 0.5\mu$m [22].

Hints of the Luttinger liquid behavior on quantum wires have tried to be observed in the form of a power law, like in the case of the carbon nanotubes, or by expecting the group velocities of collective spin and charge modes to be different as predicted by the Luttinger theory. Examples of the effect of the Coulomb interaction in 1D have been found in a change in the quantized conductance as a function of the temperature when the length of the wire is increased [43], and in weakly disordered V-groove wires [23].

1.3.3 Organic conductors

The search for molecular conductors lead to the synthesis of organic salts, one of whose most representative group is the one of the Bechgaard salts [10] $(TMTSF)_2X$, where X is an inorganic anion with several possible symetries: spherical (PF_6, AsF_6, SbF_6, TaF_6), tetrahedral (BF_4, ClO_4, ReO_4), or triangular (NO_3). These compounds were the first of their class to exhibit superconductivity. This was first dicovered in $(TMTSF)_2FS_6$ at 0.9K under a pressure of 12kbar in 1979 by Jérome, Mazaud, and Ribault in Paris, and independently by Bechgaard in Copenhagen [21]. Superconductivity is only one of many complex and interesting features grabbing the attention of both experimenters and theoreticians. Their varied phase diagram at very low temperatures includes Peierls transition, antiferromagnetism, spin-density waves, superconductivity, and a less clear, non-Fermi liquid phase. At ambient pressure, the material shows a Mott-insulator transition. These phases have been unified in the diagram shown in Fig. 1.16 for several TMTSF compounds by C. Bourbonaiss and D. Jérome [7].

[10] The compund full name is tetramethyltetraselenefulvalene.

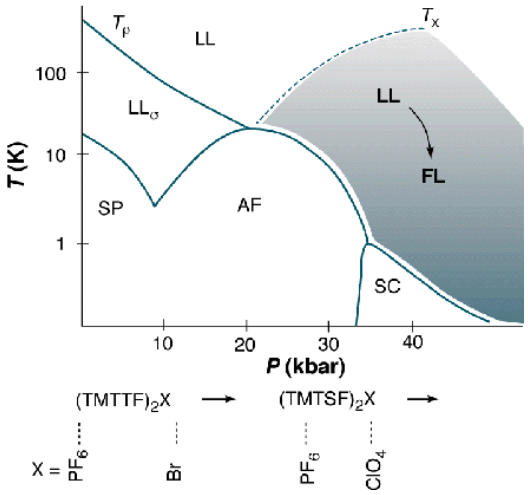

Figure 1.16: Phase diagram of TMTSF compounds [7]. MI: Mott insulator, LL: Luttinger liquid, FL: Fermi liquid, SP: spin Peierls, AF: antiferromagnetic spin-density wave, SC: superconducting.

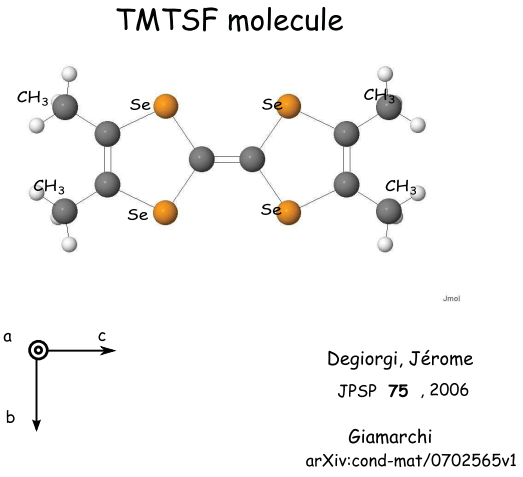

Figure 1.17: Organic molecule basic element, the tetramethyltetraselenefulvalene (TMTSF) molecule.

These organic molecules are composed of linear stacks of TMTSF positive ions (see Fig. 1.17) arranged into planes separated by X anions, which stabilize the structure and allow for charge transfer between TMTSF and X to provide charge neutrality to the whole molecule (see Fig. 1.18). The lattice vectors are not orthogonal but one can distinguish a vertical axis **a** along the stacks, a horizontal axis **b** in the TMTSF planes, and a **c** axis pointing out of the planes. Considering the hopping of electrons in these three directions, it was found that the compound is highly anisotropic at room temperature, with hopping values 1000K:100K:30K in the **a**, **b**, and **c** direction, respectively. The reason for this is that the π orbitals of the selenium overlap along the stacking direction. This makes these systems quasi-one dimensional. And with one ion for two TMTSF molecules the chains are quarter-filled. Furthermore, this concentration cannot be modified under pressure. A direct proof of a Luttinger behavior has been found in these compounds. Measurements of the **a**-axis optical conductivity by Schwartz show clearly a power law decay shown in Fig. 1.19 [35].

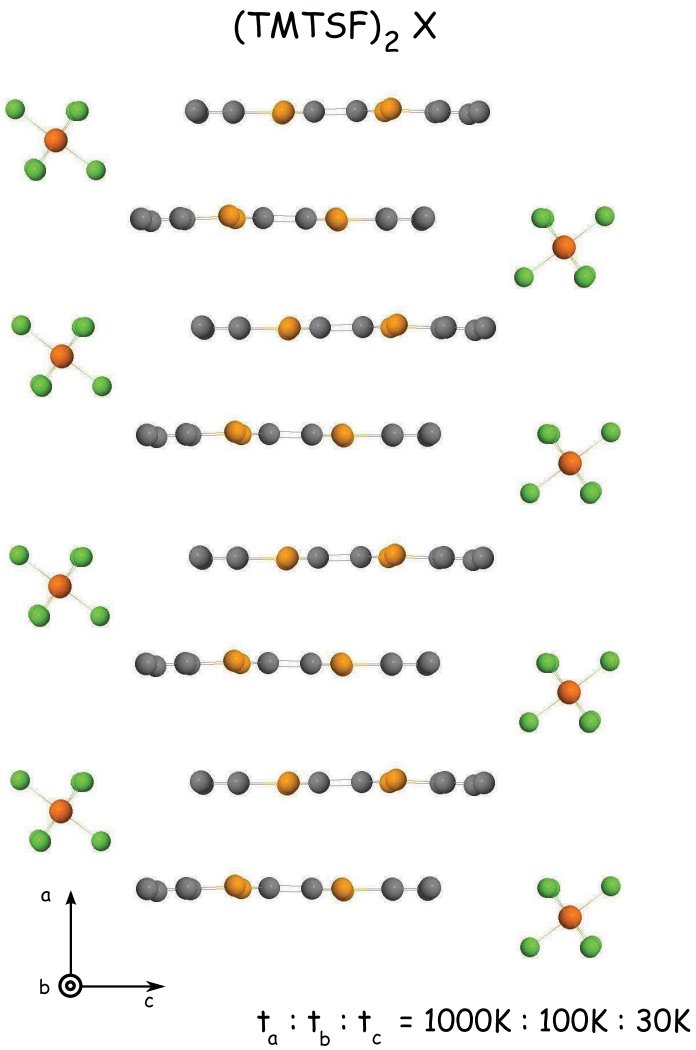

Figure 1.18: Organic conducting molecule formed by stacking of TMTSF planes separated by anions X. t_a, t_b, and t_c are the hopping energies in the **a**, **b**, and **c** direction, respectively.

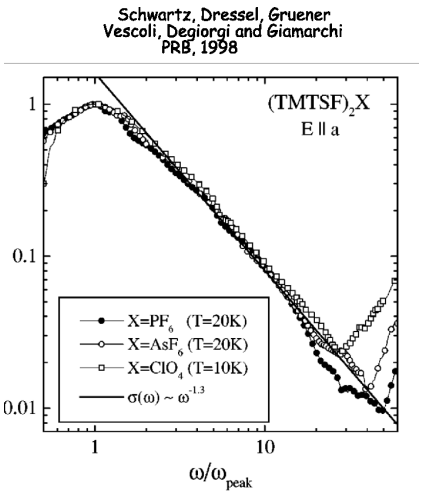

Figure 1.19: Optical conductivity for different TMTSF compounds as measured by Schwartz et al [35]. The solid line corresponds to a fit of the form $\sigma(\omega) \sim \omega^{-\nu}$, with $\nu = 1.3 \leq 0.1$.

Summary

In this chapter we discussed the concept of dimensionality of materials not only in terms of the spatial dimensions but also in terms of the possible restrictions on the propagation of conducting electrons. The conductivity can be confined to a plane or even to a line. In the last case, we call the material a one dimensional material. One-dimensional systems imply strong correlations between the particles. Therefore, we turned to the Fermi liquid model for interacting systems and found out that it describes accurately high-dimensional systems but for D=1 the model fails because the spectral weight vanishes at the Fermi surface. The physics of such systems, in the homogeneous low-energy regime, is well described by the Tomonaga-Luttinger liquid model, which predicted that all correlation functions exhibit a power-law decay with the distance. The Tomonaga-Luttinger liquid will be the subject of the following chapters. We also presented examples of quasi-one dimensional materials such as carbon nanotubes, quantum wires, and organic conductors. We described some of their properties and commented the possible observation of TLL behavior.

Chapter 2

Tomonaga-Luttinger liquid

In the previous chapter we discussed the effect of a reduced dimensionality on the physical properties of fermionic systems, from which a reduction of the phase space follows, making it impossible to keep a Fermi liquid description for 1D interacting systems. Haldane introduced the concept of the Luttinger liquid, a model that has its roots in the work by Tomonaga and Luttinger on the theory of interacting electrons in 1D. In this chapter we will study the Tomonaga-Luttinger liquid theory beginning by making plausible a description of 1D interacting systems in terms of boson operators. Such a bosonic description lies at the roots of the solution of the Tomonaga-Luttinger model known as *bosonization*, presented in the next chapter. Suggested literature on the subject includes: seminal papers by Tomonaga [45], Luttinger [26] and Haldane [14]. Deep reviews on the subject of strong correlated fermionic systems are those by Voit [46], Sólyom [40], and Schulz [33]. The bosonization method can be also consulted in the papers by Schönhammer [30], Senechal [36], and von Delft [47].

2.1 Non-interacting model

2.1.1 Linear dispersion approximation

In a one-dimensional many-particle system of non-interacting particles the Hamiltonian, in the language of the second quantization, is given by

$$H_0 = \sum_{k,\sigma} \epsilon(k) c^\dagger_{k,\sigma} c_{k,\sigma}, \tag{2.1}$$

where $c^\dagger_{i,\sigma}$ ($c_{i,\sigma}$) is the creation (annihilation) operator with spin index $\sigma = \downarrow, \uparrow$, and $\epsilon(k) = k^2/2m$ is the dispersion relation quadratic in the wavenumber k, and is shown in Fig. 2.1a for the first Brillouin zone. The Fermi level[1] is given by k_F lying in between the highest filled level and the lowest non-occupied level. Figure 2.1b shows the particle-hole excitations spectrum for two and three-dimensional systems. The particle-hole pairs can be created with arbitrarily low-energy, leading to a continuum of excitations for all momentum vectors q smaller than $2k_F$. In 1D, if we consider low-energy excitations, they are allowed *only* close to the Fermi points, because exciting a particle deep down the Fermi sea would require a great amount of energy and therefore such processes are forbidden. From Fig. 2.1c we observe that in the low-energy regime, the only possible well-defined excitations involve a momentum transfer of $q \sim 0$ or $q \sim 2k_F$. This feature is seen in the particle-hole spectrum, which modifies as shown in Fig. 2.1d. And this is one important reason for the bosonic treatment of these systems, because a particle-hole unit is a bosonic unit in nature. This will be formalized in this and the next chapter.

[1] Remember that the Fermi surface in 1D is represented by two points in phase space, $-k_F$ and $+k_F$.

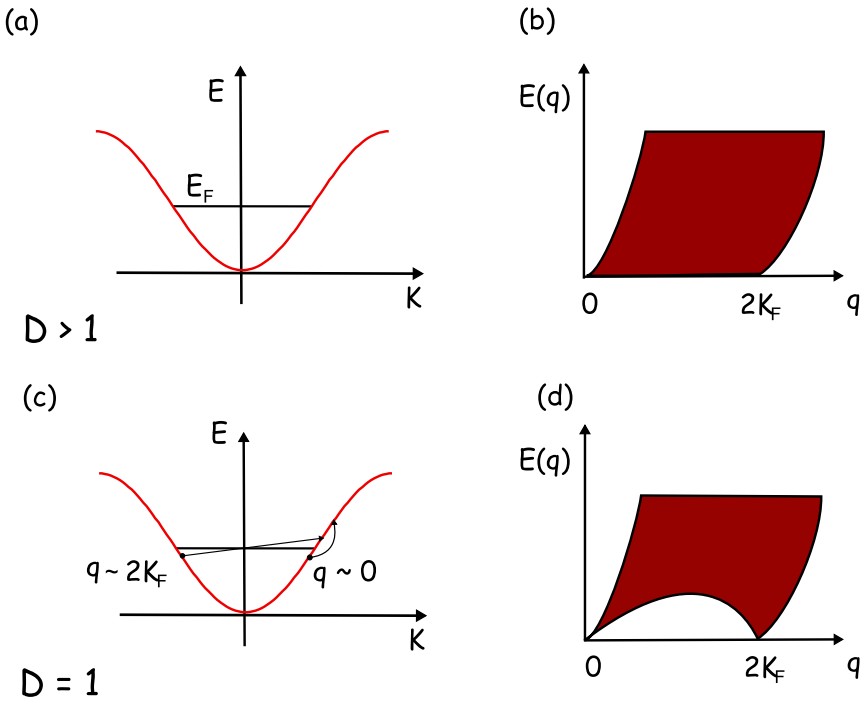

Figure 2.1: (a) Quadratic dispersion relation in the first Brillouin zone for higher dimensions with the Fermi energy level indicated. (b) Continuum spectrum of particle-hole pairs for higher dimensions. (c), (d) In 1D particle-hole pairs are allowed *only* close to the Fermi points, for $q \sim 0$ or $q \sim 2k_F$.

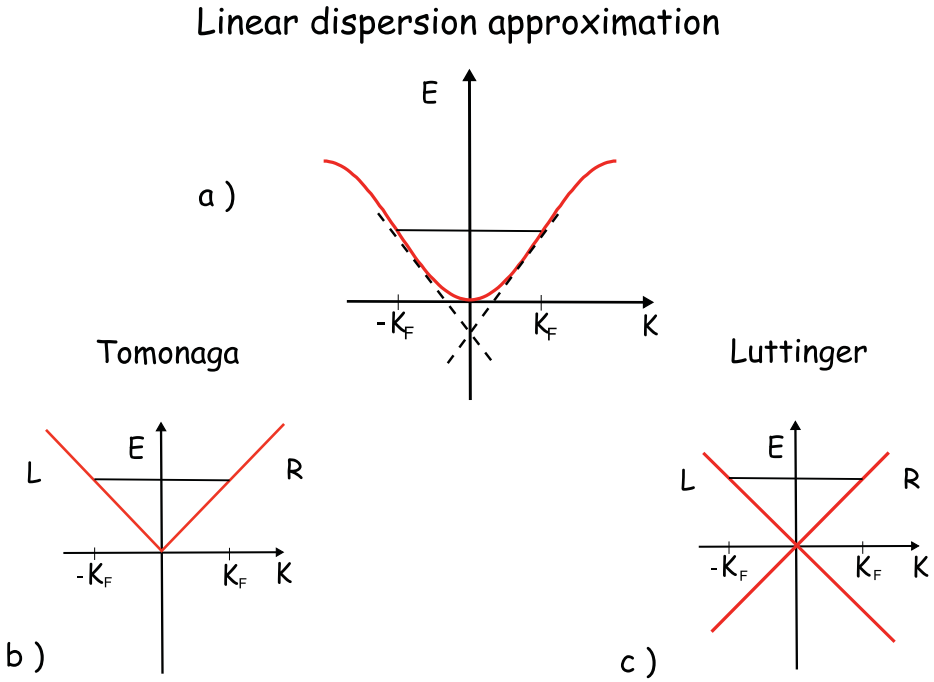

Figure 2.2: (a) Linear approximation close to the Fermi surface of the quadratic dispersion for free systems. (b) The Tomonaga model limits the linear approximation with a band cut-off in the momentum.(c) Luttinger extended the dispersion to $-\infty$ to make the mathematics easier to deal with. The extra non-physical states are removed by the introduction of the normal-ordering of operators.

If we consider to retain the low-energy properties of the system and excitations close to the Fermi level, a first approximation that can be done is to linearize the dispersion relation at the Fermi points (see Fig. 2.2a). A natural question that arises is how far can we extend such a linear dispersion. Tomonaga introduced from the beginning a band cut-off in the momentum (see Fig. 2.2b), as well as the concept of "right" and "left" movers, referring to the direction of the propagation of the electrons. This is described by the right and the left branch of the dispersion. Luttinger later extended the dispersion to $-\infty$, as shown in Fig. 2.2c. This introduces many extra states that must be removed at some point in the calculations to avoid infinite counting.

The electrons represented by the two branches may be defined in terms of the usual creation and annihilation fermionic operators. The left movers operator $c^\dagger_{+,k}$ and the right movers operator $c^\dagger_{-,k}$ are given by

$$\begin{aligned} c^\dagger_{+,k} &= c^\dagger_k, \text{ if } \ k \geq 0 \\ c^\dagger_{-,k} &= c^\dagger_k, \text{ if } \ k < 0. \end{aligned} \tag{2.2}$$

In terms of these operators, we introduce the linear dispersion in the free Hamiltonian (2.1) and obtain[2]

$$H_0 = \sum_{r,k} v_F(rk - k_F) : c^\dagger_{r,k} c_{r,k} : \tag{2.3}$$

where $r = \pm$ correspond to the branch index, + for the right branch and - for the left branch. The normal ordering of a product of operators : $\cdots$: was introduced to subtract the average value of the artificial vacuum generated by the extended linear dispersion of the Luttinger model. The normal ordering is defined as

$$\begin{aligned} : c^\dagger_{r,k} c_{r,k} : &= c^\dagger_{r,k} c_{r,k} - \langle \psi_0 | c^\dagger_{r,k} c_{r,k} | \psi_0 \rangle \\ &= c^\dagger_{r,k} c_{r,k} - \theta(k_F - rk) \end{aligned} \tag{2.4}$$

The Hamiltonian (2.3) is the free model of the Luttinger liquid and we will come to its solution in the next chapter.

2.1.2 Boson representation

The Tomonaga-Luttinger low-energy spectrum can be represented as a bosonic spectrum. A simple physical picture of this is the next: The spectrum in the low-energy regime is discrete with equidistant energy levels Δ. Let us define $N_F(E)$ and $N_B(E)$ as the number of states with energy E for the fermionic and bosonic systems respectively. A state with energy $\Delta = 1$ can be thought of as a fermion just above the Fermi surface or exactly one boson at the level $\Delta = 1$, so $N_F = N_B = 1$. If we consider fermion states with energy $\Delta = 2$, then the possible states are: either a fermion with two energy levels above the Fermi surface, or a fermion just above the Fermi surface with $\Delta = 1$ and a fermion just below the Fermi surface which jumped to the level left empty by the first fermion, finally $N_F = N_B = 2$. We can extend this analysis to other energy levels (of course, not for all), as for the example, the case $\Delta = 3$ for which $N_F = N_B = 3$. This equivalence is illustrated in Fig. 2.3.

[2]The formal process of linearization of the Hamiltonian (2.1) is presented in the next chapter.

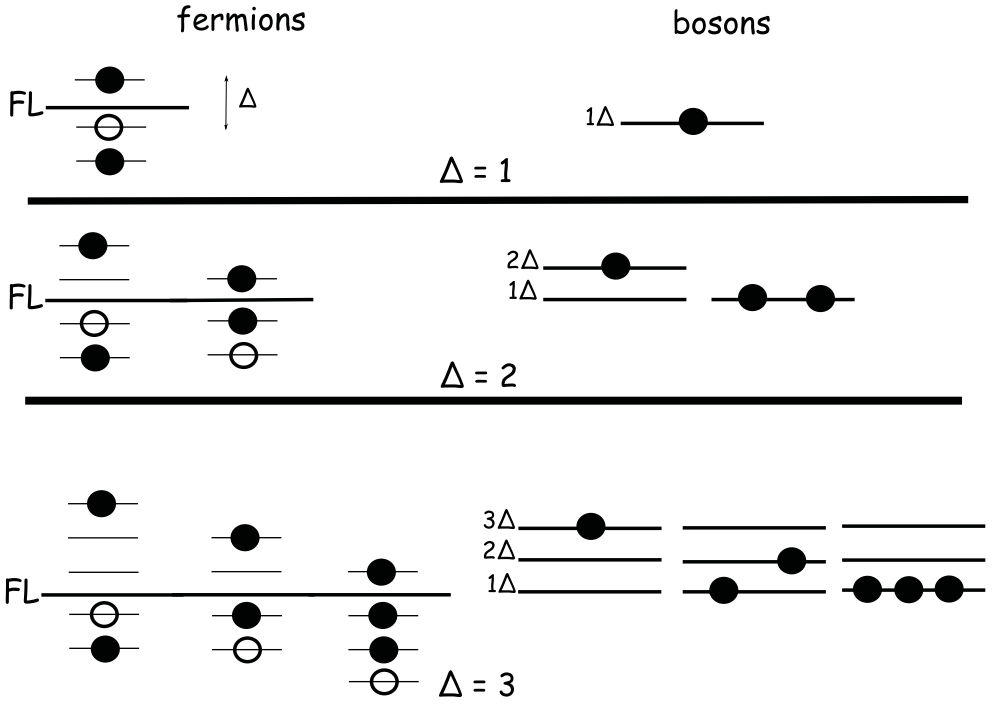

Figure 2.3: Equivalence between the energy levels of a fermionic and a bosonic system for a given energy Δ.

We can conclude that, in the low-energy limit, there is an equivalence between the energy levels of a fermionic system and the bosonic ones for a given energy. Therefore, it should be possible, in this limit, to write the fermionic Hamiltonian in a bosonic form. To formalize this idea let us first define the density operator for the branch r in the fermionic system,

$$\rho_r(x) \equiv : \psi_r^\dagger(x)\psi_r(x) : \tag{2.5}$$

with the field operator

$$\psi_r(x) = \frac{1}{\sqrt{L}} \sum_k e^{ikx} c_{r,k}. \tag{2.6}$$

The Fourier transform of the density operator is

$$\begin{aligned} \rho_{r,q} &= \int \mathrm{d}x e^{-iqx} \rho_r(x) \\ &= \begin{cases} \sum_k c_{r,k+q}^\dagger c_{r,k} & \text{if } \; q \neq 0 \\ \sum_k \left(c_{r,k}^\dagger c_{r,k} - \theta(k_F - rk) \right) & \text{if } \; q = 0. \end{cases} \end{aligned} \tag{2.7}$$

with commutator

$$\left[\rho_{r,q}, \rho_{r',-q'}\right] = -\delta_{r,r'}\delta_{q,q'} r L q/2\pi. \tag{2.8}$$

We observe that the commutator is similar, up to a constant, to that of creation ($a_q^\dagger$) and annihilation (a_q) boson operators

$$\left[a_q, a_{q'}^\dagger\right] = \delta_{q,q'}. \tag{2.9}$$

This indicates that there are bosonic degrees of freedom as part of the system and they are related to the density fluctuations. Indeed, the Hamiltonian for the free Luttinger model acquires the form,

$$H_0 \approx \sum_{q\neq 0} v_F |q| a_q^\dagger a_q. \tag{2.10}$$

Observe that the negative values of Eq. (2.3) have disappeared after the normal ordering was introduced. The Hamiltonian is still not complete due to the fact that we have not yet translated all the problem into the bosonic representation and there is still fermionic behavior in our Hamiltonian. The field operators of Eq. (2.6), for example, are still in terms of fermionic operators, which change the total number of particles in one, whereas the bosonic operators conserve the total number of particles. We will see in the next chapter that we can also write the fermionic field operators in terms of bosonic ones. The calculation of the density operators commutator (2.8) and detailed derivation of the Hamiltonian (2.10) are also left for the next chapter.

2.2 Interacting channels

We are now interested in considering the interactions of the system. In one dimension the available space for interactions is strongly limited compared to higher dimensional systems. The possible two-body interactions in 1D are clearly classified in terms of the momentum transfer they involve. According to this, there are four possible interaction processes identified by a set of coupling constants g_1, g_2, g_3 and g_4[3]. We will describe them next but not considering this numerical order; rather, we will order them in terms of an increasing momentum transfer:

- Forward scattering on different branches. When a particle from the left branch couples to one in the right branch, staying however on their original branch (see Fig. 4.2a). This process, with coupling constant g_2, involves a momentum transfer $q \sim 0$.
- Forward scattering on the same branch. When the two coupled particles are on the same branch (see Fig. 4.2b). This process, with coupling constant g_4, involves a momentum transfer $q \sim 0$.
- Backward scattering. When two particles switch their direction of motion, i. e., they switch branches keeping their spins (see Fig. 4.2c). This process, with coupling constant g_1, involves a momentum transfer $q \sim 2k_F$.
- Umklapp process. When two particles (of opposite spin) on the same branch switch their direction of motion, i. e., they switch branches (see Fig. 4.2d). This process, with coupling constant g_3, requires the system to be half-filled and involves a momentum transfer $q \sim 4k_F$.

Until now, the spin index has not been written explicitly, and for spinless fermions the only important processes are the forward scattering processes with g_2 and g_4. On the other hand, the couplings have two values for electrons with spin, corresponding to parallel $g_\parallel$, or antiparallel spins $g_\perp$. For spinless electrons, the g_1 and g_2 processes are identical, for the backward scattering can be considered an effective forward scattering process. If the spin is included, $g_{1\parallel} = g_{2\parallel}$, by permuting two of the operators but $g_{1\perp} \neq g_{2\perp}$. For spinful electrons we have corresponding charge (c) and spin (s) combinations of the coupling constants given by:

$$\begin{aligned} g_{ic} &= \frac{1}{2}\left(g_{i\parallel} + g_{i\perp}\right) \\ g_{is} &= \frac{1}{2}\left(g_{i\parallel} - g_{i\perp}\right) \end{aligned} \tag{2.11}$$

for $i = 1 \ \ldots \ 4$.

[3] This classification is known as the g-ology as described by Emery [10].

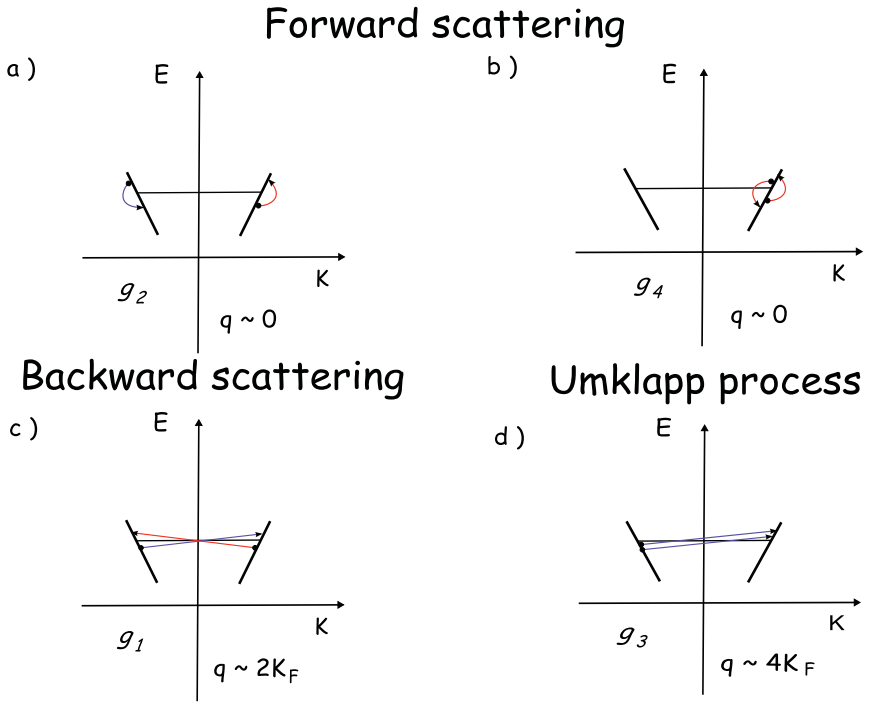

Figure 2.4: Interacting channels in 1D. (a) Forward scattering on different branches with constant coupling g_2.(b) Forward scattering on the same branch with constant coupling g_4.(c) Backward scattering with constant coupling g_1. (d) Umklapp process with constant coupling g_3.

The Tomonaga-Luttinger model deals only with the low-momentum transfer events, hence we will only take into account the g_2 and g_4 interactions[4]. A general form for the interaction, which depends only on the position of the particles, is

$$H_{int} = \sum_r \int \mathrm{d}x\ \mathrm{d}x' \big[\rho_r(x) g_2(x-x') \rho_{-r}(x') + \rho_r(x) g_4(x-x') \rho_r(x')\big]. \tag{2.12}$$

The first term refers to the interaction g_2 for fields with opposite r-values, and the second term accounts for interaction between fields with the same r-value. The Fourier expansion of these interactions is

$$g_{2,4}(x) = \frac{\pi}{L} \sum_q e^{iqx} g_{2,4}(q). \tag{2.13}$$

Furthermore, we will assume that $g_{2,4}(q) = g_{2,4}(-q)$, which means that $g_{2,4}(x) = g_{2,4}(-x)$. Upon introduction of the Fourier expansion (2.13) in (2.12) and after performing the integrals, the interaction in momentum space takes the form:

$$H_{int} = \frac{\pi}{L} \sum_{r,q} \Big(g_2(q) \rho_r(q) \rho_{-r}(-q) + g_4(q) \rho_r(q) \rho_r(-q) \Big). \tag{2.14}$$

The form of Hamiltonian (2.14) involves actually quartic terms in the fermion operators, but by using boson operators a, $a^\dagger$, which are still to be defined, or linear combinations of them, the interaction remains quadratic in the boson operators, being thus easy to diagonalize by means of a Bogoliubov transformation.

[4]In the following we are dropping the spin index.

Summary

In this chapter we introduced the Tomonaga-Luttinger liquid model in an intuitive and physical way. We observed how the particle-hole spectrum changes in 1D, restricting the excitations to only those with momentum $q = 0$ or $q = 2k_F$, close to the Fermi surface. We discussed that in 1D, the dispersion relation can be approximated by a linear function in the low-energy regime. In this limit as well, the energy spectrum of both fermionic and bosonic systems is equivalent, thus 1D systems can be represented by bosonic variables. We also discussed the possible interacting channels in 1D and classified them following the notation by Emery [10].

Chapter 3

Bosonization

In the previous chapter we presented the Tomonaga-Luttinger model for one-dimensional strongly correlated systems. Considering the discussed properties of low-dimensional systems, there is a plausible bosonic representation of such systems in the low-energy regime. In this chapter we will formalize this. First we will derive the Hamiltonian for the free Luttinger model. Then we will construct the density operator. We will find that its properties will allow for the construction of boson operators from which a complete set of boson eigenstates can be generated. Afterwards, the field operators must also be transformed into the boson basis. We will discuss the interacting systems and finally the correlation functions[1].

3.1 Non-interacting model

3.1.1 Free Luttinger model

We want to obtain the Hamiltonian with linear dispersion

$$H_0 = \sum_{r,k,\sigma} v_F(rk - k_F) : c^\dagger_{r,k,\sigma} c_{r,k,\sigma} : \tag{3.1}$$

from the free Hamiltonian of Eq. (2.1) using the new operators for right and left propagating electrons[2],

$$\begin{aligned} c_{+,k} &= c_k, \text{ if } \ k \geq 0 \\ c_{-,k} &= c_k, \text{ if } \ k < 0. \end{aligned} \tag{3.2}$$

Conversely, the usual fermionic operators can be expressed in the compact form:

$$c_k = \sum_r \theta(rk) c_{r,k}, \tag{3.3}$$

with $r = \pm$, and $\theta(x)$ is the step function defined as

$$\theta(x) = \begin{cases} 1 & \text{if } \ x \geq 0 \\ 0 & \text{if } \ x < 0. \end{cases} \tag{3.4}$$

In terms of the new particle operators, the field operator $\psi(x)$ is

$$\psi(x) = \frac{1}{\sqrt{L}} \sum_{r,k} \theta(rk) e^{ikx} c_{r,k}. \tag{3.5}$$

In a non-interacting one-dimensional system, the Hamiltonian, which consist only of the kinetic term, is given by

$$H_0 = -\frac{1}{2m} \int \mathrm{d}x \ \psi^\dagger(x) \partial_x^2 \psi(x). \tag{3.6}$$

[1] It is worth mentioning that the bosonization method has found application in other phenomena. We suggest the paper by Senechal [36] and the book by Stone [41] for a survey on the subject of bosonization applied to other problems.

[2] In the following we will drop the spin index but can be recovered anytime.

Inserting in (3.6) the field operator from (3.5) and performing the integral the Hamiltonian turns into:

$$\begin{aligned} H_0 &= \frac{1}{2m}\sum_{r,k}\theta(rk)k^2 c^\dagger_{r,k}c_{r,k} \\ &= \frac{1}{2m}\sum_{r,k}\theta(rk)\big(rk-k_F+k_F\big)^2 c^\dagger_{r,k}c_{r,k}. \end{aligned} \tag{3.7}$$

In the last line of Eq. (3.7) we made use of the fact that $r^2=1$ and inserted a zero by adding and subtracting k_F. Next, we expand the quadratic term to find

$$\begin{aligned} H_0 = \frac{1}{2m}k_F^2\Bigg\{ &\sum_{r,k}\theta(rk)\left(\frac{rk-k_F}{k_F}\right)^2 c^\dagger_{r,k}c_{r,k} \\ &+2\sum_{r,k}\theta(rk)\left(\frac{rk-k_F}{k_F}\right)c^\dagger_{r,k}c_{r,k} \\ &+\sum_{r,k}\theta(rk)c^\dagger_{r,k}c_{r,k}\Bigg\}. \end{aligned} \tag{3.8}$$

Let us now observe this Hamiltonian in the context of our low-energy regime. Since for low-energy states only excitations close to the Fermi points are allowed, and for these states we find that their contribution to the sum $\sim (rk-k_F/k_F)^2$ is a small number, the sum of quadratic terms can be ignored in this limit, getting for the Hamiltonian the next approximation:

$$H_0 \approx v_F\sum_{r,k}\theta(rk)(rk-k_F)c^\dagger_{r,k}c_{r,k}+\frac{1}{2}v_Fk_F\sum_{r,k}\theta(rk)c^\dagger_{r,k}c_{r,k}, \tag{3.9}$$

with the Fermi velocity, $v_F=k_F/m$. Now we want to measure the energy with respect to the ground state, which is given by both branches filled below the Fermi points and has an energy E_0. We will consider the extended linear dispersion (to $\pm\infty$) proposed by Luttinger, as it has no influence in the low-energy regime, close to the Fermi points, but it will be necessary when studying the boson-fermion equivalence. Subtracting the ground state, we find

$$\begin{aligned} H_0-E_0 \approx\ & v_F\sum_{r,k}\theta(rk)(rk-k_F)\big(c^\dagger_{r,k}c_{r,k}-\theta(k_F-rk)\big) \\ &+\frac{1}{2}v_Fk_F\sum_{r,k}\theta(rk)\big(c^\dagger_{r,k}c_{r,k}-\theta(k_F-rk)\big). \end{aligned} \tag{3.10}$$

Since only terms with $rk>0$ will contribute, i.e., for r and k with the same sign, we can then write the Hamiltonian as:

$$\begin{aligned} H_0-E_0 \approx\ & v_F\sum_{r,k}(rk-k_F)\big(c^\dagger_{r,k}c_{r,k}-\theta(k_F-rk)\big) \\ &+\frac{1}{2}v_Fk_F\sum_{r,k}\big(c^\dagger_{r,k}c_{r,k}-\theta(k_F-rk)\big). \end{aligned} \tag{3.11}$$

The last term in Hamiltonian (3.11) corresponds to the number of particles relative to the ground state, and if constant assumed, we finally obtain the Hamiltonian for the free

Luttinger model:

$$\begin{aligned} H_0 = \; & v_F \sum_{r,k} (rk - k_F)\big(c^\dagger_{r,k} c_{r,k} - \theta(k_F - rk)\big) \\ = & \sum_{r,k} v_F (rk - k_F) : c^\dagger_{r,k} c_{r,k} : \end{aligned} \tag{3.12}$$

3.1.2 The density operator

In this section we will prove the commutation relation of Eq. (2.8) for the density operator. This will let us construct a boson basis in the next section. We recall that the density operator is defined as:

$$\rho_r(x) \equiv : \psi^\dagger_r(x) \psi_r(x) : \tag{3.13}$$

with Fourier transformation:

$$\begin{aligned} \rho_{rq} &= \int \mathrm{d}x e^{-iqx} \rho_r(x) \\ &= \begin{cases} \sum_k c^\dagger_{r,k+q} c_{r,k} & \text{if } \; q \neq 0 \\ \sum_k \big(c^\dagger_{r,k} c_{r,k} - \theta(k_F - rk)\big) & \text{if } \; q = 0, \end{cases} \end{aligned} \tag{3.14}$$

Let us write and expand the next commutator:

$$\begin{aligned} \big[\rho_{r,q}, \rho_{r',-q'}\big] &= \sum_{k,k'} \Big(c^\dagger_{r,k+q} c_{r,k} c^\dagger_{r',k'-q'} c_{r',k'} - c^\dagger_{r',k'-q'} c_{r',k'} c^\dagger_{r,k+q} c_{r,k} \Big) \\ &= \sum_{k,k'} \Big(\delta_{r,r'} \delta_{k,k'-q'} c^\dagger_{r,k+q} c_{r',k'} - \delta_{r,r'} \delta_{k',k+q} c^\dagger_{r',k'-q'} c_{r,k} \Big) \\ &= \delta_{r,r'} \sum_k \big(c^\dagger_{r,k+q} c_{r',k+q'} - c^\dagger_{r',k+q-q'} c_{r,k} \big). \end{aligned} \tag{3.15}$$

The second line results after using the anticommutation relations of $c_{r,k}$ and $c^\dagger_{r,k}$. In the last line the summation over k' was performed. Now let us analyze the result of Eq. (3.15). For $q \neq q'$ the commutator is already normal ordered and upon the change of variables $k + q \to k + q - q'$ the commutator vanishes. If $q = q'$ the commutator must be normally ordered first. Using the definition of Eq. (2.4) for the normal order, the commutator can be expressed as:

$$\delta_{r,r'} \delta_{q,q'} \sum_k \Big(: c^\dagger_{r,k+q} c_{r,k+q} : + \theta\big(k_F - r(k+q)\big) - : c^\dagger_{r,k} c_{r,k} : - \theta\big(k_F - rk\big) \Big). \tag{3.16}$$

By shifting $k \to k + q$, the ordered expressions cancel leaving only

$$\begin{aligned} & \delta_{r,r'} \delta_{q,q'} \sum_k \Big(\theta\big(k_F - r(k+q)\big) - \theta\big(k_F - rk\big) \Big) \\ &= \begin{cases} \delta_{r,r'} \delta_{q,q'} \; \big[\theta\big(k_F - (k+q)\big) - \theta\big(k_F - k\big)\big] & \text{if } \; r = + \\ \delta_{r,r'} \delta_{q,q'} \; \big[\theta\big(k_F + (k+q)\big) - \theta\big(k_F + k\big)\big] & \text{if } \; r = -. \end{cases} \\ &= \begin{cases} -\delta_{r,r'} \delta_{q,q'} Lq/2\pi & \text{if } \; r = + \\ +\delta_{r,r'} \delta_{q,q'} Lq/2\pi & \text{if } \; r = -. \end{cases} \end{aligned} \tag{3.17}$$

The last line follows from evaluating the sum of the step functions for different signs of r and q. Summarizing,

$$\big[\rho_{r,q}, \rho_{r',-q'}\big] = -\delta_{r,r'} \delta_{q,q'} \frac{rLq}{2\pi}. \tag{3.18}$$

If the spin index $s = \downarrow, \uparrow$ is introduced, charge and spin densities can be defined respectively as:

$$\rho_r^c(q) = \frac{1}{\sqrt{2}}\big[\rho_{r\uparrow}(q) + \rho_{r\downarrow}(q)\big] \tag{3.19}$$

and

$$\rho_r^s(q) = \frac{1}{\sqrt{2}}\big[\rho_{r\uparrow}(q) - \rho_{r\downarrow}(q)\big]. \tag{3.20}$$

These operators obey the same commutation relations as in (3.18).

3.1.3 Boson representation

We will formulate the complete boson representation in three stages: *a*) constructing the boson operators, *b*) constructing the boson eigenstates, and *c*) carrying out the bosonization of the field operators.

Boson operators

Since the density operators commute in a similar way as the bosonic ones, let us define new boson operators for $q \neq 0$:

$$a_q^\dagger = \sqrt{\frac{2\pi}{|q|L}} \sum_r \theta(rq)\rho_{r,q} \tag{3.21}$$

$$a_q = \sqrt{\frac{2\pi}{|q|L}} \sum_r \theta(rq)\rho_{r,-q}. \tag{3.22}$$

Using the result from Eq. (3.18), we can compute the next commutators for the a's operators,

$$\begin{aligned}\big[a_q, a_{q'}^\dagger\big] &= \frac{2\pi}{L\sqrt{|qq'|}} \sum_{r,r'} \theta(rq)\theta(r'q')\big[\rho_{r,-q}, \rho_{r',q'}\big] \\ &= \delta_{q,q'} \frac{1}{\sqrt{|qq'|}} \sum_r rq'\theta(rq)\theta(rq').\end{aligned} \tag{3.23}$$

We observe from the last line, that the only contributions are those for which $rq > 0$, thus the final result reduces to $\delta_{q,q'}$. Another commutator is:

$$\begin{aligned}\big[a_q^\dagger, a_{q'}^\dagger\big] &= \frac{2\pi}{L\sqrt{|qq'|}} \sum_{r,r'} \theta(rq)\theta(r'q')\big[\rho_{r,q}, \rho_{r',q'}\big] \\ &= -\frac{1}{\sqrt{|qq'|}} \sum_{r,r'} \delta_{r,r'}\delta_{-q',q}\ rq\theta(rq)\theta(r'q') \\ &= -\frac{1}{\sqrt{|qq'|}} \sum_r \delta_{-q',q}\ rq\theta(rq)\theta(rq').\end{aligned} \tag{3.24}$$

In the last line, the Kronecker delta, $\delta_{-q',q}$, keeps both step functions equal to zero at the same time, thus the commutator vanishes. Similarly the commutator $[a_q, a_{q'}]$ vanishes. We can summarize the results in the following,

$$\big[a_q, a_{q'}^\dagger\big] = \delta_{q,q'} \tag{3.25}$$

$$\left[a_q, a_{q'}\right] = \left[a_q^\dagger, a_{q'}^\dagger\right] = 0. \tag{3.26}$$

We have so far shown that boson operators can be written in terms of the density operators and now we are left with the task of inverting Eq. (3.21) and Eq. (3.22). To this end, we will rewrite the a's in the following way:

$$\theta(rq)a_q^\dagger = \sqrt{\frac{2\pi}{|q|L}}\theta(rq)\rho_{r,q} \tag{3.27}$$

and

$$\theta(-rq)a_{-q} = \sqrt{\frac{2\pi}{|q|L}}\theta(-rq)\rho_{r,q}. \tag{3.28}$$

If $q \neq 0$, then

$$\begin{aligned}\rho_{r,q} &= \big\{\theta(rq) + \theta(-rq)\big\}\rho_{r,q} \\ &= \sqrt{L|q|/2\pi}\big\{\theta(rq)a_q^\dagger + \theta(-rq)a_{-q}\big\}.\end{aligned} \tag{3.29}$$

If $q = 0$, the corresponding mode is represented by the number operator $N_r \equiv \sum_k n_{r,k} - \langle n_{r,k}\rangle_0$, which results from the normal ordering, thus:

$$\rho_{r,q} = N_r\delta_{q,0} + \sqrt{L|q|/2\pi}\big\{\theta(rq)a_q^\dagger + \theta(-rq)a_{-q}\big\} \tag{3.30}$$

Now the density operator has been reformulated in terms of bosonic variables. In the following we will construct the boson eigenstates.

Boson eigenstates

Before we construct a set of boson states, we need to investigate the commuting properties of Hamiltonian (3.12) and its effect on states of the two branches.

We look first at the commutator between the Hamiltonian H_0 and the particle number operator N_r on branch r,

$$\begin{aligned}\left[H_0, N_r\right] &= v_F \sum_{r',k'}\sum_k \big(r'k' - k_F\big)\left[c_{r',k'}^\dagger c_{r',k'}, c_{r,k}^\dagger c_{r,k}\right] \\ &= v_F \sum_{r',k'}\sum_k \big(r'k' - k_F\big)\big(\delta_{k,k'}\delta_{r,r'}c_{r',k'}^\dagger c_{r,k} - \delta_{k,k'}\delta_{r,r'}c_{r,k}^\dagger c_{r',k'}\big)\end{aligned} \tag{3.31}$$

After performing the prime summations, the last line vanishes, finding that H_0 and N_r can have common eigenstates, since

$$\left[H_0, N_r\right] = 0. \tag{3.32}$$

Now let us think of possible states of the system. We can construct states from the ground state by adding N_r fermions to the first levels just above the Fermi point for the branch r, and by removing N_{-r} fermions just below the Fermi level. We can write such states as the set $\{|N_rN_{-r}\rangle\}$. These are eigenstates of the number operator N_r and have a filling $\theta\big(k_F + N_r2\pi/L - rq\big)$, where we observe that it has been increased or decreased in N_r. The effect of the Hamiltonian (3.12) on these states indicates that $\{|N_rN_{-r}\rangle\}$ are eigenstates of H_0 with energies given by:

$$\begin{aligned}E_{N_rN_{-r}} &= v_F\pi/L\sum_r N_r(N_r+1)^2, \\ &= v_F\pi/L\sum_r N_r^2,\end{aligned} \tag{3.33}$$

where the last line results from dropping the term N_r/L in the thermodynamic limit. Let us compute the commutator between H_0 and ρ_{qr},

$$\begin{aligned}
\big[H_0, \rho_{r,q}\big] &= v_F \sum_{r',k'} \sum_{k} \big(r'k' - k_F\big)\big(c^\dagger_{r',k'} c_{r',k'} c^\dagger_{r,k+q} c_{r,k} - c^\dagger_{r,k+q} c_{r,k} c^\dagger_{r',k'} c_{r',k'}\big) \\
&= v_F \sum_{r',k'} \sum_{k} \big(r'k' - k_F\big)\big(\delta_{k',k+q}\delta_{r,r'} c^\dagger_{r',k'} c_{r,k} - \delta_{k,k'}\delta_{r,r'} c^\dagger_{r,k+q} c_{r',k'}\big) \\
&= v_F \sum_{k} \big\{\big(r(k+q) - k_F\big) c^\dagger_{r,k+q} c_{r,k} - \big(rk - k_F\big) c^\dagger_{r,k+q} c_{r,k}\big\} \\
&= v_F r q \rho_{r,q}. \qquad (3.34)
\end{aligned}$$

The second line is obtained after repeatedly application of the anticommutation relations. The third line follows from the primed summations, and in the last line we use the definition of $\rho_{r,q}$ in Eq. (3.14). The previous results for the commutators allow for the straightforward calculation of the commutator between H_0 and $a^\dagger_q$,

$$\begin{aligned}
\big[H_0, a^\dagger_q\big] &= \sqrt{2\pi/L|q|} \sum_r \theta(rq) \big[H_0, \rho_{r,q}\big] \\
&= \sqrt{2\pi/L|q|} \sum_r \theta(rq) v_F r q \rho_{r,q} \\
&= v_F |q| a^\dagger_q. \qquad (3.35)
\end{aligned}$$

By an induction procedure, the result in (3.35) is easily generalized to

$$\big[H_0, \big(a^\dagger_q\big)^{n_q}\big] = n_q v_F |q| \big(a^\dagger_q\big)^{n_q} \quad \text{for } n_q \geq 0, \qquad (3.36)$$

with the corresponding Hermitian conjugate

$$\big[H_0, a^{n_q}_q\big] = -n_q v_F |q| a^{n_q}_q \quad \text{for } n_q \geq 0. \qquad (3.37)$$

From this we can conclude that if $|E\rangle$ is an eigenstate of H_0 with energy E, then $(a^\dagger_q)^{n_q}|E\rangle$ is also an eigenstate of H_0 with energy $E + v_F n q |q|$ and $a^{n_q}_q|E\rangle$ is an eigenstate with energy $E - v_F n_q |q|$. In this way, a whole set of eigenstates for H_0 can be constructed with a_q and $a^\dagger_q$ acting as ladder operators. From this, we define the next boson states:

$$|N_r, N_{-r}, \{n_q\}\rangle = \prod_{q\neq 0} \frac{(a^\dagger_q)^{n_q}}{\sqrt{n_q!}} |N_r N_{-r}\rangle, \qquad (3.38)$$

and using the results in (3.33) and (3.36), we find that the eigenvalues of such states are given by

$$E(N_r, N_{-r}, \{n_q\}) = v_F \sum_{q\neq 0} n_q |q| + v_F \pi/L \sum_r N_r^2. \qquad (3.39)$$

Thus, the Hamiltonian (3.12) can be expressed in terms of the boson operators a_q as:

$$H_0 = v_F \sum_{q\neq 0} |q| a^\dagger_q a_q + v_F \pi/L \sum_r N_r^2. \qquad (3.40)$$

The completeness of the set of these bosonic states is supported by Haldane, who showed that the N-particle Hilbert space $\mathcal{H}_\mathcal{N}$, spanned by all possible particle-hole excitations of $|N\rangle_0$, is also spanned by repeatedly applying $a^\dagger_q$ on $|N\rangle_0$, as is here the case. Furthermore, the bosonic states are an orthonormal set with

$$\langle N'_r, N'_{-r}, \{n'_q\} | N_r, N_{-r}, \{n_q\}\rangle = \delta_{N_r,N'_r} \delta_{N_{-r},N'_{-r}} \delta_{\{n_q\},\{n'_q\}}. \qquad (3.41)$$

To conclude this section, let us define the operators N and J corresponding to the total number of particles and the current (given by the difference between the left and right movers), respectively, by:

$$\begin{aligned} N &= N_0 + \sum_r N_r, \\ J &= \sum_r r N_r \end{aligned} \tag{3.42}$$

from which follows that

$$\begin{aligned} 2\sum_r N_r^2 &= (N - N_0)^2 + J^2 \\ 2\sum_r N_r N_{-r} &= (N - N_0)^2 - J^2. \end{aligned} \tag{3.43}$$

After inserting (3.43) into (3.40) we obtained the free bosonized Hamiltonian

$$H_0 = v_F \sum_{q\neq 0} |q| a_q^\dagger a_q + \frac{\pi}{2L}\Big(v_F (N - N_0)^2 + v_F J^2\Big). \tag{3.44}$$

So far, we have shown how the density operator and the Hamiltonian can be written in terms of bosonic operators, and constructed a complete set of orthonormal boson states. In the following, we will perform the bosonization of the field operators too.

Bosonization of the field operator

The boson representation of the field operator (2.6) has been discussed by Haldane [14] and by Schönhammer [30]. In this section we will follow the presentation of the later, still we will obtain the same results as those by Haldane.

Let us define the following in terms of the boson operators a_q,

$$\begin{aligned} A &= \sum_{q\neq 0} \lambda_q a_q^\dagger \\ B &= \sum_{q\neq 0} \mu_q a_q. \end{aligned} \tag{3.45}$$

Given two operators a and b, such that $\big[b,[a,b]\big] = 0$, then $\big[a, e^b\big] = \big[a,b\big]e^b$. Furthermore,

$$\begin{aligned} \big[a_q, e^B e^A\big] &= e^B \big[a_q, e^A\big] + \big[a_q, e^B\big] e^A \\ &= e^B \big[a_q, A\big] e^A \\ &= \lambda_q e^B e^A \end{aligned} \tag{3.46}$$

and

$$\begin{aligned} \big[a_q^\dagger, e^B e^A\big] &= e^B \big[a_q^\dagger, e^A\big] + \big[a_q^\dagger, e^B\big] e^A \\ &= \big[a_q^\dagger, B\big] e^B e^A \\ &= -\mu_q e^B e^A. \end{aligned} \tag{3.47}$$

Now, given a fermionic operator S satisfying the following equations

$$\begin{aligned} \big[a_q, S\big] &= -\lambda_q S \big[a_q^\dagger, S\big] \\ &= \mu_q S, \end{aligned} \tag{3.48}$$

by the commutation relations of e^A and e^B above, we find that

$$\begin{aligned}\big[a_q, Se^Be^A\big] &= \big[a_q, S\big]e^Be^A + S\big[a_q, e^Be^A\big] \\ &= -\lambda_q Se^Be^A - \lambda_q Se^Be^A \\ &= 0 \end{aligned} \tag{3.49}$$

and

$$\begin{aligned}\big[a_q^\dagger, Se^Be^A\big] &= \big[a_q^\dagger, S\big]e^Be^A + S\big[a_q^\dagger, e^Be^A\big] \\ &= \mu_q Se^Be^A - \mu_q Se^Be^A \\ &= 0. \end{aligned} \tag{3.50}$$

From the results above, we see that the operator Se^Be^A commutes with both a_q and $a_q^\dagger$, furthermore, $S \sim e^{-A}e^{-B}$, i. e., the fermionic operator is related to exponentials of boson fields. If we could only identify the operator Se^Be^A, then we could have a fermionic field operator in terms of boson variables. Let us identify $\psi_r^\dagger(x)$ with S to find the values of λ_q and μ_q by computing the next commutators,

$$\begin{aligned}\big[a_q, \psi_r^\dagger(x)\big] &= \sqrt{2\pi/|q|L}\sum_{r'}\theta(r'q)\big[\rho_{r',-q}, \psi_r^\dagger(x)\big] \\ &= \sqrt{2\pi/|q|L}\sum_{r'}\theta(r'q)\delta_{r,r'}e^{iqx}\psi_r^\dagger(x) \\ &= \theta(qr)\sqrt{2\pi/|q|L}e^{iqx}\psi_r^\dagger(x) \end{aligned} \tag{3.51}$$

and

$$\begin{aligned}\big[a_q^\dagger, \psi_r^\dagger(x)\big] &= \sqrt{2\pi/|q|L}\sum_{r'}\theta(r'q)\big[\rho_{r',q}, \psi_r^\dagger(x)\big] \\ &= \sqrt{2\pi/|q|L}\sum_{r'}\theta(r'q)\delta_{r,r'}e^{-iqx}\psi_r^\dagger(x) \\ &= \theta(qr)\sqrt{2\pi/|q|L}e^{-iqx}\psi_r^\dagger(x). \end{aligned} \tag{3.52}$$

Thus, we can choose

$$\begin{aligned}\lambda_q &= -\theta(rq)\sqrt{2\pi/|q|L}e^{iqx} \\ \mu_q &= -\theta(rq)\sqrt{2\pi/|q|L}e^{-iqx}. \end{aligned}$$

and we can construct the next operator

$$O_r(x) = \psi_r^\dagger e^{i\varphi_r(x)}e^{i\varphi_r^\dagger(x)}, \tag{3.53}$$

where

$$\varphi_r(x) = -i\sum_{q\neq 0}\theta(rq)\sqrt{2\pi/|q|L}e^{-iqx}a_q. \tag{3.54}$$

The operator $O_r(x)$ commutes with both a_q and $a_q^\dagger$. Besides, it is uniquely determined and represented in the boson basis. By inversion of Eq. (3.53), we find an expression for $\psi_r^\dagger(x)$ in terms of boson operators.

By inverting Eq. (3.53), we find[3]

$$\begin{aligned}&\langle N_r', N_{-r}'|\psi_r^\dagger(x)|N_r, N_{-r}\rangle \\ &= \langle N_r', N_{-r}'|O_r(x)e^{-i\varphi_r^\dagger}e^{-i\varphi_r(x)}|N_r, N_{-r}\rangle \\ &= \langle N_r', N_{-r}'|O_r(x)|N_r, N_{-r}\rangle \end{aligned} \tag{3.55}$$

[3]This results from the commutation relation between the O's and the exponentials of φ

Recalling the definition of the field operator (2.6), we obtain

$$\begin{aligned}&\langle N_r', N_{-r}'|O_r(x)|N_r, N_{-r}\rangle \\ &= \frac{1}{\sqrt{L}}\sum_k e^{ikx}\langle N_r', N_{-r}'|c_{r,k}^\dagger(x)|N_r, N_{-r}\rangle\end{aligned} \tag{3.56}$$

Since the set of states $|N_r, N_{-r}\rangle$ is orthonormal, the inner product in the sum of the last equation vanishes except for the case in which $|N_r', N_{-r}'\rangle = |N_r+1, N_{-r}\rangle$ and $k = k_F + 2\pi(N_r+1)/L - \pi/L$ [4], thus[5]

$$\begin{aligned}O_r(x)|N_r, N_{-r}\rangle &= |N_r+1, N_{-r}\rangle L^{1/2} e^{i(2\pi(N_r+1)/L + k_F - \pi/L)rx} \\ &= L^{-1/2} e^{i(k_F-\pi/L)rx} e^{irx2\pi N_r/L}|N_r+1, N_{-r}\rangle.\end{aligned} \tag{3.57}$$

From the last results we can conclude that the effect of the $O_r(x)$ on a boson eigenstate is given by

$$\begin{aligned}O_r(x)|N_r, N_{-r}, \{n_q\}\rangle &= \prod_{q\neq 0}\frac{(a_q^\dagger)^{n_q}}{\sqrt{n_q!}} O_r(x)|N_r, N_{-r}\rangle \\ &= \prod_{q\neq 0}\frac{(a_q^\dagger)^{n_q}}{\sqrt{n_q!}} L^{-1/2} e^{i(k_F-\pi/L)rx} e^{irx2\pi N_r/L}|N_r+1, N_{-r}\rangle \\ &= L^{-1/2} e^{i(k_F-\pi/L)rx} e^{irx2\pi N_r/L}|N_r+1, N_{-r}, \{n_q\}\rangle\end{aligned} \tag{3.58}$$

where we have used the commutation relations between $O_r(x)$ and $a_q^\dagger$. And we can define the operator U_r as

$$U_r \equiv L^{1/2} e^{-i(k_F-\pi/L)rx} e^{-irx2\pi N_r/L} O_r(x). \tag{3.59}$$

The operator U_r, as well as it conjugate $U_r^\dagger$, inherits the commutation relations of $O_r(x)$ with $a_q^\dagger$ and a_q. U_r is a ladder operator that raises the fermion number on the r-branch by one and, at the same time, commutes with the boson operators a_q. U_r is a unitary operator, i.e., $U_r^\dagger U_r = U_r U_r^\dagger = 1$. Such operators are also known in the field theory language as "Klein factors".

Recalling the definition of $\psi_r^\dagger$, as obtained by inversion of (3.53), and the definition of U_r, (3.59), we find

$$\begin{aligned}\psi_r^\dagger(x) &= O_r(x) e^{-i\varphi_r^\dagger(x)} e^{-i\varphi_r(x)} \\ &= L^{-1/2} e^{i(k_F-\pi/L)rx} e^{irx2\pi N_r/L}\ U_r\ e^{-i\varphi_r^\dagger(x)} e^{-i\varphi_r(x)} \\ &= L^{-1/2} e^{i(k_F-\pi/L)rx} e^{irx\pi N_r/L} e^{-i\varphi_r^\dagger(x)}\ U_r\ e^{irx\pi N_r/L} e^{-i\varphi_r(x)},\end{aligned} \tag{3.60}$$

Defining the next

$$\begin{aligned}\phi_r(x) &= r(\pi x/L)N_r - \varphi_r(x) \\ &= r(\pi x/L)N_r + i\sum_{q\neq 0}\theta(rq)\sqrt{2\pi/L|q|}e^{-iqx}a_q,\end{aligned} \tag{3.61}$$

we can write the Fermi field operator $\psi_r^\dagger$ as

$$\psi_r^\dagger(x) = \frac{1}{\sqrt{L}} e^{irk_F x} e^{i\phi_r^\dagger(x)}\ U_r\ e^{i\phi_r(x)}. \tag{3.62}$$

[4] This corresponds to creating a particle with the lowest momentum available.

[5] In the first line of Eq. (3.57), the N_r in the exponential refers to the eigenvalue of the number operator, whilst in the exponential in the second line, N_r is the number operator.

Equation (3.62) is a tremendous result, for it states that the degrees of freedom of our Fermi systems can be expressed as bosonic degrees of freedom. The field operator $\phi_r(x)$ was introduced by Haldane in the context of a charge (N) and current (J) formalism, by making symmetric and antisymmetric combinations of the left and right movers. Following this idea, we have already introduced the operators for charge and current in Eq. (3.42). Further, we can define the density and field operators as:

$$\rho_N(x) = \frac{N_0}{L} + \sum_r \rho_r(x),$$
$$\rho_J(x) = \sum_r r\rho_r(x),$$

where $N_0 = k_F L/\pi$, and

$$\phi_N(x) = \sum_r \phi_r(x),$$
$$\phi_J(x) = \frac{\pi N_0}{L}x + \sum_r r\phi_r(x),$$

By defining the next local phase fields $\theta_N(x)$ and $\theta_J(x)$ as

$$\theta_N(x) = \phi_N(x) + \phi_N^\dagger(x),$$
$$\theta_J(x) = \phi_J(x) + \phi^{\dagger_J(x)}.$$

It is easy to deduce the following relations:

$$\partial_x\theta_N(x) = 2\pi\rho_J(x),$$
$$\partial_x\theta_J(x) = 2\pi\rho_N(x).$$

with

$$[\rho_N(x), \theta_N(x')] = [\rho_J(x), \theta_J(x')] = i\sum_n \delta(x - x' + nL),$$
$$[\rho_N(x), \theta_J(x')] = [\rho_J(x), \theta_N(x')] = 0$$

The fields $(\rho_N(x), \theta_N(x))$ and $(\rho_J(x), \theta_J(x))$ are canonically conjugate pairs. Expressing ρ_N and the field $\phi_N(x)$ in terms of the boson operators from Eq. (3.21) and Eq. (3.22) one obtains:

$$\rho_N(x) = \left(\frac{N}{L}\right) + \sum_{q\neq 0} \sqrt{|q|/2\pi L}\; e^{iqx}(a_q^\dagger + a_{-q}), \tag{3.63}$$

$$\rho_J(x) = \left(\frac{J}{L}\right) + \sum_{q\neq 0} \sqrt{|q|/2\pi L}\; \mathrm{sgn}(q) e^{iqx}(a_q^\dagger - a_{-q}), \tag{3.64}$$

$$\phi_N(x) = \left(\frac{N}{L}\right)\pi x + i\sum_{q\neq 0} \sqrt{2\pi/L|q|}\; e^{-iqx}a_q, \tag{3.65}$$

$$\phi_J(x) = \left(\frac{N}{L}\right)\pi x + i\sum_{q\neq 0} \sqrt{2\pi/L|q|}\; \mathrm{sgn}(q) e^{-iqx}a_q. \tag{3.66}$$

In the phase field variables, the Hamiltonian 3.44 can be expressed as:

$$H_0 = \frac{v_F}{\pi}\int \mathrm{d}x : \big(\partial_x\theta_N(x)\big)^2 + \big(\partial_x\theta_J(x)\big)^2 : \tag{3.67}$$

With this, we complete the boson representation of a Fermi system under the corresponding physical considerations as discussed in the previous and in this chapter. In the next section we will study the interactions in the Tomonaga-Luttinger model.

3.2 Interacting model

In this section we will study the interacting part of the Tomonaga-Luttinger model. Two cases are to be discuss: spin-independent systems and systems including the spin degree of freedom. First we will discuss the spinless case, and then we will be able to extend the results to the case with spin[6].

Spinless case

In chapter 2 we discussed the possible interacting processes for both spinless case and the case with spin-1/2. In this section, we will make use of all the machinery constructed to write the full Hamiltonian of the Tomonaga-Luttinger model and solve it. The interacting spinless part, Eq. (2.14) is

$$H_{int} = \frac{\pi}{L}\sum_{r,q}\Big(g_2(q)\rho_r(q)\rho_{-r}(-q) + g_4(q)\rho_r(q)\rho_r(q)\Big), \tag{3.68}$$

Let us expand the Hamiltonian in terms of the operators a and $a^\dagger$ by using Eq. (3.30). The first term can be expressed then as:

$$\begin{aligned}
&\sum_{r,q} g_2(q)\rho_r(q)\rho_{-r}(-q) = \\
&\sum_{r,q} g_2(q)\Big(N_r\delta_{q0} + \sqrt{\frac{L|q|}{2\pi}}\big(\theta(rq)a_q^\dagger + \theta(-rq)a_{-q}\big)\Big)\times \\
&\quad\Big(N_{-r}\delta_{-q,0} + \sqrt{\frac{L|q|}{2\pi}}\big(\theta(rq)a_q^\dagger + \theta(-rq)a_q\big)\Big) \\
&= g_{20}\sum_r N_r N_{-r} + \frac{L}{2\pi}\sum_{q\neq 0} g_2(q)|q|\big(a_q^\dagger a_{-q}^\dagger + a_q a_{-q}\big).
\end{aligned} \tag{3.69}$$

Where $g_{20} = g_2(q=0)$. The last line was obtained by using the fact that $g_2(q) = g_2(-q)$. By performing the corresponding substitution in the second term, we obtain

$$\sum_{qr} g_4(q)\rho_r(q)\rho_r(-q) = g_{40}\sum_r N_r^2 + \frac{L}{2\pi}\sum_{q\neq 0} g_4(q)|q|\big(a_q^\dagger a_q + a_q a_q^\dagger\big). \tag{3.70}$$

The full Hamiltonian turns into

$$\begin{aligned}
&H = H_0 + H_{int} = \\
&v_F\sum_{q\neq 0}|q|a_q^\dagger a_q + \frac{1}{2}\sum_{q\neq 0} g_2(q)|q|\big(a_q^\dagger a_{-q}^\dagger + a_q a_{-q}\big) + \frac{1}{2}\sum_{q\neq 0} g_4(q)|q|\big(a_q^\dagger a_q + a_q a_q^\dagger\big) \\
&+ \frac{\pi}{L}g_{20}\sum_r N_r N_{-r} + \frac{\pi}{L}(g_{40}+v_F)\sum_r N_r^2
\end{aligned} \tag{3.71}$$

The last two terms in the Hamiltonian can be expressed as

$$\frac{\pi}{L}g_{20}\sum_r N_r N_{-r} + \frac{\pi}{L}(g_{40}+v_F)\sum_r N_r^2 = \frac{\pi}{2L}\Big(v_j J^2 + v_N(N-N_0)^2\Big), \tag{3.72}$$

[6] We especially recommend the paper by Haldane [14] and the book by Giamarchi [13].

where we introduced the following definitions:

$$v_j = v_F + g_{40} - g_{20}$$
$$v_N = v_F + g_{40} + g_{20}$$

Applying the commutation relations from Eq. (3.25), we write the total Hamiltonian as

$$H = \frac{1}{2}\sum_{q\neq 0}|q|\Big[g_2(q)(a_q^\dagger a_{-q}^\dagger + a_q a_{-q}) + (v_F + g_4(q))(a_q^\dagger a_q + a_q a_q^\dagger)\Big] + \frac{\pi}{2L}\big(v_j J^2 + v_N(N-N_0)^2\big) - \frac{1}{2}\sum_{q\neq 0} v_F|q|. \tag{3.73}$$

We would like now to diagonalize this Hamiltonian. Observe that, because the Hamiltonian consists of terms of the form $a_q^\dagger a_q$, $a_q^\dagger a_{-q}^\dagger$, and $a_q a_{-q}$, it should be possible to introduce a linear combination of the boson operators to solve Hamiltonian (3.73). Let us define

$$b_q \equiv \alpha_q a_q - \beta_q a_{-q}^\dagger. \tag{3.74}$$

α and β are real values and only depend on the absolute value of q, just as the coupling interactions $g_{2,4}$. We should make sure that the new operators satisfy the boson commutation relations, i.e., $[b_q, b_{q'}^\dagger] = \delta_{q,q'}$. The calculation of the commutator renders

$$\big[\alpha_q a_q - \beta_q \alpha_{-q}^\dagger, \alpha_{q'} a_{q'}^\dagger - \beta_{q'}\alpha_{-q'}\big] = \delta_{q,q'}(\alpha_q^2 - \beta_q^2). \tag{3.75}$$

From the result above, we have $\alpha_q^2 - \beta_q^2 = 1$, which indicates that α and β can be expressed using the functions cosh and sinh, respectively. Then the b operator can be written as[7]

$$b_q = \cosh\xi_q a_q - \sinh\xi_q a_{-q}^\dagger, \tag{3.76}$$

equally, ξ_q is assumed to be real and depends only on $|q|$. From the above, we can now invert the equation for b_q and write the boson operators a_q and $a_q^\dagger$ as

$$a_q^\dagger = \cosh\xi_q b_q^\dagger + \sinh\xi_q b_{-q}$$
$$a_q = \cosh\xi_q b_q + \sinh\xi_q b_{-q}^\dagger. \tag{3.77}$$

Let us now insert these expressions into the first term of Eq. (3.73),

$$\begin{aligned} &g_2(q)(a_q^\dagger a_{-q}^\dagger + a_q a_{-q}) + (v_F + g_4(q))(a_q^\dagger a_q + a_q a_q^\dagger) \\ &= \big(\alpha_q\beta_q g_{2q} + \alpha_q^2(g_{4q} + v_F)\big)(b_q^\dagger b_q + b_q b_q^\dagger) \\ &+ \big(\alpha_q\beta_q g_{2q} + \beta_q^2(g_{4q} + v_F)\big)(b_{-q}^\dagger b_{-q} + b_{-q} b_{-q}^\dagger) \\ &+ \big((\alpha^2+\beta^2)g_{2q} + 2\alpha_q\beta_q(g_{4q} + v_F)\big)(b_q^\dagger b_{-q}^\dagger + b_q b_{-q}). \end{aligned} \tag{3.78}$$

Should the last line in this equation vanish, the interacting Hamiltonian would reduce to an expression easily diagonalizable. Such requirement would give place to the next condition

$$(\cosh\xi_q{}^2 + \sinh\xi_q{}^2)g_{2q} + 2\cosh\xi_q\sinh\xi_q(g_{4q} + v_F) = 0. \tag{3.79}$$

Using the properties of cosh and sinh functions, the equation above leads to the definition of ξ_q,

$$\tanh 2\xi_q = -\frac{g_{2q}}{v_F + g_{4q}}. \tag{3.80}$$

[7] This actually means to carry on a unitary transformation of a_q and $a_q^\dagger$, i. e. $b_q = S a_q S^\dagger$, with S an hermitian operator, so that $SS^\dagger = \mathbb{1}$. In this case this is a Bogoliubov transformation.

With this definition, the first term of the Hamiltonian 3.73 is,

$$\begin{aligned}
&\frac{1}{2}\sum_{q\neq 0}|q|\Big[g_2(q)(a_q^\dagger a_{-q}^\dagger + a_q a_{-q}) + (v_F + g_4(q))(a_q^\dagger a_q + a_q a_q^\dagger)\Big] \\
&= \frac{1}{2}\sum_{q\neq 0}|q|\Big[2\alpha_q\beta_q g_{2q} + (\alpha_q^2+\beta_q^2)(v_F+g_{40})\Big](b_q^\dagger b_q + b_q b_q^\dagger) \\
&= \frac{1}{2}\sum_{q\neq 0}|q|\sqrt{(v_F+g_{4q})^2-(g_{2q})^2}(b_q^\dagger b_q + b_q b_q^\dagger),
\end{aligned} \tag{3.81}$$

We conclude that the full interacting fermion Hamiltonian from Eq. (3.73) can be mapped onto a free bosonic one as,

$$\begin{aligned}
H &= E_0 + \sum_{q\neq 0}\omega_q b_q^\dagger b_q + \frac{\pi}{2L}\big(v_j J^2 + v_N(N-N_0)^2\big) \\
E_0 &= \frac{1}{2}\sum_{q\neq 0}(\omega_q - v_F|q|) \\
\omega_q &= |q|\sqrt{(v_F+g_{4q})^2-(g_{2q})^2}.
\end{aligned} \tag{3.82}$$

Spinful case

The inclusion of spin degrees of freedom, $\sigma = \uparrow, \downarrow$, leaves the boson and number operators with analogous definitions as for the spinless case, only with an extra spin index. A significant difference is the introduction of another type of interaction in the Hamiltonian. Due to the fact that the backward scattering process can no longer be considered an effective forward scattering process, and $g_{1\perp} \neq g_{2\perp}$, we have to consider the interaction g_1. The interacting Hamiltonian becomes therefore:

$$H_{int} = H_1 + H_2 + H_4, \tag{3.83}$$

$$\begin{aligned}
H_1 &= \frac{1}{L}\sum_{k,k',q,\sigma,\sigma'} g_1 c_{+,k,\sigma}^\dagger c_{-,k',\sigma'}^\dagger c_{+,k'+2k_F+q,\sigma'} c_{-,k-2k_F-q,\sigma}, \\
H_2 &= \int \mathrm{d}x \sum_\sigma \Big\{ g_{2\parallel}\rho_{+,\sigma}(x)\rho_{-,\sigma}(x) + g_{2\perp}\rho_{+,\sigma}(x)\rho_{-,-\sigma}(x)\Big\} \\
H_4 &= \int \mathrm{d}x \sum_{r,\sigma} \Big\{ \frac{g_{4\parallel}}{2}\rho_{r,\sigma}(x)\rho_{r,\sigma}(x) + \frac{g_{4\perp}}{2}\rho_{r,\sigma}(x)\rho_{r,-\sigma}(x)\Big\}
\end{aligned} \tag{3.84}$$

The Hamiltonian above is no longer diagonal in the spin index, as the interaction couples up- with down-spins. To diagonalize it (observe that the Hamiltonian is still quadratic in the fields ϕ and θ), one introduces the spinful definitions for operators and fields. For the density operator, analog to Eq. (3.13), we have:

$$\rho_{r\sigma} \equiv :\psi_{r\sigma}^\dagger \psi_{r\sigma}: \tag{3.85}$$

and we recall that the charge and spin densities, see Eq. (3.20) and Eq. (3.20), in real space are:

$$\begin{aligned}
\rho_c(x) &= \frac{1}{\sqrt{2}}\big[\rho_\uparrow(x) + \rho_\downarrow(x)\big], \\
\rho_s(x) &= \frac{1}{\sqrt{2}}\big[\rho_\uparrow(x) - \rho_\downarrow(x)\big].
\end{aligned} \tag{3.86}$$

The boson fields are

$$\phi_c(x) = \frac{1}{\sqrt{2}}\big[\phi_\uparrow(x) + \phi_\downarrow(x)\big],$$
$$\phi_s(x) = \frac{1}{\sqrt{2}}\big[\phi_\uparrow(x) - \phi_\downarrow(x)\big]. \tag{3.87}$$

An analog relation corresponds to the $\theta(x)$ fields. In terms of these fields, H_2 and H_4 become

$$H_2 = \frac{1}{4\pi}\int \mathrm{d}x\big[g_{2\parallel} + g_{2\perp}\big]\Big((\partial_x\phi_c(x))^2 - (\partial_x\theta_c(x))^2\Big) + \big[g_{2\parallel} - g_{2\perp}\big]\Big((\partial_x\phi_s(x))^2 - (\partial_x\theta_s(x))^2\Big) \tag{3.88}$$

and

$$H_4 = \frac{1}{4\pi}\int \mathrm{d}x\big[g_{4\parallel} + g_{4\perp}\big]\Big((\partial_x\phi_c(x))^2 + (\partial_x\theta_c(x))^2\Big) + \big[g_{4\parallel} + g_{4\perp}\big]\Big((\partial_x\phi_s(x))^2 + (\partial_x\theta_s(x))^2\Big) \tag{3.89}$$

The $g_{1\perp}$-term can be bosonized rendering

$$H_1 = \int \mathrm{d}x \frac{g_{1\perp}}{(2\pi\alpha)^2}\sum_{s=\uparrow,\downarrow}\big[e^{i(-2\phi_s(x))} + e^{i(-2\phi_{-s}(x))}\big]$$
$$= \int \mathrm{d}x \frac{g_{1\perp}}{(2\pi\alpha)^2}\cos\Big(2\sqrt{(}2)\ \phi_\sigma(x)\Big) \tag{3.90}$$

We have now two decoupled sectors corresponding to charge and spin excitations, thus $H = H_c + H_s$. Let us, for each sector $\lambda = c, s$ define the next coupling constants and velocities:

$$K_\lambda \equiv \sqrt{\frac{2\pi v_F + g_{4\lambda} - g_{2\lambda}}{2\pi v_F + g_{4\lambda} + g_{2\lambda}}} \tag{3.91}$$

$$u_\lambda \equiv v_F\sqrt{\Big(1 + \frac{g_{4\lambda}}{2\pi v_F}\Big)^2 - \Big(\frac{g_{2\lambda}}{2\pi v_F}\Big)} \tag{3.92}$$

3.3 Correlation functions

In one-dimensional systems, with short-range interactions, the $T = 0$ point represents a quantum critical point. This can be characterized through the corresponding correlation functions at $T = 0$. In systems of $D > 1$, the correlation functions give information about the tendency of the system to show long-range order. In 1D though, criticality manifest itself in an algebraic decay of the correlation functions.

With charge and spin dynamics already decoupled, we can define the operators for each sector. For the charge sector we have the total density operator

$$O_c(x) = \sum_{r,\sigma} : \psi^\dagger_{r,\sigma}(x)\psi_{r,\sigma}(x) : \tag{3.93}$$

with $q \sim 2k_F$ and $q \sim 4k_F$ components given by

$$O_{CDW}(x) = \sum_\sigma e^{-2ik_Fx}\psi^\dagger_{+,\sigma}(x)\psi_{-,\sigma}(x), \tag{3.94}$$

$$O_{4k_F}(x) = e^{-4ik_Fx}\psi^\dagger_{+,\sigma}(x)\psi^\dagger_{+,-\sigma}(x)\psi_{-,-\sigma}(x)\psi_{-,\sigma}(x). \tag{3.95}$$

the $q \sim 0$ component, as we will see below, decays as $1/r^2$ for long distances r. For the spin sector, the total density operator and $q \sim 2k_F$ component are

$$O_s(x) = \sum_{r,\mu,\nu} \sigma^3_{\mu,\nu} : \psi^\dagger_{r,\mu}(x)\psi_{r,\nu}(x) :, \tag{3.96}$$

$$O^a_{SDW}(x) = \sum_{\mu,\nu} e^{-2ik_F x}\sigma^a_{\mu,\nu}\psi^\dagger_{+,\mu}(x)\psi_{-,\nu}(x), \tag{3.97}$$

where $\sigma^a_{\mu,\nu}$ is the μ,ν elements of the a-th Pauli matrix, $\mu,\nu = \pm 1$, $a = 1,2,3$. We are now interested in the correlation functions, which are defined as $C_\lambda(x) \equiv \langle O_\lambda(x) O^\dagger_\lambda(x)\rangle$. The results are summarized in the next,

$$\begin{aligned} C_c(x) &= \tfrac{K_c}{(\pi x)^2} & C_s(x) &= \tfrac{K_s}{(\pi x)^2} \\ C_{CDW}(x) &\sim \tfrac{\cos(2k_F x)}{x^{K_c+K_s}} & C^z_{SDW}(x) &\sim \tfrac{\cos(2k_F x)}{x^{K_c+K_s}} \\ C_{4K_F}(x) &\sim \tfrac{\cos(4k_F x)}{x^{4K_c}} & C^{x,y}_{SDW}(x) &\sim \tfrac{\cos(2k_F x)}{x^{(K_c+\frac{1}{K_s})}} \end{aligned}$$

A logarithmic correction of the density-density correlation function was carried out by Giamarchi [12], so one obtains:

$$\langle \rho_c(x)\rho_c(0)\rangle = \frac{K_c}{(\pi x)^2} + \frac{A_1\cos(2k_F x)}{x^{1+K_c}}\ln(\mathrm{x})^{-\frac{3}{2}} + \frac{A_2\cos(4k_F x)}{x^{4K_c}} + \ldots. \tag{3.98}$$

This is the form of the density-density correlations that we will use to study the systems to be proposed in the next chapter.

Summary

In this chapter we have employed the method of bosonization to solve the Tomonaga-Luttinger model of one-dimensional interacting systems. We learned that in the low-energy regime there is an equivalence between a fermionic and a bosonic representation, the last one being easier to treat since the Hamiltonian, free and interacting, reduces to quadratic terms in the new bosonic variables and this can be solved by a usual Bogoliubov transformation. We also learned that the systems decouple in independent spin and charge sectors of different group velocities, in contrast to the high-dimensional case of a Fermi liquid. This phenomenon is well-known under the name of *spin-charge separation* and is one of the Tomonaga-Luttinger liquid benchmarks. We found also that K_λ is a relevant parameter that characterizes the decay of the correlation functions. It is also clear that up to now there is no way to estimate it, if the couplings are unknown. One aspect of this work will be the calculation of K_c from the measurement of the density-density correlation function.

Chapter 4

One-dimensional inhomogeneous systems

When we consider the experimental progress and the results we discussed in chapter 1, it is no wonder that a great effort is being invested in the study of the properties of one-dimensional strongly correlated electron systems. In this sense, to investigate the low-energy ($T = 0K$) properties of one-dimensional inhomogeneous systems, we will turn to the one-dimensional Hubbard model which has been one of the most helpful models of strongly correlated electron systems. While appearing simple, as it only consists of two terms, it is by no means a trivial model. It has been used in the study of a wide variety of phenomena including metal-insulator transition, ferrimagnetism, antiferromagnetism, ferromagnetism, superconductivity and Tomonaga-Luttinger liquid. The one-dimensional Hubbard model is one of the rare examples of an exactly solvable model for spin-1/2 fermions. It was solved using the Bethe Ansatz [24], which is a powerful analytical technique to treat one-dimensional systems. The method was first used by Bethe to solve the isotropic Heisenberg Hamiltonian [4] and was later successfully applied to other models. This original method is now known as the *coordinate* Bethe Ansatz (CBA). It was further developed by Baxter [19] and other representatives of the Russian school, giving rise to the quantum inverse scattering method (QISM).

In this chapter we will first describe the one-dimensional Hubbard model, and see that the Bethe Ansatz can be a good approach to solve it. General properties of this model will also be discussed. At the end we will write the Hubbard model for the case of inhomogeneous systems and define in this way the heterostructures we study in this thesis.

4.1 One-dimensional Hubbard model

The Hubbard model, as described by Ashcroft and Mermin [3], is a *highly oversimplified model* for electrons propagating in a solid and interacting with each other through short-ranged Coulomb interactions. The Hamiltonian of the Hubbard model consists of two parts: H_0, which describes the propagating electrons, as they hop from one site to another; and H_U, which describes the effect of two electrons sitting in the same site, i.e, the on-site Coulomb interaction. Each term on their own offers no big difficulties, but if their energy scales are comparable both terms must be considered, leading to a competing process that takes place between the kinetic term trying to delocalize the electrons and the on-site Coulomb interaction trying to do the opposite. The physics then becomes non-trivial.

Given a lattice of length L sites and a total of N electrons the Hubbard Hamiltonian is

$$H = H_0 + H_U, \tag{4.1}$$

with kinetic term

$$H_0 = \sum_{<ij>} \sum_{\sigma} -t_{ij} \left(c^{\dagger}_{i,\sigma} c_{j,\sigma} + c^{\dagger}_{j,\sigma} c_{i,\sigma} \right) \tag{4.2}$$

where $c^{\dagger}_{i,\sigma}$, $c_{i,\sigma}$ are the creation and annihilation fermion operators, respectively, with spin $\sigma = \uparrow, \downarrow$ on the site i. The hopping amplitude $t_{ij} = t_{ji} = t > 0$ represents the probability that an electrons hops from site i to site j, and it is usually assumed to be real. $< ij >$

implies that the sum is done over the nearest-neighboring sites. The interacting term is

$$H_U = \sum_i U_i n_{i,\uparrow} n_{i,\downarrow}, \tag{4.3}$$

where $n_{i\sigma} = c^\dagger_{i,\sigma} c_{i,\sigma}$ is the electron number operator. For our purposes, $U_i > 0$, i.e., we will describe repulsive interactions. This term describes the gain in the energy, by U_i, when two electrons occupy a single orbital state at i. The fermion operators obey the canonical anticommutation relations,

$$\left\{c^\dagger_{i,\sigma}, c_{i',\sigma'}\right\} = \delta_{ii'}\delta_{\sigma\sigma'}$$
$$\left\{c^\dagger_{i,\sigma}, c^\dagger_{i',\sigma'}\right\} = \left\{c_{i,\sigma}, c_{i',\sigma'}\right\} = 0.$$

Now let us investigate some basic conserved quantities. It is easy to check that the total-number operator

$$N = \sum_i \left(n_{i,\uparrow} + n_{i,\downarrow}\right) \tag{4.4}$$

commutes with the Hamiltonian H, and since each lattice site has at most two electrons, $0 \leq N \leq 2L$, where N is the number of particles and L is the length of the chain. It also conserves the number of down-spins M (similarly of M' up-spins), so we find

$$\left[\sum_i n_{i\uparrow}, H\right] = \left[\sum_i n_{i\downarrow}, H\right] = 0. \tag{4.5}$$

The Hubbard Hamiltonian is as well invariant under a particle-hole transformation and under reversal of all spins.

4.1.1 Bethe Ansatz solution (PBC)

The eigenvalue problem for the Hubbard Hamiltonian with periodic boundary conditions (PBC) was solved by Lieb and Wu [24, 25] using the CBA. They proved in the end that the ground state corresponds to an antiferromagnet and a Mott transition takes place.

We saw in the previous section that the number of down-spins M as well as that of up-spins M' are conserved. This fact allows us to characterize the eigenstates of the system by using these quantities. We can write then the Schrödinger equation as

$$H|M, M'\rangle = E(M, M')|M, M'\rangle \tag{4.6}$$

with $N = M + M'$, and we will restrict to a particle number of N such that $N \leq L$, i.e., the band is half-filled at most[1]. The eigenstate $|M, M'\rangle$ can be expressed as a superposition of all the states $|x_1 x_2 \ldots x_N\rangle$ in which all the down-spin electrons are located at the sites $x_1, x_2, \ldots, x_M$, and the up-spin electrons are at sites given by the coordinates $x_{M+1}, \ldots, x_N$. A particular ordering of the particles, which we can call a *sector* Q, is given by

$$x_{Q1} \leq x_{Q2} \leq \ldots \leq x_{QN} \tag{4.7}$$

where $Q = \{Q1, Q2, \ldots, QN\}$ is a permutation that maps the ordered set $\{1, 2, \ldots, N\}$ into $\{Q1, Q2, \ldots, QN\}$, so in 4.7, it is meant that the particle $Q1$ is in the first position, $Q2$ in the second, etc. In total there are $N!$ permutations and corresponding sectors Q.

[1] For fixed M and M', the solution to Eq. (4.6) is not uniquely determined. To restrict the solutions one makes use of the particle-hole invariance and finds that $N \leq L$.

The union of these sectors gives the full configuration space. Furthermore, such sectors are disjoint except for their boundaries, for which $x_{Qi} = x_{Q(i+1)}$.

Let us proceed, then, to diagonalize the Hamiltonian in Eq. (4.6). An arbitrary form of the eigenstate $|M, M'\rangle$ is

$$|M, M'\rangle = \sum_{x_1 \leq x_2 \leq \ \ldots \ \leq x_N} a_{\sigma_1 \ \ldots \ \sigma_N}(x_1, x_2, \ \ldots \ , x_N)|x_1 x_2 \ \ldots \ x_N\rangle, \tag{4.8}$$

where the summation is over all x_i, from 1 to N, and $a_{\sigma_1 \ldots \sigma_N}(x_1, x_2, \ldots, x_N)$ is the amplitude of the state $|x_1 x_2 \ldots x_N\rangle$ with spin projections σ_i.

Next, we substitute Eq. (4.8) in the Schrödinger equation, Eq. (4.6), and obtain for the amplitudes (setting $t_{ij} = 1$)

$$\begin{aligned} &- \sum_{i}^{N} \left[a_{\sigma_1 \ldots \sigma_N}(x_1, \ldots, x_i + 1, \ldots, x_N) + a_{\sigma_1 \ldots \sigma_N}(x_1, \ldots, x_i - 1, \ldots, x_N) \right] \\ &+ U \sum_{i<j} \delta(x_i - x_j) \delta_{\sigma_i, -\sigma_j} a_{\sigma_1 \ldots \sigma_N}(x_1, \ldots, x_N) = E a_{\sigma_1 \ldots \sigma_N}(x_1, \ldots, x_N) \end{aligned} \tag{4.9}$$

Since we are working with fermions, the amplitude $a_{\sigma_1 \ldots \sigma_N}(x_1, x_2, \ldots, x_N)$ is required to be antisymmetric *separately* in both the M- and in the M'-region. This condition also ensures that the amplitude will be zero if any two x's are equal in the same subset, thus the only relevant delta-function terms in 4.9 are the ones with $i \leq M$ and $j > M$, i.e., the only interaction is between the up- and down-spins. We now proceed to solve 4.9 for the amplitudes a and the energy E, keeping in mind that site 1 is the same as the site $N + 1$ for the boundary condition to be periodic. We will find the proceeding in steps. First we will consider a system with one electron in the chain, then with two electrons, and finally we can generalize the solution to N electrons.

Case I: One electron in the chain. In this case, Eq. (4.9) reduces to

$$- a_\sigma(x - 1) - a_\sigma(x + 1) = E a_\sigma(x) \tag{4.10}$$

whose solution is

$$a_\sigma(x) = e^{ipx} a_\sigma, \tag{4.11}$$

with a_σ a normalization constant. And for the energy eigenvalue

$$E = -2 \cos p. \tag{4.12}$$

Case II: Two electrons in the chain. Now we have to consider two cases: when the electrons are located at different sites, and therefore they do not interact with each other (the U term vanishes), and when the electrons are able to interact in the same site.

If the electrons are at different sites, x_1 and x_2, Eq. (4.9) becomes

$$\begin{aligned} &- a_{\sigma_1 \sigma_2}(x_1 - 1, x_2) - a_{\sigma_1 \sigma_2}(x_1 + 1, x_2) \\ &- a_{\sigma_1 \sigma_2}(x_1, x_2 - 1) - a_{\sigma_1 \sigma_2}(x_1, x_2 + 1) \\ &= E a_{\sigma_1 \sigma_2}(x_1, x_2). \end{aligned} \tag{4.13}$$

The solution in this case is

$$a_{\sigma_1 \sigma_2}(x_1, x_2) = c_{1_{\sigma_1 \sigma_2}} e^{ip_1 x_1 + ip_2 x_2} - c_{2_{\sigma_1 \sigma_2}} e^{ip_2 x_1 + ip_1 x_2} \tag{4.14}$$

with c_1 and c_2 arbitrary constants, and energy

$$E = -2(\cos p_1 + \cos p_2). \tag{4.15}$$

In the case that the two electrons are neighbors with opposite spin, it is possible for them to interact in the same site $x_1 = x_2 = x$, then Eq. (4.9) becomes

$$\begin{aligned}
&- a_{\sigma_1\sigma_2}(x-1,x) - a_{\sigma_1\sigma_2}(x+1,x) \\
&- a_{\sigma_1\sigma_2}(x,x-1) - a_{\sigma_1\sigma_2}(x,x+1) \\
&+ U\delta_{\sigma_1,-\sigma_2} a_{\sigma_1\sigma_2}(x,x) \\
&= E a_{\sigma_1\sigma_2}(x,x).
\end{aligned} \tag{4.16}$$

To find the solution we have to consider two different configurations, namely $x_1 < x_2$ and $x_2 < x_1$. If $x_1 < x_2$ we have,

$$a_{\sigma_1\sigma_2}(x_1,x_2) = A_{\sigma_1\sigma_2}(p_1,p_2)e^{ip_1x_1+ip_2x_2} - A_{\sigma_1\sigma_2}(p_2,p_1)e^{ip_2x_1+ip_1x_2}, \tag{4.17}$$

if $x_2 < x_1$, then

$$a_{\sigma_1\sigma_2}(x_1,x_2) = A_{\sigma_2\sigma_1}(p_2,p_1)e^{ip_1x_1+ip_2x_2} - A_{\sigma_2\sigma_1}(p_1,p_2)e^{ip_2x_1+ip_1x_2}. \tag{4.18}$$

Equations (4.17) and (4.18) can be unified for the region $x_{Q_1} < x_{Q_2}$ as

$$a_{\sigma_1\sigma_2}(x_1,x_2) = \sum_P (-1)^{\eta_P} A_{\sigma_{Q_1}\sigma_{Q_2}}(P,Q)e^{i(p_{P_1}x_1+p_{P_2}x_2)} \tag{4.19}$$

where P and Q are the two permutations of the particles for momenta p_i and coordinates x_i. The expression includes the antisymmetry condition under exchange of two electrons, and since we are considering PBC, the continuity of the wavefunction at $x_1 = x_2$ means that the amplitudes in (4.17) and in (4.18) must satisfy,

$$A_{\sigma_1\sigma_2}(p_1,p_2) - A_{\sigma_1\sigma_2}(p_2,p_1) = A_{\sigma_2\sigma_1}(p_2,p_1) - A_{\sigma_2\sigma_1}(p_1,p_2). \tag{4.20}$$

Upon substitution of (4.19) into Eq. (4.16), we obtain

$$\begin{aligned}
&- 2(\cos p_1 + \cos p_2)\big[A_{\sigma_1\sigma_2}(p_1,p_2) - A_{\sigma_1\sigma_2}(p_2,p_1)\big] \\
&= E\big[A_{\sigma_1\sigma_2}(p_1,p_2) - A_{\sigma_1\sigma_2}(p_2,p_1)\big] \\
&+ \big(e^{ip_1} - e^{-ip_1} - e^{ip_2} + e^{-ip_2}\big) \times \big[A_{\sigma_2\sigma_1}(p_2,p_1) - A_{\sigma_1\sigma_2}(p_1,p_2)\big] \\
&- U\big[A_{\sigma_1\sigma_2}(p_1,p_2) - A_{\sigma_1\sigma_2}(p_2,p_1)\big],
\end{aligned} \tag{4.21}$$

which can be also expressed as

$$\begin{aligned}
&- 2(\cos p_1 + \cos p_2)\big[A_{\sigma_1\sigma_2}(p_1,p_2) - A_{\sigma_1\sigma_2}(p_2,p_1)\big] \\
&= E\big[A_{\sigma_1\sigma_2}(p_1,p_2) - A_{\sigma_1\sigma_2}(p_2,p_1)\big] \\
&+ \Big\{2i\big(\sin p_1 - \sin p_2\big) \times \big[A_{\sigma_2\sigma_1}(p_2,p_1) - A_{\sigma_2\sigma_1}(p_1,p_2)\big] \\
&- U\big[A_{\sigma_1\sigma_2}(p_1,p_2) - A_{\sigma_1\sigma_2}(p_2,p_1)\big]\Big\}.
\end{aligned} \tag{4.22}$$

This result looks like an equation for the eigenfunction $\big[A_{\sigma_1\sigma_2}(p_1,p_2) - A_{\sigma_1\sigma_2}(p_2,p_1)\big]$ with eigenvalue (4.15) if the expression in braces vanishes, i.e., if

$$\begin{aligned}
&2i\big(\sin p_1 - \sin p_2\big) \times \big[A_{\sigma_2\sigma_1}(p_2,p_1) - A_{\sigma_2\sigma_1}(p_1,p_2)\big] \\
&- U\big[A_{\sigma_1\sigma_2}(p_1,p_2) - A_{\sigma_1\sigma_2}(p_2,p_1)\big] = 0,
\end{aligned} \tag{4.23}$$

from which we find the next relation between the amplitudes

$$A_{\sigma_1\sigma_2}(p_2,p_1) = \frac{-U/2i}{\sin p_1 - \sin p_2 - U/2i} A_{\sigma_1\sigma_2}(p_1,p_2) + \frac{\sin p_1 - \sin p_2}{\sin p_1 - \sin p_2 - U/2i} A_{\sigma_2\sigma_1}(p_1,p_2), \tag{4.24}$$

which can be written using matrix representation as

$$A_{\sigma_1\sigma_2}(p_2,p_1) = \sum_{\sigma_{1'}\sigma_{2'}} S^{\sigma_1\sigma_{1'}}_{\sigma_2\sigma_{2'}}(p_1,p_2) A_{\sigma_{1'}\sigma_{2'}}(p_1,p_2), \tag{4.25}$$

where

$$S^{\sigma_1\sigma_{1'}}_{\sigma_2\sigma_{2'}}(p_1,p_2) = +\frac{\sin p_1 - \sin p_2}{\sin p_1 - \sin p_2 - U/2i}\delta_{\sigma_1,\sigma_{1'}}\delta_{\sigma_2,\sigma_{2'}} + \frac{-U/2i}{\sin p_1 - \sin p_2 - U/2i}\delta_{\sigma_1,\sigma_{2'}}\delta_{\sigma_2,\sigma_{1'}} \tag{4.26}$$

is called the S-matrix. It is in general regarded as a two-particle scattering matrix between an interacting pair of particles at sites i and j, and relates the amplitudes in the two regions without interfering with the other $N-2$ regions. Let us try now to generalize the previous construction to N particles. We remember that the full configuration space is divided into $N!$ sectors according to the ordering of the particles on the chain, and are labeled by elements of the permutation group. For example, the sector $x_3 < x_1 < x_7 < \ \ldots$ is labeled by the permutation $Q = \{Q1 = 3, Q2 = 1, Q3 = 7, \ \ldots\}$. In the interior of the regions there are no interactions, thus the wavefunction will be given as a sum of the product of single-particle wavefunctions, i.e., as the sum of plane waves. In the case a boundary is crossed, two particles are then interacting. Since there are no other multiparticle interactions, we can summarize the interacting effects using a general form of the S-matrix. We thus consider wavefunctions of the Bethe form:

$$\sum_P (-1)^{\eta_P} A_{\sigma_{Q_1}\sigma_{Q_2}\ldots\sigma_{Q_N}}(P,Q) e^{i[p_{P_1}x_{Q_1} + p_{P_2}x_{Q_2} + \ \ldots\ + p_{P_N}x_{Q_N}]}, \tag{4.27}$$

which is known as the Bethe Ansatz. η_P indicates the parity of the permutation and ensures the antisymmetry of the wavefunction. P and Q are elements of the configuration space. The Ansatz is a superposition of plane waves [2] with wave numbers p_j and (complex) amplitudes $A_{\sigma_{Q_1}\sigma_{Q_2}\ldots\sigma_{Q_N}}(P,Q) \equiv A_{\sigma_1\sigma_2\ldots\sigma_N}(Q|P)$, where the term to the right indicates only a different notation. Correspondingly, the energy and total momentum are given by

$$E = \sum_j -2t\cos p_j \tag{4.28}$$

$$P = \sum_j p_j. \tag{4.29}$$

The amplitudes are related by the S-matrix by

$$A_{\ldots\sigma_i\ldots\sigma_j\ldots}(\tilde{Q}|P) = \sum_{\sigma_{i'}\sigma_{j'}} S^{\sigma_i\sigma_{i'}}_{\sigma_j\sigma_{j'}}(p_i,p_j) A_{\ldots\sigma_{i'}\ldots\sigma_{j'}\ldots}(Q|P). \tag{4.30}$$

The relation between different elements of the S-matrix can be derived from a simple, but illustrative example: A three-particle initial state given by $(x_1 < x_2 <_3)$ is scattered to

[2] This is actually a generalization of the original CBA used to solve the Heisenberg chain. Here we do not only consider permutations of the p_j numbers but also of the coordinates x_j.

a final state ($x_3 < x_2 <_1$). The process to get to the final state is not unique. There are two ways to follow through intermediate states:

1. $-(x_1 < x_2 < x_3) \to (x_2 < x_1 < x_3) \to (x_2 < x_3 < x_1) \to (x_3 < x_2 < x_1)$,
2. $-(x_1 < x_2 < x_3) \to (x_1 < x_3 < x_2) \to (x_3 < x_1 < x_2) \to (x_3 < x_2 < x_1)$.

Both processes are equivalent, and this means that for the scattering matrices we have

$$\sum_{\sigma_{1'}\sigma_{2'}\sigma_{3'}} S^{\sigma_1\sigma_{1'}}_{\sigma_2\sigma_{2'}}(p_1,p_2) S^{\sigma_1\sigma_{1''}}_{\sigma_3\sigma_{3'}}(p_1,p_3) S^{\sigma_2\sigma_{2''}}_{\sigma_3\sigma_{3''}}(p_2,p_3) = \sum_{\sigma_{1'}\sigma_{2'}\sigma_{3'}} S^{\sigma_2\sigma_{2'}}_{\sigma_3\sigma_{3'}}(p_2,p_3) S^{\sigma_1\sigma_{1'}}_{\sigma_3\sigma_{3''}}(p_1,p_3) S^{\sigma_1\sigma_{1''}}_{\sigma_2\sigma_{2''}}(p_1,p_2). \tag{4.31}$$

Introducing the momentum parameterization $p_j = p_j(\lambda_j)$, such that the S-matrix depends only of the difference of the velocities, i.e., such that $S(p_1p_2) \to S(\lambda_1 - \lambda_2)$, then Eq. (4.31) can be written as

$$S^{\sigma_1\sigma_{1'}}_{\sigma_2\sigma_{2'}}(\lambda) S^{\sigma_1\sigma_{1''}}_{\sigma_3\sigma_{3'}}(\lambda+\mu) S^{\sigma_2\sigma_{2''}}_{\sigma_3\sigma_{3''}}(\mu) = S^{\sigma_2\sigma_{2'}}_{\sigma_3\sigma_{3'}}(\mu) S^{\sigma_1\sigma_{1'}}_{\sigma_3\sigma_{3''}}(\lambda+\mu) S^{\sigma_1\sigma_{1''}}_{\sigma_2\sigma_{2''}}(\lambda). \tag{4.32}$$

Repeated indices indicate a summation. Equations (4.32) are known as the Yang-Baxter equations [19], with λ called the spectral parameter. An artificial but helpful construction is that of the *transfer matrix* T, defined as follows

$$T^{\sigma_1\cdots\sigma_N}_{\tau_1\ldots\tau_N}(\lambda) = \sum_{\gamma_1\cdots\gamma_N} S^{\gamma_1\gamma_2}_{\sigma_1\tau_1}(\lambda) S^{\gamma_2\gamma_3}_{\sigma_2\tau_2}(\lambda)\cdots S^{\gamma_N\gamma_1}_{\sigma_N\tau_N}(\lambda), \tag{4.33}$$

The Hamilton operator can be expressed using either the S- or the transfer matrix, so that the diagonalization of the Hamiltonian reduces to diagonalizing the transfer matrix. When considering PBC, the eigenvalue problem takes the form

$$T_j A(I|I) = e^{iNp_j} A(I|I), \qquad \text{for j=1, ..., N.} \tag{4.34}$$

From this equation we see that, the jth electron will be dispersed by the other $N-1$ particles, and the whole set of events will be quantified through the S-matrix and summarized in the transfer matrix. After the electron has been transferred along the whole chain of length L, the wavefunction gains a wavefactor of e^{iLp_j}. From this analysis, one obtains a set of $N+M$ equations for the N parameters p_j and M additional equation for the set of λ_i, which parameterize the momentum:

$$e^{ip_jL} = \prod_{i=1}^{M} \frac{\lambda_i - \sin p_j + iU/4}{\lambda_i - \sin p_j - iU/4}, \qquad j = 1, 2, \ \ldots\ , N \tag{4.35}$$

$$\prod_{l=1}^{N} \frac{\lambda_i - \sin p_l + iU/4}{\lambda_i - \sin p_l - iU/4} = \prod_{\substack{k=1\\k\neq i}}^{M} \frac{\lambda_i - \lambda_k + iU/2}{\lambda_i - \lambda_k - iU/2}, \qquad i = 1, 2, \ \ldots\ , M \tag{4.36}$$

Eq. (4.35) results from the periodic boundary conditions imposed. Taking the logarithm on both sides, we obtain another pair of equations,

$$p_jL = 2\pi I_j + 2\sum_{i=1}^{M} \arctan\left(\frac{4}{U}(\lambda_i - \sin p_j)\right), \tag{4.37}$$

$$\sum_{j=1}^{N} 2\arctan\left(\frac{4}{U}(\lambda_i - \sin p_j)\right) = 2\pi J_i + \sum_{k=1}^{M} 2\arctan\left(\frac{2}{U}(\lambda_i - \lambda_k)\right), \tag{4.38}$$

where I_j and J_i are integers or half-integers. Adding up the first equation on j and the second on i, we obtain for the total momentum:

$$L\sum_{j=1}^{N} p_j = 2\pi\left(\sum_{j=1}^{N} I_j + \sum_{i=1}^{M} J_i\right). \tag{4.39}$$

4.1.2 Bethe Ansatz solution (OBC)

The analysis carried out previously is valid also for systems under open boundary conditions (OBC). This condition must be introduced when diagonalizing the Hamiltonian (in terms of the transfer matrix). Analog to Eq. (4.35) and Eq. (4.36), equations for momenta p_j and velocities λ_i are found for OBC and are given by (setting $p_0 = \lambda_0 = 0$ in this case) [31]

$$e^{2p_j(L+1)} = \prod_{i=1}^{M} \frac{(\sin(p_j) + iU/4)(\sin(p_j) + \lambda_i + iU/4)}{(\sin(p_j) - \lambda_i - iU/4)(\sin(p_j) + \lambda_i - iU/4)} \tag{4.40}$$

and

$$\begin{aligned}\prod_{l=1}^{N} \frac{(\lambda_i - \sin(p_l) + iU/4)(\lambda_i + \sin(p_l) + iU/4)}{(\lambda_i - \sin(p_l) - iU/4)(\lambda_i + \sin(p_l) - iU/4)} = \\ \prod_{\substack{k=1 \\ k\neq i}}^{M} \frac{(\lambda_i - \lambda_k + iU/2)(\lambda_i + \lambda_k + iU/2)}{(\lambda_i - \lambda_k - iU/2)(\lambda_i + \lambda_k - iU/2)}\end{aligned} \tag{4.41}$$

And, by taking again the logarithm on both sides, we obtain the following sets of equations:

$$2(L+1)p_j = 2\pi I_j - \sum_{i=1}^{M}\left\{2\arctan\left(\frac{4}{U}(\sin p_j - \lambda_i)\right) + 2\arctan\left(\frac{4}{U}(\sin p_j + \lambda_i)\right)\right\}, \tag{4.42}$$

and

$$\begin{aligned}\sum_{j=1}^{N}\left\{2\arctan\left(\frac{4}{U}(\lambda_i - \sin p_j)\right) + 2\arctan\left(\frac{4}{U}(\lambda_i + \sin p_j)\right)\right\} \\ = 2\pi J_i + \sum_{k=1}^{M}\left\{2\arctan\left(\frac{2}{U}(\lambda_i - \lambda_k)\right) + 2\arctan\left(\frac{2}{U}(\lambda_i + \lambda_k)\right)\right\}.\end{aligned} \tag{4.43}$$

Equations (4.37)-(4.38), and (4.42)-(4.43) can be solved by the method of Newton iteration[3]. Once with the set of p_j's one can calculate the ground state energy from Eq. (4.29). The only down side of the Bethe Ansatz is the fact that correlation functions cannot be obtained from this solution, since the information gained is related to the thermodynamics of the systems.

[3] In Eqs. (4.35)-(4.43), in the terms $iU/2$ and $iU/4$, i refers to the complex unit and not the parameters index.

4.2 Model systems

In the introduction we mentioned that the low-dimensional materials have a rather complex chemical structure making them, in general, inhomogeneous systems (or *heterostructures*), where the valence electrons propagate under the influence of different values of the on-site Coulomb interaction (due to the diverse types of atoms present), and of scattering potentials (due to impurities or defects). On the other hand, such complexity is also the source of the singular physical properties with promising applications in technology. We will model inhomogeneous systems starting from the one-dimensional Hubbard Hamiltonian in Eq. (4.1), including terms corresponding to scattering potentials,

$$H = -t \sum_{i,\sigma} c^{\dagger}_{i,\sigma} c_{i+1,\sigma} + \sum_{i} U_i n_{i\uparrow} n_{i\downarrow} + \sum_{i,\sigma} V_i n_{i\sigma} \tag{4.44}$$

where again $c^{\dagger}_{i,\sigma}$ ($c_{i,\sigma}$) is the creation (annihilation) operator with spin σ ($=\uparrow,\downarrow$) at site i and $n_{i\sigma} = c^{\dagger}_{i,\sigma} c_{i,\sigma}$ is the electron number operator. Tunable parameters are t, U, and V; and we choose t to set the energy scale. The Hamiltonian in Eq. (4.44) incorporates the different systems we want to study. The Hubbard heterostructures we investigate are chains with length L under OBC. Figure 4.1 shows the layout of the structures. We describe them in the following:

- **Heterostructure I** is a chain with on-site Coulomb interaction U/t switching between two different values, in a step-wise form (see the continuum line in Fig. 4.2). It can be visualized as a square valley in the middle point of the chain with sharp edges at the sites labeled x_L and x_R. No scattering potentials are introduced. The form of the Coulomb interaction is given by the function

$$U(x) = \begin{cases} U_L & \text{for } \ 0 < x < x_L \\ U_C & \text{for } x_L \leq x < x_R \\ U_R & \text{for } x_R \leq x < L \end{cases} \tag{4.45}$$

  where $U_L = U_R > U_C$.

- **Heterostructure II** has a form of the Coulomb interaction which changes smoothly close to x_L and x_R, contrary to the former case. The actual change is given by the function

$$U(x) = A + B\cos(\gamma x), \tag{4.46}$$

  with A, B and γ are constants (see broken line in Fig. 4.2). As in the previous case, no scattering potentials are introduced. Heterostructures I and II are designed to investigate what happens when the Coulomb potential modifies abruptly or smoothly.

- **Heterostructure III** includes, in addition to the Coulomb interaction described for heterostructure I, two potential walls of different height V, located at the positions x_L and x_R in the chain (see Fig. 4.2).

The sites x_L and x_R, as seen from Fig. 4.1 and Fig. 4.2, divide the whole system into three homogeneous subchains U_L, U_C and U_R. This raises two main questions: first, how the density-density correlation function behaves in the whole system and second, whether the known results for the homogeneous regime can be recovered within the subchains.

For inhomogeneous structures the high-energy physics is determined by the underlying chemistry which, as already mentioned, introduces in the atomic scale on-site Coulomb correlations and local potentials. On the other hand, at large length scales, the physics has to be described by the TLL model. In order to establish a connection between the low-energy

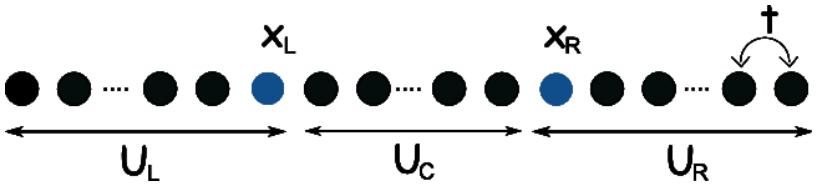

Figure 4.1: General arrangement of a Hubbard heterostructure. The inhomogeneous systems are 1D chains where the electrons hop with coupling constant t and the on-site Coulomb interaction is position-dependent. Our heterostructures are defined as junctions of three homogeneous regions, U_L, U_C, and U_R, with different values for the on-site Coulomb interaction.

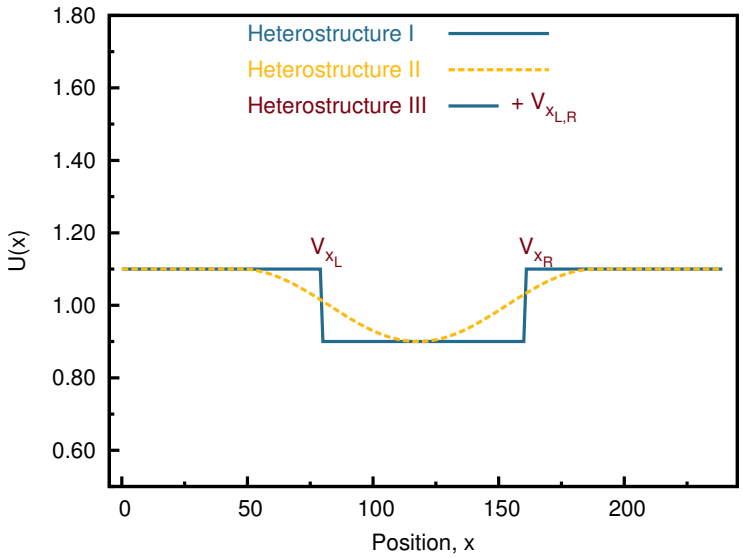

Figure 4.2: On-site Coulomb interaction as a function of the position used to define heterostructures I,II, and III.

TLL and the quasi-one-dimensional systems synthesized in the laboratory, we investigate the density-density correlation functions in the asymptotic region (i. e. for well separated positions x and x'). Position dependent on-site Coulomb interaction $U(x)$ and a local potential V are used to model the changes in the local chemistry of the heterostructures. This defines regions which, for slowly varying potentials, can be separately considered as homogeneous. We wish to study how the TL parameter changes close to the crossover regions. We expect to find a description of it in terms of $U(x)$ and the local density $n(x)$. We will investigate the above described structures using the density-matrix renormalization group method, which is he topic of the next chapter.

SUMMARY

In this chapter we introduced the one-dimensional Hubbard model and solved it using the Bethe Ansatz. For systems with periodic boundary conditions, the Bethe Ansatz solution was explained in detail, and the results were extended to systems with open boundary conditions. The Tomonaga-Luttinger liquid model and the Bethe Ansatz solution of the one-dimensional Hubbard model gives accurate information on the low-energy physics of homogeneous systems. We want now to investigate how much of these descriptions is still valid in the case of inhomogeneous systems (heterostructures), which we also introduced in this chapter. They are represented by a one-dimensional Hubbard model with position-dependent on-site Coulomb interaction $U(x)/t$. Some of these inhomogeneous systems include as well potential barriers.

Chapter 5

The Density-Matrix Renormalization Group Method

An accurate description of a many-body system must take into account the different interactions between its components. Such interactions can lead to strong correlation effects and make the problem analytically and even numerically unsolvable. Exact solutions such as the ones achieved through the Bethe Ansatz are, as we mentioned in section 4.1.2, rare. A numerical study of quantum many-body problems requires to handle an exponentially increasing basis to represent the quantum state of the system. As an example, we can think of a two-spin system with $s = 1/2$. In this case, four states $|\downarrow\downarrow\rangle, |\downarrow\uparrow\rangle, |\uparrow\downarrow\rangle$, and $|\uparrow\uparrow\rangle$ conform the basis of the Hilbert space. As is expected, the dimension of this Hilbert space increases exponentially as 2^n, with n the number of spins. Normally, only systems of up to 30 spins can be solved by exact diagonalization. In this chapter, the density matrix renormalization group method (DMRG) will be discussed and its algorithms described. This method will be introduced as a successor of the numerical renormalization group method (NRG) by Wilson [52].

5.1 The DMRG method

The DMRG developed by S. R. White has proven to be a powerful method for treating low-dimensional strongly correlated systems [49, 50]. It combines a variational method and a real space renormalization group method. The goal is to diagonalize the Hamiltonian of large one-dimensional lattice systems, by selecting a smaller sector of the complete Hilbert space with a size-manageable basis, yet accurate enough to best represent the state of the system. Such accurate representation, as we will see, will be given by the density matrix of the system. The DMRG method was originally developed to overcome the problems that arise in one-dimensional interacting systems when standard renormalization group techniques are applied [27]. The main concerns areg *a*) the selection of the sector of the Hilbert space, *b*) the construction of the wavefunction of the system, and *c*) the handling of the boundary conditions in the block construction of the systems.

In the renormalization group by Wilson the attention was directed not to the full spectrum of the eigenstates but only to the ground state or low-energy excitations. With this in mind, the truncation of the Hilbert space is done by keeping only the sector with the m lowest-energy eigenstates. This reduction of the Hilbert space would allow access to bigger systems which are constructed starting from two neighboring sites S or *blocks* and combined (i. e. they interact with each other) to form a new system SS twice the size of the original. At this point the new Hilbert space has a size of m^2 states and must be again truncated to keep its size constant. By attaching a new site in an iterative process, the system can be grown to any desired size. The construction of the wavefunction at each iteration follows from the diagonalization of the Hamiltonian H_S of the system, which is now expressed in terms of the reduced basis.

Wilson used the renormalization group method to solve the problem of the Kondo effect. This is the effect of a magnetic impurity in a metallic host. It was observed that there is a critical temperature at which a spin-1/2 impurity couples to the conduction band of the metal resulting in a finite magnetization. Wilson mapped the problem to a one-dimensional

chain with the impurity in one extreme (see Fig. 5.1). Formulated in this way, the couplings between the blocks decrease exponentially obtaining a good numerical accuracy. In the case of one-dimensional systems where the interactions between the building blocks are constant, the NRG leads to important errors due to the Hilbert space truncation. One example of this is found when studying the non-interacting one-dimensional tight-binding model [51]. In non-interacting models, an appropriate combination of boundary conditions solve the problem, but in the interacting case the solution is not trivial. In the following we will discuss how the density matrix projection gives us the necessary information to best represent a state in a reduced basis.

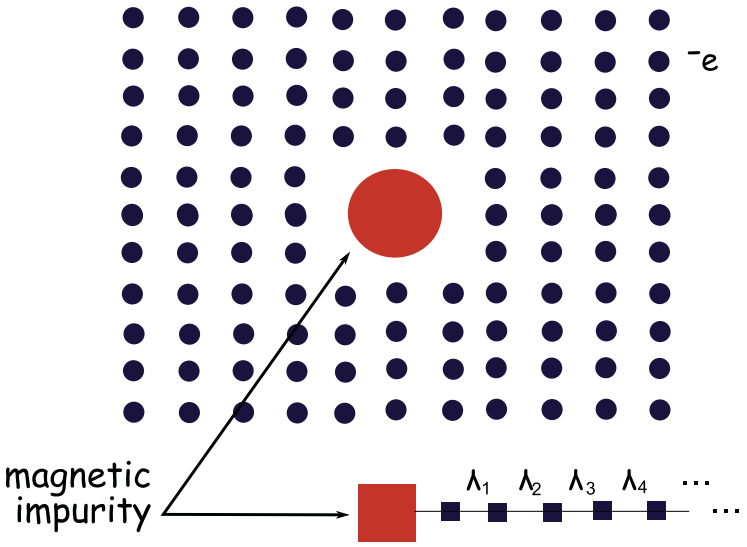

Figure 5.1: Mapping of the Kondo problem to a 1D chain. With the magnetic impurity at the head and decaying values for the couplings.

5.1.1 Density matrix projection

When dealing with quantum systems, we are specially interested in observables, which are given by the corresponding expectation value of a suitable operator A and this can be calculated as

$$\langle A \rangle = \mathrm{tr}\ (\rho A), \tag{5.1}$$

where ρ is the density matrix of the system. Thus, one can assume that the physically significant information of the system is contained in the density matrix. If the system is in a *pure* state, i.e., if it is characterized by a single-state vector $| \psi \rangle$, the density matrix is $\rho = | \psi \rangle\langle \psi |$ [1]. In the case that a system is allowed to interact with a second one, which we can call a *bath* or *environment*, a state of the system will be a mixed one as a result of the interaction. Let $| i \rangle$ be the states of the system and $| j \rangle$ the states of the environment. The elements of the density matrix of the system plus environment are then $\langle ij |\rho| i'j' \rangle$. Since we want to keep our attention focused on the system, it is necessary to extract from

[1] If the system is not in a *pure* state, it can be written as a combination of pure states $| \phi_1 \rangle$, $| \phi_2 \rangle$, ... pondered by the corresponding weights w_1, w_2, ...

ρ only the part characterizing it. Let us consider once again the matrix elements of an operator $A_{ii'}$, which acts only on the system part of the superblock and are given by

$$A_{ii'} = \langle\ ij\ |A|\ i'j'\ \rangle = \langle\ i\ |A|\ i'\ \rangle\delta_{jj'}, \tag{5.2}$$

where the states $|\ j\ \rangle$ are assumed to be orthogonal. From Eq. (5.1) and Eq. (5.2) the expectation value $\langle\ A\ \rangle$ is

$$\begin{aligned}\langle\ A\ \rangle &= \mathrm{tr}\big(\rho A\big)\\ &= \sum_{ii'jj'} \langle\ ij\ |\rho|\ i'j'\ \rangle\langle\ i'j'\ |A|\ ij\ \rangle\\ &= \sum_{ii'} \Big[\sum_{j'} \langle\ ij'\ |\rho|\ i'j'\ \rangle\Big]\langle\ i'\ |A|\ i\ \rangle.\end{aligned} \tag{5.3}$$

We can define the elements of a matrix ρ_E by

$$\langle\ i\ |\rho_E|\ i'\ \rangle = \sum_{j'} \langle\ ij'\ |\rho|\ i'j'\ \rangle. \tag{5.4}$$

Then Eq.(5.3) can be written as

$$\begin{aligned}\langle\ A\ \rangle &= \sum_{ii'} \langle\ i\ |\rho_E|\ i'\ \rangle\langle\ i'\ |A|\ i\ \rangle\\ &= \mathrm{tr}\ \rho_E A.\end{aligned} \tag{5.5}$$

Since the information on the system can be expressed in terms of the expectation value of an operator acting on it, it follows from Eq. (5.5) that such information of the system can be obtained once ρ_E is known. Because the density matrix elements in the unobserved variable j are traced out, $\rho_E(i)$ is usually called the *reduced density matrix*. This can also be expressed as taking the total density matrix ρ and then project it onto the subspace of interest. For convenience we will introduced the shorthand notation

$$\rho_E = \mathrm{tr}_E\ \rho \tag{5.6}$$

where $\mathrm{tr}_\mathrm{E}\ \rho$ indicates the trace over all unobserved variables.

The reduced density matrix has n eigenvalues ω_α and orthonormal eigenstates $|\ \omega_\alpha\ \rangle$

$$\rho_E|\ \omega_\alpha\ \rangle = \omega_\alpha|\ \omega_\alpha\ \rangle \tag{5.7}$$

with

$$\sum_\alpha \omega_\alpha = 1. \tag{5.8}$$

Generally, it is assumed that the states are ordered such that $\omega_1 \geq \omega_2 \geq \omega_3 \geq \ldots$. So, when keeping only m states of the reduced density matrix to describe the system, the error due to the truncation is

$$\mathrm{Err} = 1 - \sum_{\alpha=1}^{m} \omega_\alpha. \tag{5.9}$$

In the following we will show, using a variational approach, how to obtain the optimal quantum states of a system from the reduced density matrix [2].

Let us consider the already described arrangement, also called *superblock*, consisting of two parts or *blocks*, S and E (see Fig. 5.2). The ground state wavefunction $|\ \Psi\ \rangle$

[2] In his original paper, White wrote the problem in the form of a singular-value decomposition [49].

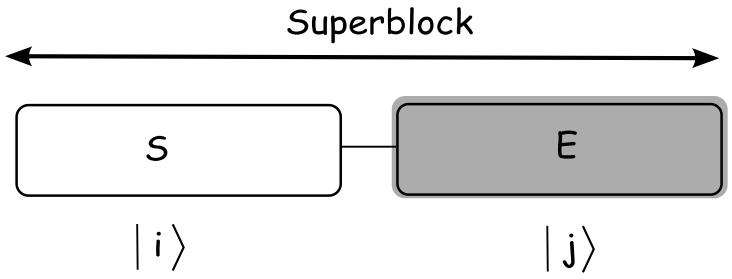

Figure 5.2: A superblock consist initially of a left block or system S and a right block or environment E, with ground state wavefunction $\mid \Psi \rangle = \sum_{i,j} \Psi_{ij} \mid i \rangle \otimes \mid j \rangle$.

$$\mid \Psi \rangle = \sum_{i,j} \Psi_{ij} \mid i \rangle \otimes \mid j \rangle \tag{5.10}$$

is written in terms of the states $\mid i \rangle$ and $\mid j \rangle$ on the blocks S and E respectively. If the system is truncated and the Hilbert space is spanned by only m ($m < n$) orthonormal states $|\alpha\rangle = \sum_i u_{\alpha i} \mid i \rangle$ with real coefficients. Then the wavefunction of the system can be approximated by [3]

$$\mid \tilde{\Psi} \rangle = \sum_{\alpha=1}^{m} \sum_{j=1}^{n} a_{\alpha j} \mid \alpha \rangle \otimes \mid j \rangle, \tag{5.11}$$

and the problem turns to minimize the distance

$$||| \Psi \rangle - \mid \tilde{\Psi} \rangle||^2 = 1 - 2 \sum_{\alpha i j} \psi_{ij} a_{\alpha j} u_{\alpha i} + \sum_{\alpha j} a_{\alpha j}^2 \tag{5.12}$$

with respect to $a_{\alpha j}$ and $u_{\alpha i}$. The stationary solution in $a_{\alpha j}$ [4] leads to

$$\sum_i \psi_{ij} u_{\alpha i} = a_{\alpha j}. \tag{5.13}$$

Combining Eq. (5.13) and Eq. (5.12), and using the reduced density matrix of the system we find that

$$1 - \sum_{\alpha i i'} u_{\alpha i} \rho_{i i'} u_{\alpha i'}. \tag{5.14}$$

The coefficients $u_{\alpha i'}$ transform the basis from $\mid i \rangle$ to $\mid \alpha \rangle$, and Eq. (5.14) can be expressed in terms of the density matrix eigenvalues ω_α:

$$1 - \sum_{\alpha i i'} u_{\alpha i} \rho_{i i'} u_{\alpha i'} = 1 - \sum_{\alpha=1}^{m} \omega_\alpha. \tag{5.15}$$

[3] Here we assume that the system and environment have the same configuration and therefore m states are kept on both. However, this must not necessarily apply.

[4] Obtained by taking the derivative in $a_{\alpha j}$ of Eq. (5.12) and setting it to zero.

In this way the minimum can be found by choosing $| \alpha \rangle$ to be the m eigenvectors $| \omega_\alpha \rangle$ corresponding to the largest eigenvalues ω_α of the density matrix.

In this section we discussed the motivation for using numerical approaches in solving many-body, strongly correlated systems. We showed that the density matrix projection offers a controlled process to reduce the degrees of freedom by decimating the Hilbert space but still permitting to accurately describe the ground state of a system connected to an environment. In the next subsections we will describe the DMRG algorithms based on the density matrix projection and how the calculation of equilibrium properties is done.

5.1.2 Infinite-size algorithm

The basic DMRG algorithm incorporates the density matrix projection described in the last section into the renormalization group scheme by Wilson. We begin with a small system and let it grow iteratively by adding new sites between the system and the environment (see Fig. 5.3). The new block must be transformed according to the density matrix projection. This first process is know as the *infinite-size algorithm*, for it allows to grow the system to any desired size. The algorithm consists of the next steps:

1. Take a system block S with L sites and m states. It should be small enough to be exactly diagonalizable and obtain the ground state $| \Psi \rangle$.

2. Add a single site with n states to S to get a new system block S' with $m \times n$ states.

3. Construct the superblock by joining the system block S' and the environment E. E may consist of a block with a few sites or a reflection of the block system S'.

4. Calculate the ground state of the superblock. For this one can choose between the Lanczos or the Davison algorithms [29]. The ground state of the superblock, as explained in the last section, is

$$| \Psi \rangle = \sum_{i}^{m \times n} \sum_{j}^{n} \Psi_{ij} | i \rangle \otimes | j \rangle \tag{5.16}$$

   For the beginning, we are interested in the ground state. We express this by saying that the ground state is the *target state*. For some applications other states out of the ground state will serve as target states. In general, the target states are those from which the reduced density matrix is calculated.

5. Calculate the reduced density matrix ρ_E

$$(\rho_E)_{ii'} = \sum_{j} \Psi_{ij} \Psi_{i'j} \tag{5.17}$$

   Diagonalize the density matrix to obtain the set of eigenvectors and corresponding eigenvalues, $| \omega_\alpha \rangle$ and ω_α, respectively. In this step the important states to represent the system are selected.

6. Keep the m eigenvectors of the reduced density matrix with the largest eigenvalues. They are the new basis of the system block. Transform the operators A in the system like

$$\tilde{A} = U^T A U \tag{5.18}$$

   where U is the transformation matrix formed by the m column eigenvectors of the density matrix with the largest eigenvalues.

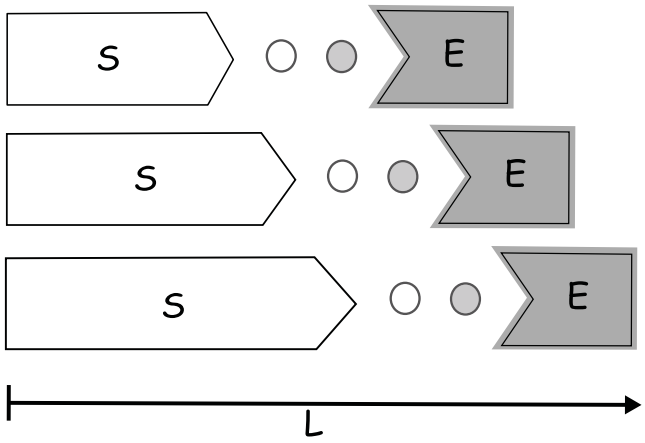

Figure 5.3: DMRG infinite-size algorithm. The system (S) is grown up to a desired length L. The system connects to an environment (E) through single sites. In this diagram the environment is chosen to have a fixed length of a few sites.

7. Go back to step 2 and repeat the process until the desired size of the system is reached.

The process of joining two blocks, as done in steps 2 and 3, amounts to building the operators of the new system or superblock, like for example the Hamiltonian. An operator on the system (environment) with elements $A^S_{i,i'}$ ($A^E_{j,j'}$) acts only on the states of the corresponding block, this means that the same operator on the superblock is written as

$$A_{ij,i'j'} = A^S_{i,i'}\delta_{j,j'} + A^E_{j,j'}\delta_{i,i'}. \tag{5.19}$$

In the case of the Hamiltonian operator, extra terms emerge from the interaction between the blocks. From Fig. 5.4 we see that, in the case of nearest neighbor interactions, the total Hamiltonian at a step is

$$H = H_S + H_a + H_b + H_{S-a} + H_{a-b} + H_{b-E} + H_E. \tag{5.20}$$

Such operator is not explicitly constructed, one makes use of the system symmetries. Examples of these symmetries are

$$[H,\ \vec{S}^2] = [H,\ S^z] = [H,\ N] = 0 \tag{5.21}$$

where $\vec{S} = \sum_i \vec{S}_i$ and $N = \sum_i n_i$. The symmetries present in the system depend on the model one is working with. Nevertheless, once a symmetry found ($[H, A] = 0$), the Hamiltonian will not mix states from different eigenspaces of A. And this will let us work with blocks.

5.1.3 Finite-size algorithm

The infinite-size algorithm is not suitable to describe a system of fixed length L. Systematic errors can propagate as the size of the system increases. We can see from the algorithm that at each step, with a system of length L_S, whose basis has been truncated, the ground state of the new system L_{S+1} is approximated using that of the previous smaller system. In this way, the density matrix and the corresponding truncation are never constructed

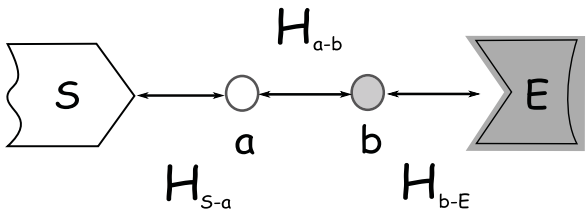

Figure 5.4: Connecting the system (S) and the environment (E) through two single sites a and b.

in terms of the correct target state. The finite-size algorithm was designed to solve this problem. At each step, the size of both L_S and L_E will be chosen so that the size of the superblock remains constant, i. e., $L_S + L_E = L$ (see Fig. 5.5). The finite-size algorithm consists of the following steps:

1. Use the infinite-size algorithm to build up the superblock to the desired length L. After every truncation, store all operators, including the Hamiltonians, as they will be reused in the coming iterations. After the last step, the system has a length L_S and the environment L_E, with $L_S + L_E = L$. We will now rename the components of the superblock. The system block is now the *left block* of size l, and the environment block is the *right block* of size r.

2. Add a single site to the right block, so that $r' = r + 1$. Add a single site to the left block of size $l = L - r' - 1$. Build a superblock out of these two new blocks.

3. Carry out steps 4-6 of the infinite-size algorithm, i. e. diagonalize the superblock, calculate the reduced density matrix with respect to the left block, and transform the operators with the new basis.

4. Rename $r = r'$. Go back to step 2 until $l = 2$. We see how the right block increases its size and at the same time, the left block shrinks. This is called the *right to left sweep*.

5. Add a single site to the left block, so that $l' = l + 1$. Add a single site to the right block of size $r = L - l' - 1$. Build a superblock from these two blocks.

6. Carry out the steps 4-6 of the infinite-size algorithm.

7. Rename $l = l'$. Go back to the step 5 until $L - l' = 2$. This is called the *left to right sweep*.

8. Go back to point 2 and repeat steps 2-7 until the system converges.

The *sweeping* back and forth over the system has the advantage that the target state is always determined for the same system. The environment blocks used in the first sweep[5]

[5]This means, the system blocks stored from the infinite-size algorithm.

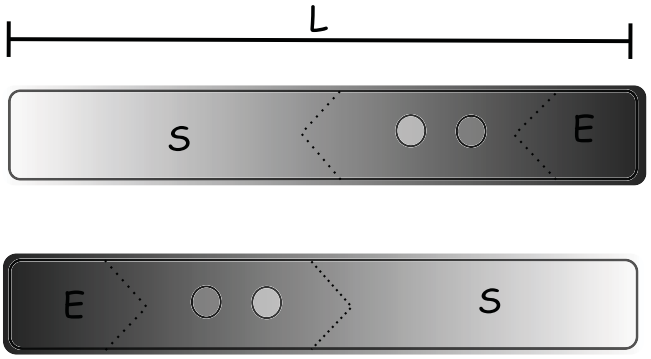

Figure 5.5: DMRG finite-size algorithm. In order to keep the total length of the system fixed, the system block shrinks in the direction of growing in the right-to-left sweep. The process reverses in the left-to-right sweep.

were calculated for smaller systems, so they are not optimal to represent the environment. But for the second sweep, the new environment blocks were calculated for the system with the right size, so they are better than those used in the former sweep. This leads to a progressive improvement in the measurement of the target states of the superblock.

5.1.4 Calculation of equilibrium properties

The ground state energy of the superblock is determined every time the superblock is diagonalized. Since the DMRG is a variational approach $E^0_{DMRG} \geq E^0_{exact}$. The measurement of observables renders better results if carried out at the position where E_0 has a minimum. In the case of homogeneous systems the minimum is usually in the middle of the chain. For impurity systems like the single-impurity Anderson model, the minimum is close to the position of the impurity.

Expectation values of local operators are the first observables that can be measured. This is, as explained above, usually done after the superblock reached a symmetric configuration, i.e., when both system and environment have the same size. The expectation value of an operator A is

$$\langle\ A\ \rangle = \langle\ \Psi\ |\ A\ |\ \Psi\ \rangle \tag{5.22}$$

with $|\ \Psi\ \rangle$ the eigenstate of the superblock and the operator A has been always tracked, i. e., it has been properly transformed and stored at every step. For an operator A acting on the left block, the expectation value can be written like

$$\langle\ \Psi\ |\ A\ |\ \Psi\ \rangle = \sum_{ii',j} \Psi^*_{ij}\ A_{ii'} \Psi_{i'j}. \tag{5.23}$$

For products of operators on two different sites, A and B, as in the case of correlation functions, two different situations have to be considered: *a*) the operators act on the same block or *b*) they act on different blocks. In the case of both operators acting on the same block, for example on the left block, one could naively try to calculate first the matrix

elements of the operators product like

$$(AB)_{i,j} = \sum_k A_{i,k}\ B_{k,j}. \tag{5.24}$$

This is wrong because the index k should run over all the states of the left block, but the basis of this block has been truncated thus misleading the measurement of the expectation values. This problem is solved by constructing from the beginning of the process, the operator $C = AB$. One must keep track of it during the whole process. In this way its expectation value can be calculated just as that of a single site operator.

In the second case, both operators are fully represented by the corresponding block basis, so the correlation function is given by

$$\langle\ \Psi\ |\ AB\ |\ \Psi\ \rangle = \sum_{ii',jj'} \Psi^*_{ij} A_{ii'} B_{jj'} \Psi_{i'j'} \tag{5.25}$$

5.1.5 Multiple target states

Low-lying excited states can be represented approximately through the use of multiple target states $|\ \Psi_\alpha\ \rangle$. For each one of them, the reduced density matrix must be calculated separately and added up to obtain the total reduced density matrix,

$$\rho = \sum_\alpha \omega_\alpha \rho_\alpha \tag{5.26}$$

where $\rho_\alpha = |\ \Psi_\alpha\ \rangle\langle\ \Psi_\alpha\ |$, which are pondered by the weights ω_α. There are no rules for choosing the weight associated to each state. Usually one gives the ground state $|\ \Psi_0\ \rangle$ half of the weight and the rest of it is equally divided between the other target states.

5.2 Dynamic properties at zero temperature

In the last section we have discussed how the DMRG is an effective numerical method to study ground state properties and low-lying excited states of one-dimensional systems with great accuracy. Dynamic properties, on the other hand, are beyond investigation if using the DMRG method alone. One reason for this it that the time evolution of a general excited state requires an exploration of large sectors of the Hilbert space. Important achievements in the measurement of dynamic properties have been realized by implementing techniques, like those of Green's functions, into the known DMRG algorithms. The Green's function method has become a valuable tool, for it provides a systematic approach for extracting physical information out of the system. This is done by calculating dynamic correlation functions, from which spectral density functions can be obtained, having an opportunity to relate analytical or numerical results to those obtained in the laboratory.

In the coming sections we will recall the Lehmann representation of Green's functions to calculate spectral densities and will discuss the use of this with the Lanczos vector method [15] and the correction method [42] for calculating dynamic properties.

5.2.1 Spectral densities

Let us begin by writing the causal single-particle Green's function at $T = 0$, defined as the expectation value of the time-ordered[6] commutator of field operators $\Psi(x,t)$,

$$\begin{aligned} iG_{\alpha\beta}(xt,x't') &= \langle\ \psi_0 \mid T\big[\Psi_{\alpha H}(x,t),\Psi^\dagger_{\beta H}(x',t')\big] \mid \psi_0\ \rangle \\ &= \theta(t-t')\langle\ \psi_0 \mid \Psi_{\alpha H}(x,t)\Psi^\dagger_{\beta H}(x',t') \mid \psi_0\ \rangle \pm \\ &\quad \theta(t'-t)\langle\ \psi_0 \mid \Psi_{\beta H}(x',t')\Psi^\dagger_{\alpha H}(x,t) \mid \psi_0\ \rangle \end{aligned} \tag{5.27}$$

with ψ_0 the ground state of the system, and

$$\Psi_{\alpha H}(t) = e^{iHt}\Psi_\alpha e^{-iHt} \tag{5.28}$$

is the field operator in the Heisenberg representation. In the absence of external magnetic field and ferromagnetism, the indices α and β, labeling the spin degrees of freedom, can be neglected. Also in the absence of external fields, and in homogeneous systems, the Green's function depends only on the time difference $\tilde{t} = t - t'$ instead of t and t', so $G(t,t') = G(t-t')$. For fermionic systems one has to take care of the minus sign resulting from the time-ordering. Inserting Eq. (5.28) into Eq. (5.27) and evaluating the time-order operator, the Green's function becomes

$$\begin{aligned} iG(xt,x't') = \theta(\tilde{t})\langle\ \psi_0\ |e^{iHt}\ \Psi(x,t)e^{-iHt}e^{iHt'}\Psi^\dagger(x',t')e^{-iHt}\ \mid \psi_0\ \rangle - \\ \theta(-\tilde{t})\langle\ \psi_0\ |e^{iHt'}\ \Psi^\dagger(x',t')e^{-iHt'}e^{iHt}\Psi(x,t)e^{-iHt}\ \mid \psi_0\ \rangle \end{aligned} \tag{5.29}$$

$$\begin{aligned} iG(x,x',\tilde{t}) = \theta(\tilde{t})e^{iE_0\tilde{t}}\langle\ \psi_0 \mid \Psi(x)e^{-iH\tilde{t}}\Psi^\dagger(x')\mid \psi_0\ \rangle - \\ \theta(-\tilde{t})e^{-iE_0\tilde{t}}\langle\ \psi_0 \mid \Psi^\dagger(x')e^{iH\tilde{t}}\Psi(x)\mid \psi_0\ \rangle. \end{aligned} \tag{5.30}$$

By Fourier transforming the Green's function to the frequency space

$$iG(\omega) = i\int_{-\infty}^{\infty} \mathrm{d}t\ e^{i\omega t}G(t) \tag{5.31}$$

we obtain

$$\begin{aligned} iG(x,x',\omega) = \int_{-\infty}^{\infty}\mathrm{d}\tilde{t}e^{i\omega\tilde{t}}\Big[\theta(\tilde{t})e^{iE_0\tilde{t}}\langle\ \psi_0 \mid \Psi(x)e^{-iH\tilde{t}}\Psi^\dagger(x')\mid \psi_0\ \rangle - \\ \theta(-\tilde{t})e^{-iE_0\tilde{t}}\langle\ \psi_0 \mid \Psi^\dagger(x')e^{iH\tilde{t}}\Psi(x)\mid \psi_0\ \rangle\Big], \end{aligned} \tag{5.32}$$

and finally

$$\begin{aligned} iG(x,x',\omega) = \int_{-\infty}^{\infty}\mathrm{d}\tilde{t}\Big[\langle\ \psi_0 \mid \Psi(x)\Big(\theta(\tilde{t})e^{iE_0\tilde{t}}e^{-iH\tilde{t}}e^{i\omega\tilde{t}}\Big)\Psi^\dagger(x')\mid \psi_0\ \rangle - \\ \langle\ \psi_0 \mid \Psi^\dagger(x')\Big(\theta(-\tilde{t})e^{-iE_0\tilde{t}}e^{iH\tilde{t}}e^{i\omega\tilde{t}}\Big)\Psi(x)\mid \psi_0\ \rangle\Big]. \end{aligned} \tag{5.33}$$

Using the integral representation of the θ function and its inverse

$$\pm e^{i\epsilon t}\theta(\pm t) = \frac{1}{2\pi}\int_{-\infty}^{\infty}\mathrm{d}\omega\frac{ie^{i\omega t}}{w-\epsilon\pm i\eta} \tag{5.34}$$

$$\int_{-\infty}^{\infty}\mathrm{d}te^{i\omega t}e^{-i\epsilon t}\theta(\pm t) = \pm\frac{i}{w-\epsilon\pm i\eta} \tag{5.35}$$

[6]The time-order operator places operators with the larger time argument to the left of those with he smaller time argument. Therefore it can be expressed in terms of a time step function θ.

the Green's function can now be written as

$$G(x,x',\omega) = \langle\psi_0 \mid \Psi(x)\frac{1}{\omega-(H-E_0)+i\eta}\Psi^\dagger(x') \mid \psi_0\rangle + \langle\psi_0 \mid \Psi^\dagger(x')\frac{1}{\omega+(H-E_0)-i\eta}\Psi(x) \mid \psi_0\rangle. \tag{5.36}$$

where η is a positive number. We shall come back to this parameter by the end of this section. Introducing a complete set of basis states $|\psi_n\rangle$, i.e., $\sum_n |\psi_n\rangle\langle\psi_n| = 1$, the Green's function becomes

$$G(x,x',\omega) = \sum_n \langle\psi_0 \mid \Psi(x) \mid \psi_n\rangle\frac{1}{\omega-(H-E_0)+i\eta}\langle \psi_n\mid \Psi^\dagger(x') \mid \psi_0\rangle + \langle\psi_0 \mid \Psi^\dagger(x') \mid \psi_n\rangle\frac{1}{\omega+(H-E_0)-i\eta}\langle \psi_n\mid \Psi(x) \mid \psi_0\rangle \tag{5.37}$$

and for the on-site Green Function, i.e., for $x = x'$,

$$G(x,\omega) = \sum_n |\langle\psi_0 \mid\Psi(x)\mid \psi_n\rangle|^2\left(\frac{1}{\omega-(E_n-E_0)+i\eta} + \frac{1}{\omega+(E_n-E_0)-i\eta}\right). \tag{5.38}$$

To calculate spectral densities from the Green's function method we take the correlation function defined by

$$C_A(x,t-t') = \langle\psi_0 \mid A^\dagger(x,t)A(x,t') \mid\psi_0\rangle \tag{5.39}$$

where $A(x,t)$ is the Heisenberg representation of an operator A and $|\psi_0\rangle$ is the ground state of the system,

$$A(x,t) = e^{iHt}A(x)e^{-iHt}. \tag{5.40}$$

Inserting this into Eq. (5.39) one obtains

$$C_A(x,t-t') = \langle\psi_0 \mid e^{iHt'}A^\dagger(x)e^{-iHt'}e^{iHt}A(x)e^{-iHt}\mid\psi_0\rangle \tag{5.41}$$

Proceeding as before, we Fourier transform Eq. (5.41) to the energy space and introduce a complete set of states $|\alpha\rangle$, after which the correlation function becomes [7]

$$\begin{aligned} C_A(x,\omega) &= \int \mathrm{d}\tilde{t}e^{i\omega\tilde{t}}\sum_\alpha e^{i(E_\alpha-E_0)\tilde{t}}\ |\langle\alpha|A(x)|\psi_0\rangle|^2 \\ &= \sum_\alpha |\langle\alpha|A(x)|\psi_0\rangle|^2\ \delta(w-(E_\alpha-E_0)) \end{aligned} \tag{5.42}$$

Let us now go back to the Green's function of Eq. (5.38) and consider the imaginary part of it,

$$\mathrm{Im}\big[G(x,\omega)\big] = \mathrm{Im}\Big[\sum_n |\langle\psi_0 \mid\Psi(x)\mid \psi_n\rangle|^2\left(\frac{1}{\omega-(E_n-E_0)+i\eta} + \frac{1}{\omega+(E_n-E_0)-i\eta}\right)\Big]. \tag{5.43}$$

[7] This is called the Lehmann representation of the spectral density. An excellent book on the Green's function methods is the one by Abrikosov, Gorkov and Dzyaloshinski [2]

Using the relation

$$\frac{1}{x+i\eta} = \mathrm{P}\left[\frac{1}{x}\right] - i\pi\delta(x) \tag{5.44}$$

where P denotes the *principal part*. By substitution of $x + i\eta$ through $\omega \mp (E_n - E_0) \pm i\eta$, one obtains

$$\mathrm{Im}\big[G(x,\omega)\big] = \mathrm{Im}\sum_n |\langle\psi_0\ |\Psi(x)|\ \psi_n\rangle|^2 \Bigg\{ \mathrm{P}\left[\frac{1}{\omega-(E_n-E_0)+i\eta}\right] - i\pi\delta(\omega-(E_n-E_0)) + \mathrm{P}\left[\frac{1}{\omega+(E_n-E_0)-i\eta}\right] + i\pi\delta(\omega+(E_n-E_0))\Bigg\} \tag{5.45}$$

which simplifies to

$$\mathrm{Im}\big[G(x,\omega)\big] = \mp i\pi \sum_n |\langle\psi_0\ |\Psi(x)|\ \psi_n\rangle|^2\ \big(\delta(\omega-(E_n-E_0)) + \delta(\omega+(E_n-E_0))\big). \tag{5.46}$$

After comparing Eq. (5.42) and Eq. (5.46) we can conclude that

$$C(x,\omega) = -\frac{1}{\pi}\ \mathrm{Im}G(x,\omega), \tag{5.47}$$

where G is the Green's function of the operator A. Since we are interested in lattice models, let us consider a finite lattice with n sites and N particles, with Hamiltonian H. The corresponding Green's function is given by

$$\begin{aligned} G(i,j,\omega) = \langle\psi_0|c_i\frac{1}{\omega-(H-E_0)+i\eta}c_j^\dagger|\psi_0\rangle\ + \\ \langle\psi_0|c_j^\dagger\frac{1}{\omega+(H-E_0)-i\eta}c_i|\psi_0\rangle, \end{aligned} \tag{5.48}$$

$|\psi_0\rangle$ is the ground state of the system, and $c_i^\dagger$ and c_i are the creation and annihilation operators, respectively, of a particle at site i. Excitations of the system are created, for example, by adding or removing a particle. Such processes result in the following set of Schödinger equations,

$$\begin{aligned} H|\alpha\rangle &= E_\alpha|\alpha\rangle \\ H|\beta\rangle &= E_\beta|\alpha\rangle, \end{aligned} \tag{5.49}$$

where $|\alpha\rangle$ are the eigenstates of the Hamiltonian H with $N+1$ particles and $|\beta\rangle$ are the eigenstates of the Hamiltonian with $N-1$ particles.

We define $c_i^\dagger|\psi_0\rangle = |i^+\rangle$ and $c_i|\psi_0\rangle = |i^-\rangle$. Using these definitions and introducing the

$|\alpha\rangle$ and $|\beta\rangle$ sets of eigenstates in Eq. (5.48), we obtain

$$G(i,j,\omega) = \sum_{\alpha,\alpha'} \langle i^+|\alpha\rangle\langle\alpha| \frac{1}{\omega - (H - E_0) + i\eta} |\alpha'\rangle\langle\alpha'|j^+\rangle + \sum_{\beta,\beta'} \langle j^-|\beta\rangle\langle\beta| \frac{1}{\omega + (H - E_0) - i\eta} |\beta'\rangle\langle\beta'|i^-\rangle \tag{5.50}$$

$$= \sum_{\alpha,\alpha'} \langle i^+|\alpha\rangle \frac{\delta_{\alpha,\alpha'}}{\omega - (E_\alpha - E_0) + i\eta} \langle\alpha'|j^+\rangle + \sum_{\beta,\beta'} \langle j^-|\beta\rangle \frac{\delta_{\beta\beta'}}{\omega + (E_\beta - E_0) - i\eta} \langle\beta'|i^-\rangle \tag{5.51}$$

$$= \sum_{\alpha} \frac{\langle i^+|\alpha\rangle\ \langle\alpha|j^+\rangle}{\omega - (E_\alpha - E_0) + i\eta} + \sum_{\beta} \frac{\langle j^-|\beta\rangle\ \langle\beta|i^-\rangle}{\omega + (E_\beta - E_0) - i\eta}. \tag{5.52}$$

Finally, the on-site lattice Green's function is given by

$$G(i,\omega) = \sum_{\alpha} \frac{\langle|i^+|\alpha\rangle|^2}{\omega - (E_\alpha - E_0) + i\eta} + \sum_{\beta} \frac{\langle|j^-|\beta\rangle|^2}{\omega + (E_\beta - E_0) - i\eta}. \tag{5.53}$$

Summarizing, the spectral density can be systematically calculated following the next steps [16]:

- Take a lattice with N particles and calculate the ground state $|\psi_0\rangle$.
- Calculate $|i\rangle = c_i^\dagger|\psi_0\rangle$.
- Diagonalize the $(N+1)$-particle Hamiltonian to obtain the set of $|\alpha\rangle$ eigenstates and corresponding eigenvalues E_α.
- calculate the weights $w(\alpha) = |\langle i|\alpha\rangle|^2$.
- To visualize the peaks one can use either a Gaussian or a Lorentzian function. If using a Gaussian function, the right-hand side of the spectrum is given by

$$A_r(\omega) = \sum_{\alpha} w(\alpha) \frac{1}{\sqrt{2\pi\sigma^2}}\ \exp\Big(-\frac{(\omega - (E_\alpha - E_0^N))^2}{2\sigma^2}\Big). \tag{5.54}$$

To obtain the left part of the spectrum, one applies the annihilation operator, so that $|i\rangle = c_i|\psi_0\rangle$ and the $(N-1)$-particle Hamiltonian is to be diagonalized to obtain the $|\beta\rangle$ set of eigenstates. The weights $w(\beta)$ are calculated the same way as before. The left-hand side of the spectral density is the given by

$$A_l(\omega) = \sum_{\beta} w(\beta) \frac{1}{\sqrt{2\pi\sigma^2}}\ \exp\Big(-\frac{(\omega - (E_\beta - E_0^N))^2}{2\sigma^2}\Big), \tag{5.55}$$

where σ is an arbitrary broadening factor. Experimentally, inverse photoemission (IPE) is used to study the spectral density associated with the addition of an electron to the system,

whereas in the case of the subtraction of an electron, photoemission (PE) experiments are used.

In this section we presented the Green's function method for a lattice fermionic system. Calculation of the spectral densities offers a way to establish connection between the theory and the experiment. In the next sections we will discuss two different methods to perform dynamic calculations.

5.2.2 Lanczos vector method

As we have seen in the last section, a quasiparticle state of the system can be represented by its spectral density of states (in momentum space) $A_q(\omega)$ and the peak position of $A_q(\omega)$ can be identified with the dispersion energy $\epsilon(q)$. When discussing symmetries and good quantum numbers for the DMRG method in section (5.1.2) we did not include momentum, because the method is applied in real space and momentum is not a good quantum number. Besides, information of the excited states is lost in the truncation of the Hilbert space. In the work by Hallberg [15], the dynamic correlation functions are actually computed. We can summarize the method in two steps: first, the use of the Lanczos algorithm to find the tridiagonal form of the Hamiltonian H, which is a symmetric matrix; and second, the inversion of the tridiagonal matrix to finally obtain the spectrum from the continued fraction expansion given by

$$G(z) = \cfrac{\langle\ \Psi_0\ |A^\dagger A|\Psi_0\ \rangle}{z - a_0 - \cfrac{b_1^2}{z - a_1 - \cfrac{b_2^2}{z - \ldots}}}, \tag{5.56}$$

where the coefficients a_n and b_n are obtained from the Lanczos recursion relation

$$|f_{n+1}\rangle = H|f_n\rangle - a_n|f_n\rangle - b_n^2|f_{n-1}\rangle, \tag{5.57}$$

here the starting vector $|f_0\rangle$ is an arbitrary vector. We will see below that the correct choice of $|f_0\rangle$ has great advantages. The tri-diagonalization occurs after projection of H onto a space spanned by the product of powers of H and the Lanczos vectors $v = |f_n\rangle$. Such space is called the Krylov space,

$$\mathcal{K}_m(H, v) = \text{span}\{v, Hv, H^2v,\ \ldots\ , H^{m-1}v\}. \tag{5.58}$$

The resulting tridiagonal Hamiltonian is

$$H = \begin{pmatrix} a_0 & b_0 & & & & 0 \\ b_0 & a_1 & b_1 & & & 0 \\ & b_1 & a_2 & b_2 & & 0 \\ & & \ddots & \ddots & \ddots & \\ & & & b_{m-2} & a_{m-1} & b_{m-1} \\ 0 & & & & b_{m-1} & a_m \end{pmatrix} \tag{5.59}$$

Once in its tridiagonal form, the eigenvalues and eigenvectors of the Hamiltonian can be obtained easily, i. e. the ground state $|\psi_0\rangle$ can be obtained with this method. Let us now apply this to calculate spectral densities. We start by setting the first Lanczos vector to,

$$|f_0\rangle = \frac{A_q|\psi_0\rangle}{\langle\psi_0|A_q^\dagger A_q|\psi_0\rangle}, \tag{5.60}$$

where A_q is an operator in momentum space and $|\psi_0\rangle$ is the ground state of the system. We now run once again the Lanczos algorithm, which is summarized in the following:

$$\begin{aligned} |f_0\rangle &= A_q|\psi_0\rangle/\langle\psi_0|A_q^\dagger A_q|\psi_0\rangle \\ a_n &= \langle f_n|H|f_n\rangle \\ b_n^2 &= \| \, |f_n\rangle \, \|_2 \\ |f_{n+1}\rangle &= H|f_n\rangle - a_n|f_n\rangle - b_n^2|f_{n-1}\rangle \end{aligned}$$

The tridiagonal form of H can be diagonalized and the result is a set of eigenvectors $|\varphi_m\rangle$. This is a nearly complete set, i.e., $1 \approx \sum_m |\varphi_m\rangle\langle\varphi_m|$, and can be used to be included in the Green's function

$$\begin{aligned} G(x,x',\omega) &\approx \sum_{n,m} \langle\psi_0|A_q^\dagger|\varphi_n\rangle\langle\varphi_n| \frac{1}{\omega-(H-E_0)+i\eta} |\varphi_m\rangle\langle\varphi_m|A_q|\psi_0\rangle \\ &= \sum_n \langle\varphi_n| \frac{1}{\omega-(H-E_0)+i\eta} |\varphi_n\rangle |\langle\varphi_n|A_q| \, \psi_0\rangle|^2 \\ &= \sum_n \frac{(\varphi_n^0)^2\langle\psi_0|A_q^\dagger A_q|\psi_0\rangle}{\omega-(E_n-E_0)+i\eta}, \end{aligned} \tag{5.61}$$

where E_n is the eigenvalue of $|\varphi_n\rangle$ and $\varphi_n^0 = \langle f_0|\varphi_n\rangle$. The dynamic correlation function can be calculated from

$$\begin{aligned} C(q,\omega) &= -\frac{1}{\pi} \lim_{\eta\to 0^+} \mathrm{Im}G(q,\omega+E_0+i\eta) \\ &= \frac{\langle\psi_0|A_q^\dagger A_q|\psi_0\rangle}{\pi} \lim_{\eta\to 0^+} \sum_n \frac{\eta(\varphi_n^0)^2}{(\omega-(E_n-E_0))^2+\eta^2} \\ &= \langle\psi_0|A_q^\dagger A_q|\psi_0\rangle \sum_n \delta(\omega-(E_n-E_0))(\varphi_n^0)^2, \end{aligned} \tag{5.62}$$

where E_0 is the ground state energy and the peaks appear at $\omega_n = E_n - E_0$. A crucial point about the Lanczos method lies in the orthogonality of the Lanczos vectors, which must be ensured at each step. Furthermore, the calculation of spectral densities is also approximated, given the fact that the set of Lanczos vectors is almost complete. The actual calculation of the spectrum is carried out within the DMRG algorithm as follows: let us first recall that the on-site lattice Green's function is given by

$$\begin{aligned} G(i,\omega) = &\sum_\alpha \frac{\langle|i^+|\alpha\rangle|^2}{\omega-(E_\alpha-E_0)+i\eta} + \\ &\sum_\beta \frac{\langle|j^-|\beta\rangle|^2}{\omega+(E_\beta-E_0)-i\eta}. \end{aligned} \tag{5.63}$$

Then the right part of the spectrum can be obtained following the next steps:

- Select the appropriate target states:

$\|\psi_0\rangle$	the ground state
$c_i^\dagger\|\psi_0\rangle = \|f_0\rangle$	the first Lanczos vector
$\|f_i\rangle$	the next few Lanczos vectors

- Build up the system to the desired size using the infinite-size DMRG algorithm.
- Carry out the finite-size DMRG algorithm until reaching convergence of the ground state energy.
- Sweep back to the position where the truncation errors reach their minimum on both blocks[8], and calculate the spectral density in the way as was described in the last section.

To complete the spectrum, the left part must be calculated. For this, the algorithm above has to be carried out again, this time with $c_i|\psi_0\rangle = |f_0\rangle$ as the first Lanczos vector. Just as in subsection 5.1.5 was explained, there are no specific rules to choose the weights if using multiple target states, as is the case here. For our purposes, we assigned half of the total weight to the ground state and the rest weight is shared between the other states.

5.2.3 Correction vector method

Even though the Lanczos vector method gives us an insight to the whole spectrum in two steps (done for the right and left branches), the information obtained is reliable only for low-lying frequencies. If one looks for calculation of dynamic properties even at regions of higher excited states, then the correction vector method offers a reasonable solution [42]. If we are interested in regions of the Hilbert space with a specific frequency ω or $z = \omega + i\eta$, we select as target states the following:

$\|\psi_0\rangle$	the ground state
$\|A_q\rangle = A_q\|\psi_0\rangle$	the first Lanczos vector
$\|x(z)\rangle = \frac{1}{z-H}\|A_q\rangle$	the correction vector

With the correction vector, the Green's function can be calculated directly as:

$$G(q,z) = \langle A_q|x(z)\rangle. \tag{5.64}$$

We expect that after convergence using the target states above, the system will be optimally described to allow for the calculation of the Green's function for a given frequency ω and a broadening factor η. The correction vector is, by definition, written as a complex quantity, and for a better handling of it, we will split it into a real (x_{re}) and an imaginary part (x_{im})

$$\begin{aligned} |x(z)\rangle &= \frac{1}{\omega - H + i\eta}|A_q\rangle \\ &= \frac{\omega - H}{[\omega - H]^2 + \eta^2}|A_q\rangle - i\frac{\eta}{[\omega - H)]^2 + \eta^2}|A_q\rangle \\ &= |x_{re}\rangle + i|x_{im}\rangle \end{aligned}$$

Furthermore, the real part can be derived from the imaginary one

$$\eta|x_{re}\rangle = \big[H - \omega\big]|x_{im}\rangle$$

In this way, calculating the correction vector reduces actually to calculating the imaginary part only, which we can rewrite as

$$\big[[\omega - H]^2 + \eta^2\big]|x_{im}\rangle = -\eta|A_q\rangle \tag{5.65}$$

[8] In homogeneous or symmetric systems this occurs around the middle of the chain.

This is a system of linear equations of the form $A\mathbf{x} = \mathbf{b}$, where A is in general a non-symmetric matrix and $\mathbf{x}$ and $\mathbf{b}$ are vectors. It can be solved using the restarted version of the generalized minimal residual method, GMRES [29]. Grosso modo, this method works in the following way: at the kth iteration, the GMRES computes the solution estimate $\mathbf{x}_k$ that minimizes the Euclidean norm of the residual $\mathbf{r}_k$ =$\mathbf{b}$ - A$\mathbf{x}_k$ over a subspace of dimension k, this estimation will be recycled and used as a better initial guess to restart the algorithm, so that as each iteration enlarges the minimizing subspace, the residual norm decreases monotonically until convergence. A matter of concern about the GMRES method is that, even when the residual norm remains monotonic, the restarted process can stagnate with a non-zero residual, failing to ever converge.

Contrary to the Lanczos method that allows for display of the whole spectrum at a time, the correction vector method concentrates only in the region of frequency ω, giving the corresponding peak broaden by the factor η. This means that the process has to run for every value of the frequency. The most elaborated part of Eq. (5.65) is the inversion of the Hamiltonian to obtain the imaginary part of the correction vector, furthermore we can see that the closer ω is to an eigenvalue of the Hamiltonian, or the smaller the broadening factor η is, the more singular the system becomes. A large value of η, on the other hand, makes the Hamiltonian closer to a diagonal matrix, speeding up the process, but at the same time, losing resolution of the spectrum.

5.2.4 Construction of operators for open systems

In the last sections we have discussed the calculation of the Green's function and spectral densities associated to a specific operator A_q in the momentum space. We also mentioned that since we are studying systems in real space, the momentum in not a good quantum number. The operators though must be represented in momentum space. An operator A_n in real space for infinite systems can be Fourier transformed to its momentum representation A_q, with wavevector q:

$$A_q = \sum_{n=-\infty}^{\infty} A_n e^{ix_n q} \tag{5.66}$$

$$A_n = \frac{1}{2\pi} \int_{-\pi}^{\pi} \mathrm{d}q A_q e^{-ix_n q}, \tag{5.67}$$

where x_n is the position of site n, and the lattice spacing is taken as the unit. For finite systems under OBC[9], the operators in momentum space are constructed as wavepackets of finite spatial extent and finite uncertainty in the momentum by inserting a filter function $F(x)$ in Eq. (5.66). The filter should first eliminate the effects of the edges, and second, it must have such a form that the uncertainty in the wavevector Δq of the operator remains small. A first choice of the filter could be a Gaussian function, for which the product of uncertainties $\Delta x \Delta q$ is minimum. However, a more appropriate suggestion was made by Kuehner [42], who chose a Parzen filter defined as

$$F(x) = \begin{cases} 1 - 6|x|^2 + 6|x|^3 & \text{if } 0 \leq |x| < 1/2 \\ 2(1-|x|)^3 & \text{if } 1/2 \leq |x| \leq 1 \end{cases} \tag{5.68}$$

For operators in real space, instead of using the complex form of (5.66), we will handle

[9] Under OBC the DMRG yields results with the highest numerical precision.

the real and imaginary part separately, namely

$$\begin{aligned} A_q &= \sum_{n=-\infty}^{\infty} \cos(qx_n) f(x_n) A_n \\ &= \frac{1}{4\pi} \int \mathrm{d}q' (A_{q'} + A_{-q'}) f(q-q'), \end{aligned} \tag{5.69}$$

and

$$\begin{aligned} A_q &= \sum_{n=-\infty}^{\infty} \sin(qx_n) f(x_n) A_n \\ &= \frac{1}{4\pi i} \int \mathrm{d}q' (A_{q'} - A_{-q'}) f(q-q'), \end{aligned} \tag{5.70}$$

where $f(x_n) = F(\frac{x_n}{M})$, with $2M$ the width of the window filter. We will use systems with even number of sites and offset x_n so that $x = 0$ is in the center of the system. The sites closest to the middle of the chain are then $x = 1/2$ and $x = -1/2$. In terms of the sine and cosine components, the Green's function is

$$\begin{aligned} G(q,z) &= \langle\ A_q^\dagger | \frac{1}{z-H} | A_q\ \rangle \\ &= \frac{1}{4} \langle\ (A_q^\dagger \pm A_{-q}^\dagger) | \frac{1}{z-H} | (A_q \pm A_{-q})\ \rangle, \end{aligned} \tag{5.71}$$

where the plus sign corresponds to the cosine term, and the minus sign to the sine component. Furthermore, $\langle\ A_q^\dagger | \frac{1}{z-H} | A_q\ \rangle = \langle\ A_{-q}^\dagger | \frac{1}{z-H} | A_{-q}\ \rangle$ and $A_{-\pi} = -A_\pi$, and one can recognize three different cases for the Green's function: for $A_q = \sum_n \cos(qx_n) A_n$ the Green's function is

$$G(q,z) = \begin{cases} \frac{1}{2} \langle\ A_q^\dagger | \frac{1}{z-H} | A_q\ \rangle & \text{for } 0 < q < \pi \\ \langle\ A_q^\dagger | \frac{1}{z-H} | A_q\ \rangle & \text{for } q = 0 \\ 0 & \text{for } q = \pi \end{cases} \tag{5.72}$$

And for for $A_q = \sum_n \sin(qx_n) A_n$,

$$G(q,z) = \begin{cases} \frac{1}{2} \langle\ A_q^\dagger | \frac{1}{z-H} | A_q\ \rangle & \text{for } 0 < q < \pi \\ 0 & \text{for } q = 0 \\ \langle\ A_q^\dagger | \frac{1}{z-H} | A_q\ \rangle & \text{for } q = \pi \end{cases} \tag{5.73}$$

For $q = 0$ ($q = \pi$), the cosine (sine) term will give the full Green's function. For $0 < q < \pi$, the Green's function is obtained by calculating the cosine and sine components and adding them up. To reduce the finite-size effect on the Green's function it is required that $\pi^2 = \int \mathrm{d}q f(q)^2$ for the filter function. For the Parzen filter, this renders an additional prefactor of $\sqrt{140\pi/151M}$, which must be included in the filter.

SUMMARY

In this chapter we explained the density-matrix renormalization group method and showed how it uses the density matrix rather than an effective Hamiltonian to renormalize a one-dimensional system. The use of the density matrix to select the most probable states of a system allows for a controlled truncation of the Hilbert space. By keeping the size of the Hilbert space fixed, we can handle large chains using the infinite-size and

finite-size algorithms. Equilibrium properties such as expectation values of operators and static correlation functions can be calculated straightforwardly. Dynamic properties at zero temperature can be also calculated using Green's functions techniques combined with the Lanczos vector method, which gives information on the system at all frequencies, or the correction vector method, which give information on the system at a specific frequency at a time. The DMRG is a method in real space and therefore not suitable for calculations in momentum space. However, one can construct operators in momentum space by Fourier transforming the operators in real space. A filter window is then used to avoid undesired effects due to the edges of the systems. With these numerical methods we will calculate ground state properties of both homogeneous and inhomogeneous one-dimensional systems. By measuring the density-density correlation function we will find out if the TLL description is still valid to describe inhomogeneous systems.

Chapter 6

Numerical results for one-dimensional systems

We investigated one-dimensional homogeneous as well as inhomogeneous systems using the DMRG method. Analytical results for the half-filling case of homogeneous systems are known from the Bethe Ansatz method explained in chapter 4. Away from half-filling the (quasi) one-dimensional systems are conductors and display a Luttinger liquid behavior. Close to half-filling, on the other hand, nearly every site is singly occupied, leaving only a very low density of holes in the system. In this case, the important interaction is the short-range repulsion between the holes. At half-filling ($k_F = \pi/2$) there is a gap in the charge excitation spectrum due to umklapp scattering, which transfers two particles from one branch of the linear dispersion to the other[1]. The umklapp term can be bosonized following the formalism of chapter 3, mapping the system to a spinless fermion model with ground state energy $E_K = \pm[v_F^2(k \pm \pi/2)^2 + \Delta^2]^{1/2}$, where the gap is given by $\Delta = g_3/(2\pi\alpha)$, and α is a constant. This result indicates that the system is an insulator [34]. In the next sections we will show the results for both homogeneous and inhomogeneous systems at different band fillings ($n = N/L$, with N the number of particles on a chain of length L). We begin by presenting results for the ground state energy (per site) and particle density distributions. We will also present the results for the density-density correlation function and values for the TL parameter K_c. In the last part we will present results for spectral densities, obtained using the Lanczos vector method; and for optical conductivity, measured using the correction vector method.

6.1 Ground state energies and density profile

We will briefly recall the layout of the heterostructures defined in chapter 4. The Hubbard heterostructures are chains of length L, where the hopping of the particles is measured by the coupling t and the on-site Coulomb interaction U/t switches between different values. The change in U/t can be sharp, as for heterostructure I; or smooth, as in the case of heterostructure II. In addition, potential walls of height V/t can be introduced, as is the case of heterostructure III. The sites x_L and x_R divide the whole system into three homogeneous regions $U_L = 1.1t$, $U_C = 0.9t$ and $U_R = 1.1t$. The general layout of the systems is shown again in Fig. 6.1.

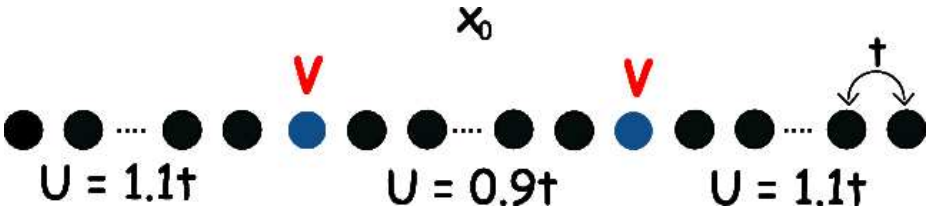

Figure 6.1: General arrangement of a Hubbard heterostructure. The systems consist of a junction of three homogeneous subregions.

[1]Such a process involves a total momentum transfer of $4k_F = 2\pi$ which is a reciprocal lattice vector. Recall Fig. 4.2d in chapter 2.

The DMRG parameters that we used are the next: For the ground state properties of the 240-sites systems we truncated the Hilbert space keeping a total of up to $m = 256$ states. The error due to the truncation can be estimated by adding up the weight of the discarded states, and in Fig. 6.2 we show the total discarded weight as a function of the position for several sweeps. We see that the maximum error is of the order of 10^{-6}. If only one state, i.e., the ground state, is targeted, convergence of the energy is usually achieved after five sweeps (see Fig. 6.3).

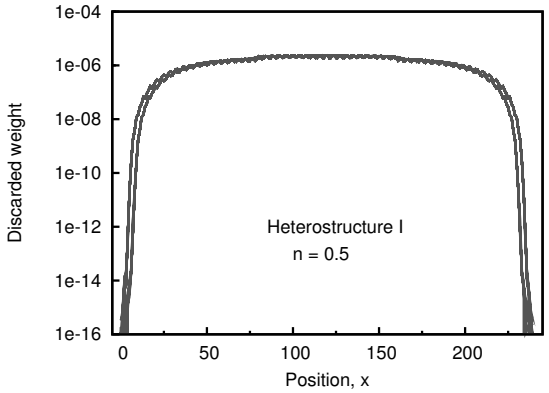

Figure 6.2: Discarded weight for heterostructure I and $n = 0.5$, with maximum error being of the order of 10^{-6}.

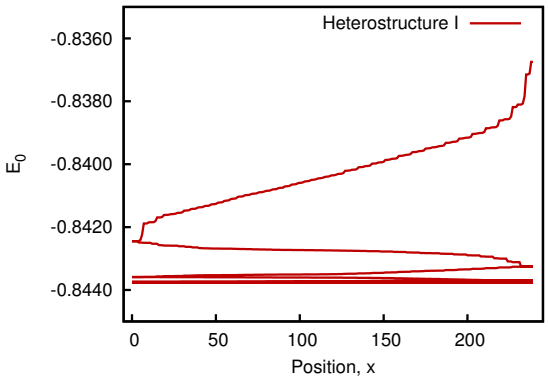

Figure 6.3: Convergence of ground state energy for heterostructure I with $n = 0.5$.

Ground state energy

From the analysis by Lieb and Wu of the one-dimensional Hubbard model, the energy of a system of size L and at half-filling is given by $E = -2tL \int \mathrm{d}k \cos(k)\rho(k)$, where $\int \mathrm{d}k\rho(k) = N/L$ [24]. In Fig. 6.4 we show the DMRG results for half-band filling and compare them to those given by the Bethe Ansatz.

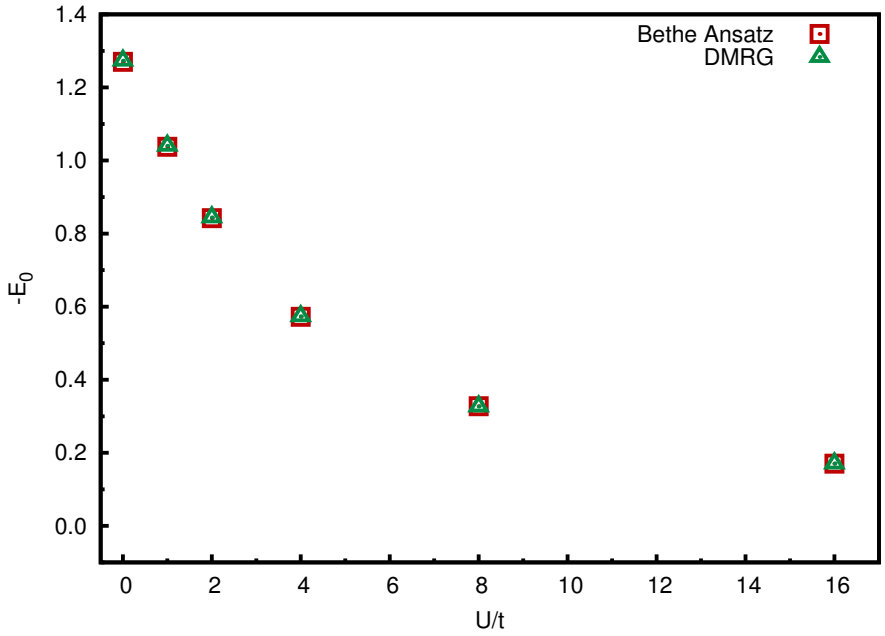

Figure 6.4: Ground state energy as a function of the Coulomb interaction U/t for a homogeneous system at half-band filling. Results obtained from Bethe Ansatz and with DMRG are compared.

Except for the case of half-filling, the equations given by Lieb and Wu cannot be analytically solved. However, the ground state energy away from half-filling has been approximated by Shiba based on the known Bethe ansatz solution [37]. Limiting cases correspond to $U/t = 0.0$, for which $E_0 = (-4/\pi)(\sin(n\pi/2))$, and $U/t \to \infty$, for which $E_0 = -(2/\pi)(\sin(\pi n))$. In Fig. 6.5 we plot the results by Shiba and show the DMRG results for the ground state energy for homogeneous systems as a function of the band filling for different values of the on-site Coulomb interaction.

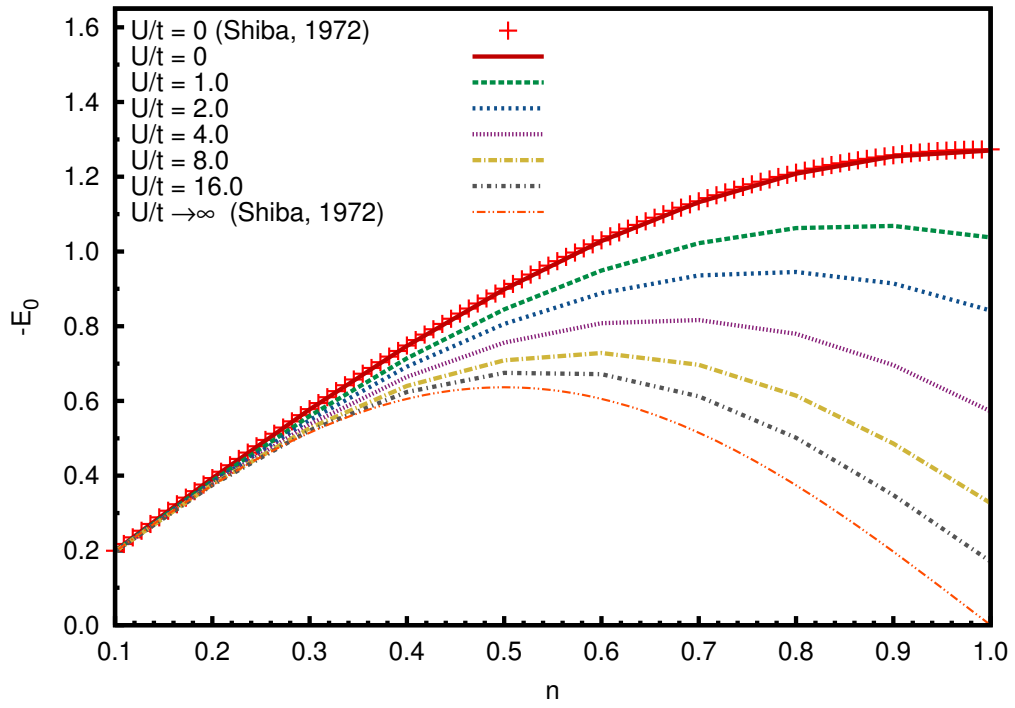

Figure 6.5: Ground state energy as a function of band-filling n for a homogeneous system. $L = 240$, $U/t = 0, 1.0, 2.0, 4.0, 8.0, 16.0$ from top to bottom. The limiting cases $U/t = 0$ and $U/t \to \infty$ correspond to the results by Shiba [37].

In figures 6.6 and 6.7, we present the ground state energy results for inhomogeneous systems. The results can be compared to those of a homogeneous system with $U/t = 1.0$. Figure 6.6 shows the ground state energy per site as a function of the band filling for heterostructures I, II, and for heterostructure III with $V/t = 1.0$. In Fig. 6.7 we show the ground state energy as a function of the band filling for heterostructure III with different heights for the potential barriers. We observe that the ground state energy, even for heterostructure III with $V/t = 10.0$, remains the same for low-particle densities and varies only slightly when approaching to half-band filling.

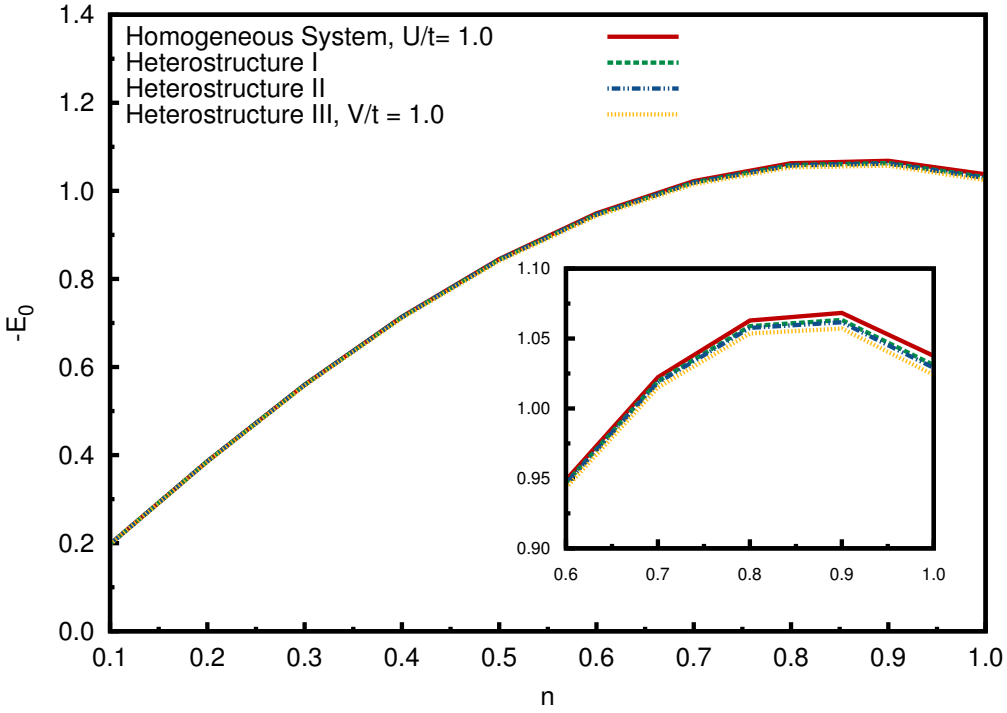

Figure 6.6: Ground state energy as a function of band filling n for heterostructures I, II, and III, as compared to the homogeneous case with $U/t = 1.0$. The inset shows a close up for $0.6 \leq n \leq 1.0$

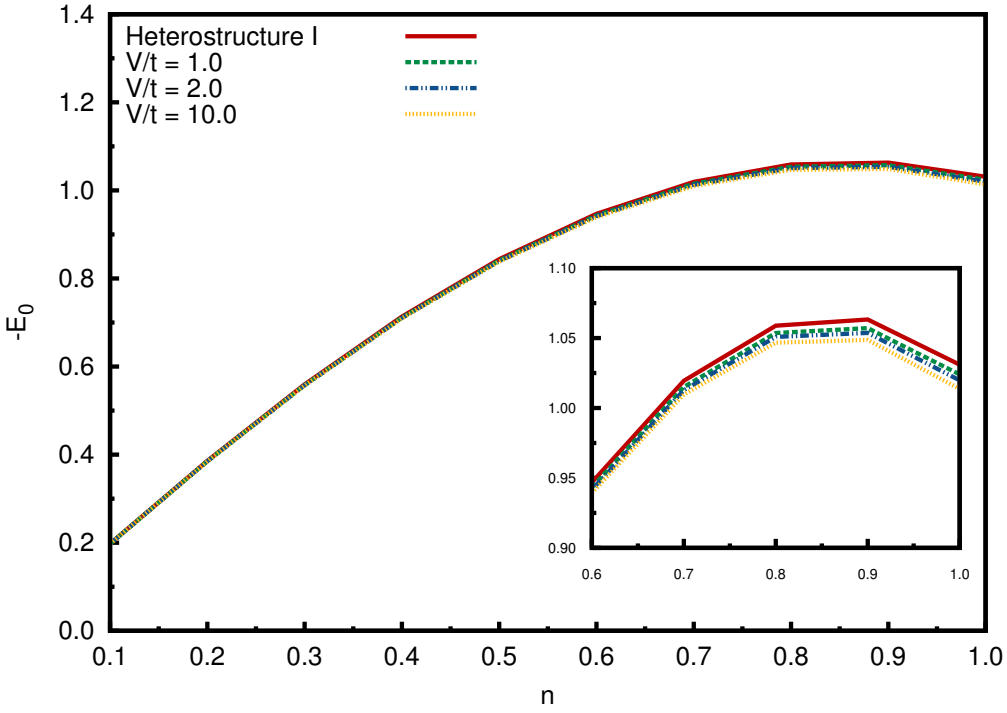

Figure 6.7: Ground state energy as a function of band filling n for heterostructure III with different values of V, as compared to heterostructure I. The inset shows a close up for $0.6 \leq n \leq 1.0$

Density profile

Using systems with open boundary conditions, finite size effects are induced. One example of these effects is the local density oscillations and the charge accumulation close to the edges of the system due to the breaking of the translational invariance. Such density oscillations are called Friedel oscillations[2]. The oscillations appear with wavenumber $2k_F$, and are given by $\delta n(x) \sim \cos(2k_F x + \varphi)x^{-\eta}$, where the exponent η depends on the interaction. The oscillations are shown in figures 6.8-6.17. In the case of the heterostructures, due to the symmetric construction, the charge distribution is expected to be also symmetric with regard to the middle point of the chain. This is the case of heterostructure II (see Fig. 6.9). We observe however, that for heterostructures I and III the symmetry is slightly perturbed. In heterostructure I (see Fig. 6.8) the perturbation takes place only locally at the positions where the on-site Coulomb potential switches values, i.e., x_R and x_L. For our purposes, such small changes are negligible, specially because we will take average over pairs of correlation functions, as will be explained in the next section. It is still observed that the charge density remains fairly homogeneous in the valley of the Coulomb interaction in heterostructure I. In heterostructure III the symmetry is much more affected upon introduction of the potential barriers, as seen from Fig. 6.10 and Fig. 6.11. In Figs. 6.8-6.17, the on-site Coulomb interaction function is plotted with its value given on the right vertical axis.

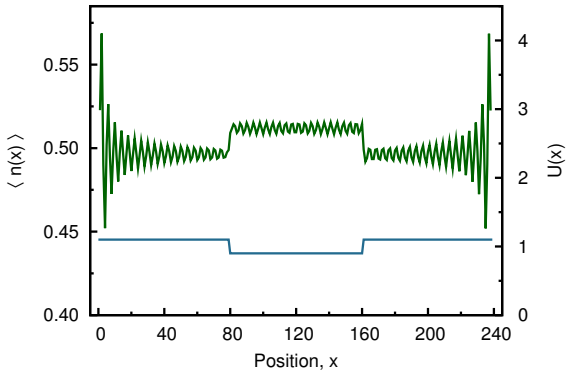

Figure 6.8: Particle density for heterostructure I, with band filling $n = 0.5$. The symmetry breaks locally at x_R and x_L.

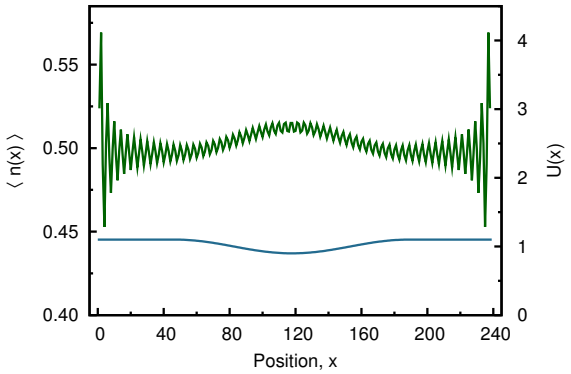

Figure 6.9: Particle density for heterostructure II, with band filling $n = 0.5$. The distribution is completely symmetric.

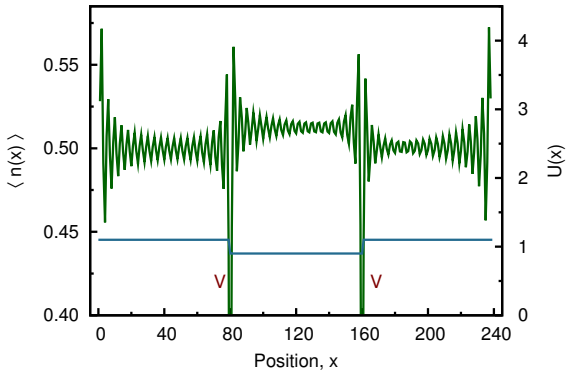

Figure 6.10: Particle density for heterostructure III, with $V/t = 1.0$ and band filling $n = 0.5$.

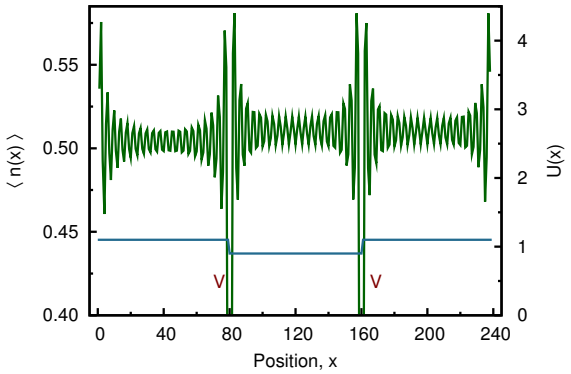

Figure 6.11: Particle density for heterostructure III, with $V/t = 10.0$ and band filling $n = 0.5$.

[2]Such oscillations can also be induced by the presence of an impurity in the system.

In the case of homogeneous systems, the particle distribution is symmetric with regard to the middle point of the system. In figures 6.12-6.17 we show the evolution of the particle density for increasing on-site Coulomb interaction U for systems with band filling $n = 0.5$. We observe that the amplitude of the oscillations decreases with increasing on-site Coulomb interaction.

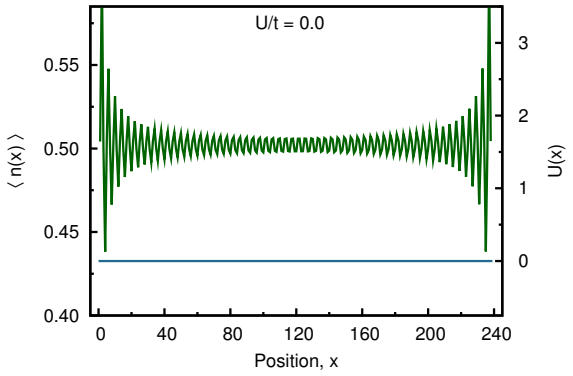

Figure 6.12: Particle density for a tight-binding chain, with $U/t = 0.0$ and band filling $n = 0.5$.

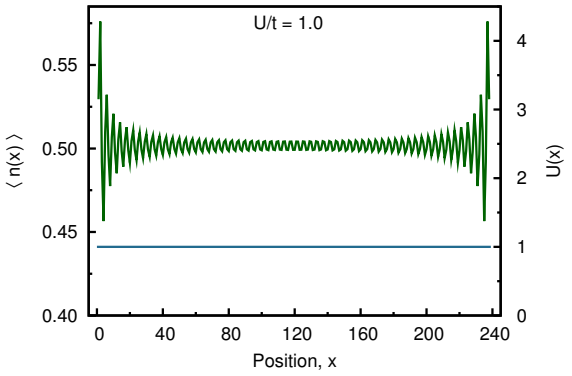

Figure 6.13: Particle density for a homogeneous system, with $U/t = 1.0$ and band filling $n = 0.5$.

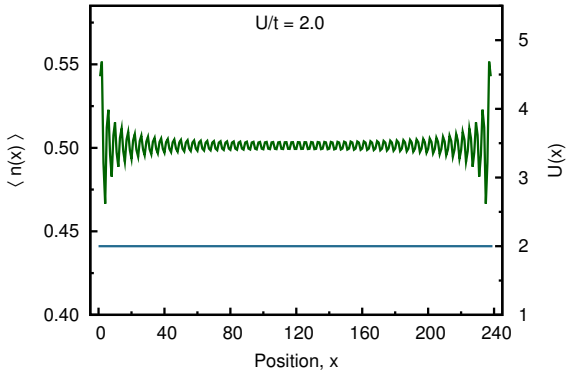

Figure 6.14: Particle density for a homogeneous system, with $U/t = 2.0$ and band filling $n = 0.5$.

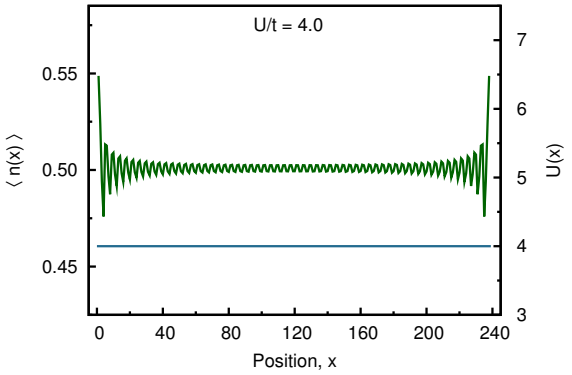

Figure 6.15: Particle density for a homogeneous system, with $U/t = 4.0$ and band filling $n = 0.5$.

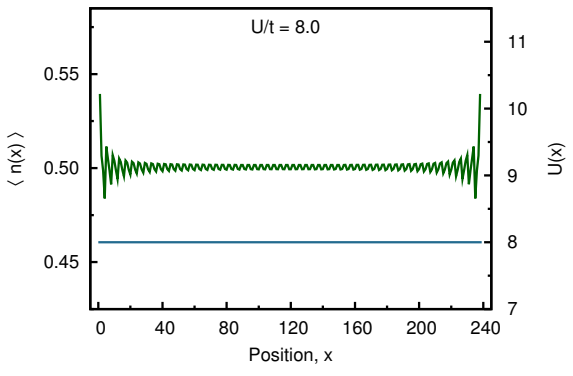

Figure 6.16: Particle density for a homogeneous system, with $U/t = 8.0$ and band filling $n = 0.5$.

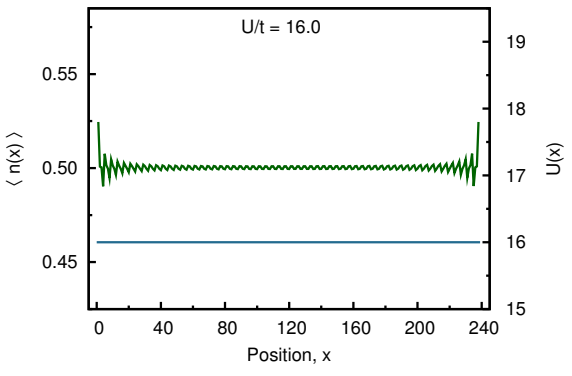

Figure 6.17: Particle density for a homogeneous system, with $U/t = 16.0$ and band filling $n = 0.5$.

6.2 Density-density correlation function

To estimate K_c, we fit the values of the numerical data to the first two terms of Eq. (3.98), i.e.,

$$\langle \rho_c(x)\rho_c(0)\rangle = \frac{K_c}{(\pi x)^2} + \frac{A_1 \cos(2k_F x)}{x^{1+K_c}} \ln(\mathrm{x})^{-\frac{3}{2}}. \tag{6.1}$$

We will see below that, even though the $2k_{\mathrm{F}}$-oscillations could not be fitted in all the cases, the power law decay was clearly observed. A few explanations are needed to detail the fitting of the data. Since we have systems with an even number of sites, there is no site at exactly the middle of the chain, and we chose the closest position to the middle point, namely the site at position $x = 120$, to be the zero of Eq. (6.1), such that the correlation functions will decay symmetrically, in principle, in the direction of the edges of the systems. We can thus speak of two branches of the systems. We will refer to the region from the middle of the chain up to the boundary (we can choose between the site at x_R or at x_L) of the Coulomb valley as the region R_1, and from this point until the end of the chain, as the region R_2. Fig. 6.18 shows the setup of the system for measuring density-density correlations. The symmetric construction of the systems reflects in its properties to a certain degree, as was seen in the density profiles. For the measurement of the correlation function we actually had to choose between the branches, the one who would render the best possible results. In the following we describe in detail the results for each heterostructure.

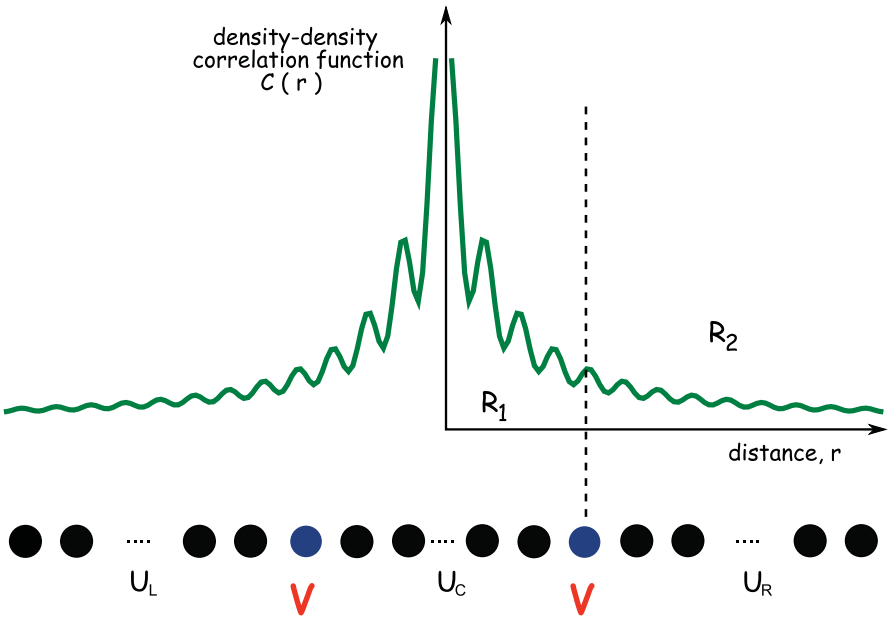

Figure 6.18: Setup of the system for measuring density-density correlations. We can select either the branch formed by the regions U_L-U_C, or U_C-U_R to measure the density-density correlation function.

Heterostructures I and II

Heterostructure I, even with the sharp edges valley in the on-site Coulomb repulsion, did not suffered from significant alterations in the continuous decay of the correlation function, this is seen from the logarithmic plots in figures 6.19 and 6.20, which illustrate both the power-law decay of the density-density correlation function and the $2k_{\mathrm{F}}$-oscillations. For band fillings $0.1 \leq n < 1.0$, the power-law decay extends beyond the boundary point (x_L or x_R) and is not completely constrained to any of the regions R_1 or R_2. However, fitting the $2k_{\mathrm{F}}$-oscillations succeeded over the selected branch only for $n \leq 0.5$. For $n > 0.5$

the fitting was only carried out for the first term of Eq. (6.1), i.e., even though the $2k_F$-oscillations could not be fitted, the power-law decay was still observed. When comparing the results to those for heterostructure II (with an interaction of the form $U(x) \propto \cos(\gamma x)$), the valley along the system remains but the change of $U(x)$ towards the ends of the chain is done in a smoothly way. This variation of U resulted in actually the same values for the correlation functions as already presented, showing that the sharp edges of the on-site Coulomb potential did not influence strongly the Luttinger liquid behavior of the system. Another possible configuration that we studied was a less symmetric one, with $x_L = 70$ and $x_R = 156$. For this arrangement, we found the density-density correlations behavior to be qualitatively the same as for the original arrangement, including the decrease in the value of the K_c for $n > 0.5$.

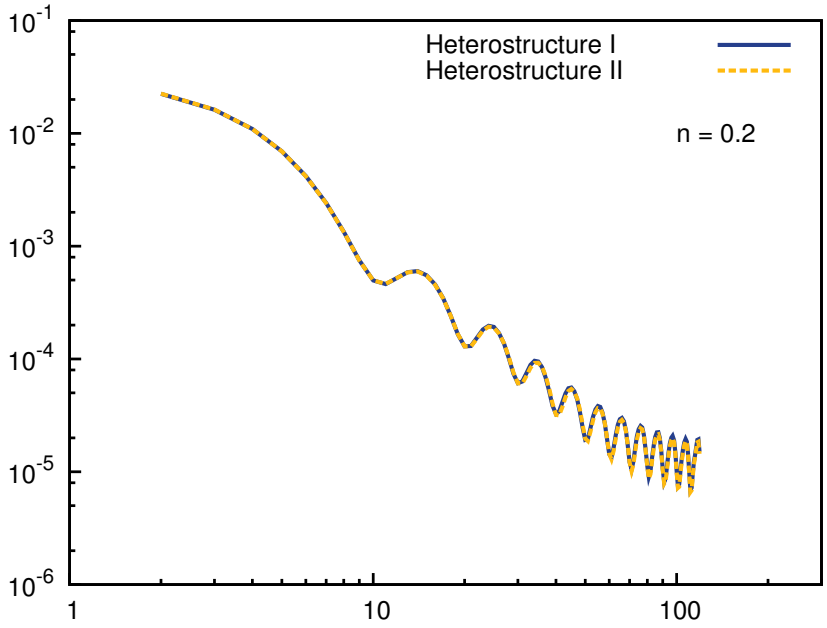

Figure 6.19: Density-density correlation function for heterostructure I (continuous line) and II (broken line), with $n = 0.2$.

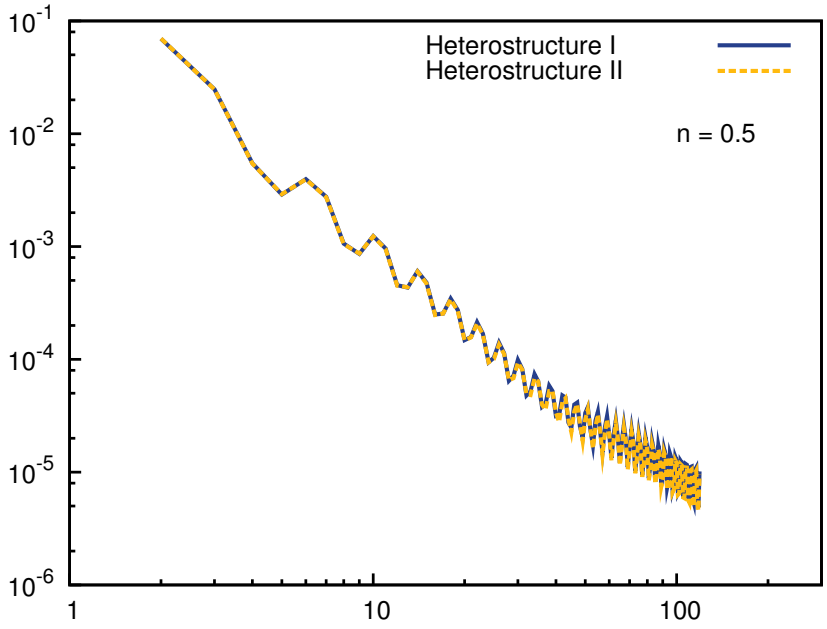

Figure 6.20: Density-density correlation function for heterostructure I (continuous line) and II (broken line), with $n = 0.5$.

The Friedel oscillations can be observed as well in Fig. 6.21 and Fig. 6.22, where the continuous line corresponds to the fitting done according to Eq. (6.1).

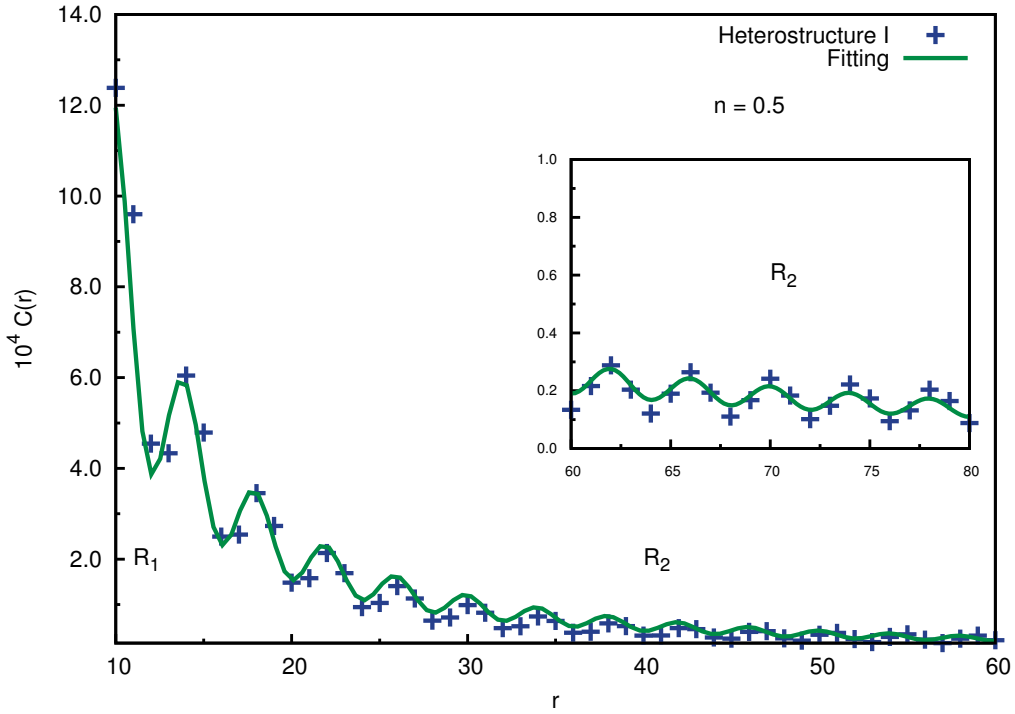

Figure 6.21: Fitting (continuous line) of density-density correlation data for heterostructure I (crosses), with $n = 0.5$. The inset shows a close up of the $2k_F$-oscillations at large distances.

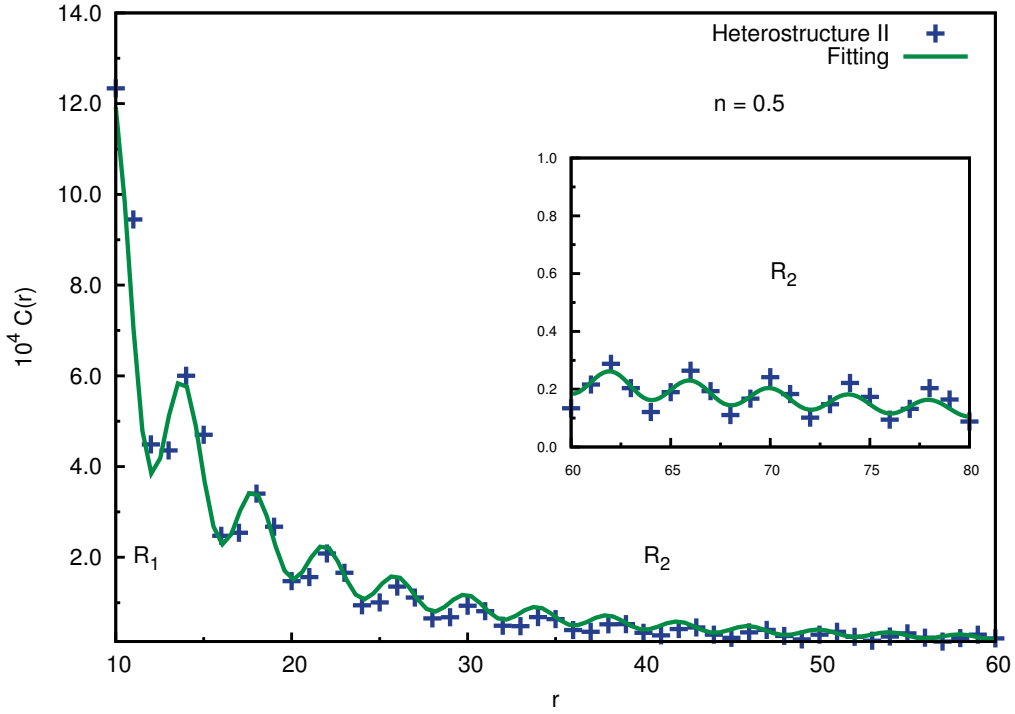

Figure 6.22: Fitting (continuous line) of density-density correlation data for heterostructure II (crosses), with $n = 0.5$. The inset shows a close up of the $2k_F$-oscillations at large distances.

Heterostructure III

In this case, we keep the valley in the Coulomb interaction of heterostructure I: $U_L = U_R = 1.1t$ and $U_C = 0.9t$. Furthermore, we simulated two potential walls by introducing the confining potential $V_{x_L}/t = V_{x_R}/t = V/t$ and $V(x)/t = 0.0$ for the rest of the sites. The results showing the change in the correlation function of the system as a function of the height of the potential is presented in Fig. 6.23, where a close up of the effects close to the transition from region R_1 to R_2 is shown. We studied the system with $V/t = 0.5, 1.0, 3.0, 10.0$ and 20.0. From this figure, we see that for $V/t = 1.0$ there is apparently little influence on the correlation function decay. Indeed, for the band fillings $n = 0.3-0.6$ a TLL was still observed. For $n = 0.3-0.5$ also the $2k_F$-oscillations could be fitted, for $n = 0.6$, as for the previous heterostructures, only the power-law decay was fitted. The results in the case of heterostructure III distinguished strongly from those previously described if $V/t \geq 3.0$. The confining potential V/t at x_L and x_R generated stronger changes from one region to the other for $V/t > 3.0$. Such scattering potential interrupted abruptly the decay of the correlation function, not having further space to fully establish the decay in the amplitude of the $2k_F$-oscillations.

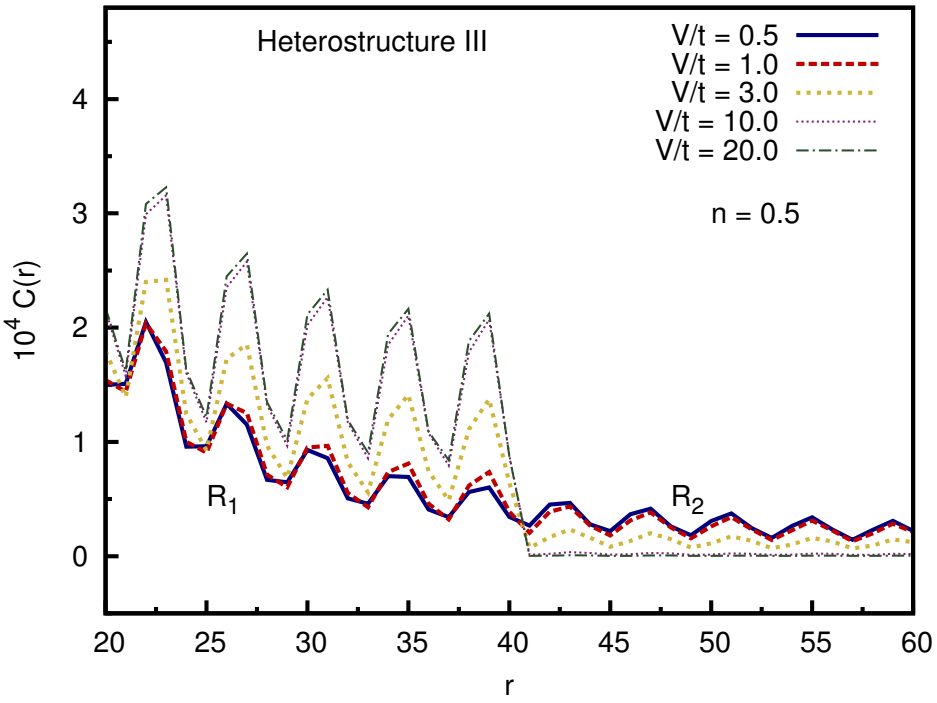

Figure 6.23: Density-density correlation function for heterostructure II for different values of the potential barrier $V_{x_L}/t = V_{x_R}/t = V/t$. With band filling $n = 0.5$.

In figures 6.24-6.26 we show the logarithmic plot of the the density-density correlation function for heterostructure III for different values of the band filling and with $V/t = 1.0$. In this case, the correlation function decays continuously for band fillings $0.3 \leq n \leq 0.6$. For other values of the band filling the behavior is strongly affected by the presence of the potential, as we can see, for example, for $n = 0.2$ in Fig. 6.24. We compare the results to those in the case of heterostructure I.

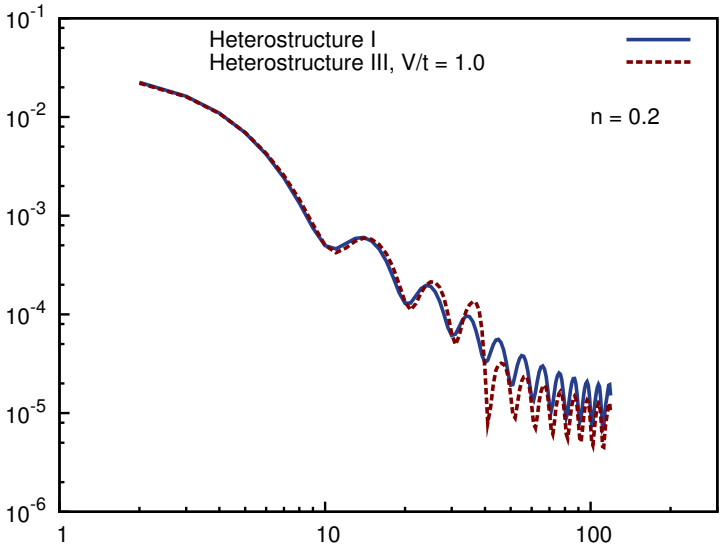

Figure 6.24: Density-density correlation function for heterostructure I (continuous line) and III (broken line), with $n = 0.2$.

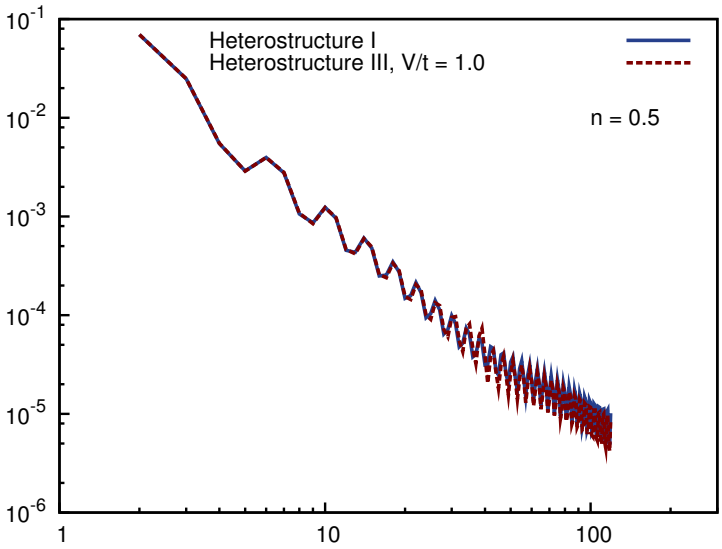

Figure 6.25: Density-density correlation function for heterostructure I (continuous line) and III (broken line), with $n = 0.5$.

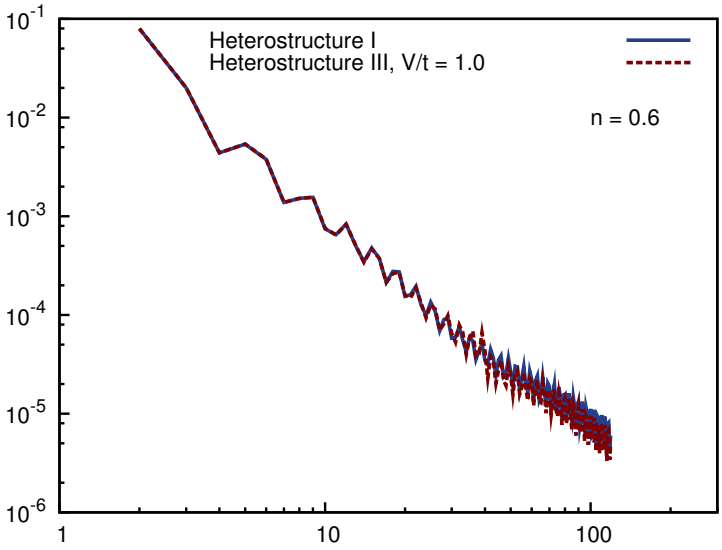

Figure 6.26: Density-density correlation function for heterostructure I (continuous line) and III (broken line), with $n = 0.6$.

In Fig. 6.27 we show a closer view of the $2k_F$-oscillations and the corresponding fitting for $n = 0.5$. In 6.28 we see from the inset that the $2k_F$-oscillations cannot be accurately fitted. In this case, we only calculated the power-law decay.

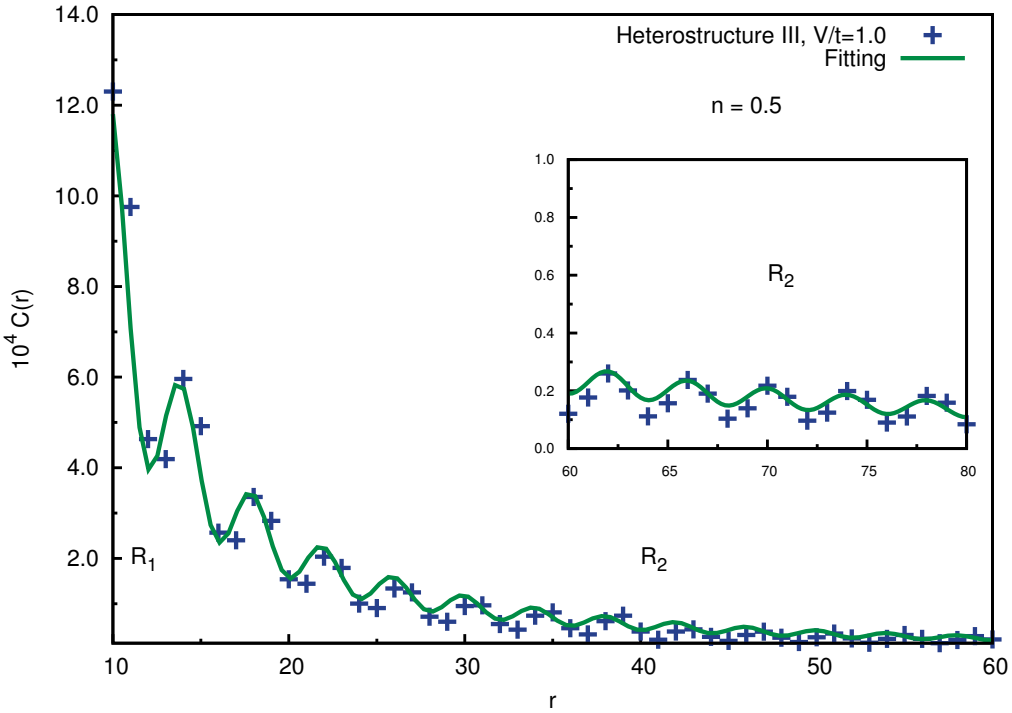

Figure 6.27: Fitting (continuous line) of density-density correlation data for heterostructure III (crosses), with $n = 0.5$. The inset shows a close up of the $2k_F$-oscillations at large distances.

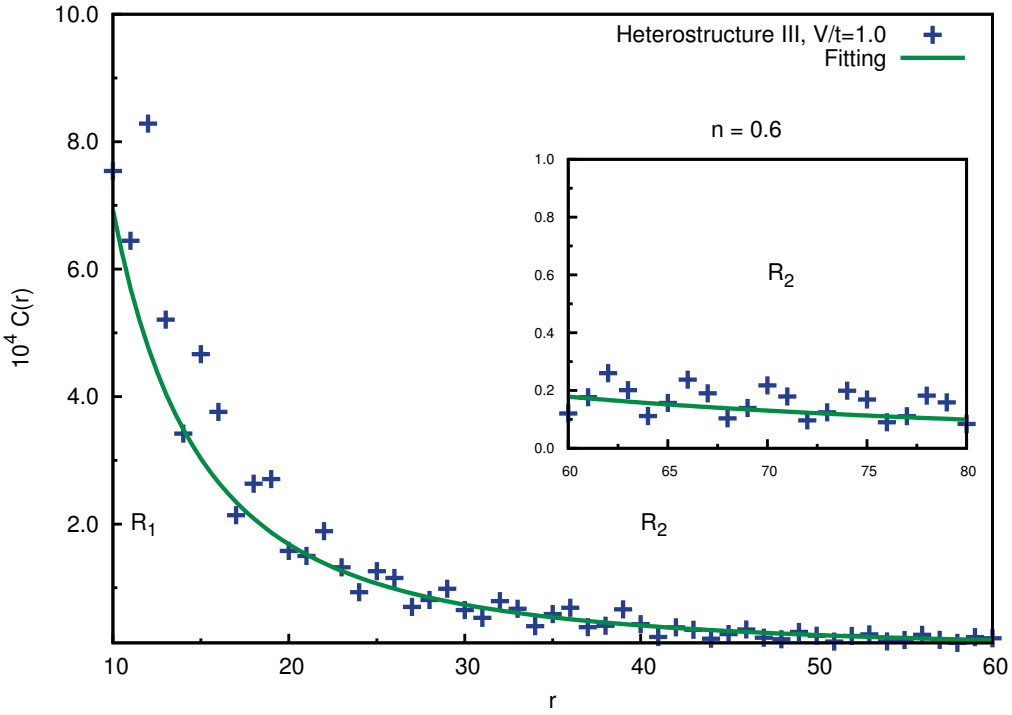

Figure 6.28: Fitting (continuous line) of density-density correlation data for heterostructure III (crosses), with $n = 0.6$. The $2k_F$-oscillations cannot be accurately fitted in this case, as shown in the inset.

Tomonaga-Luttinger parameter, K_c

As a test for our numerics, we considered the case of a homogeneous chain for which we confirmed the results obtained from the Bethe Ansatz for the correlation functions [32, 9]. In Fig. 6.29 we show our results for several values of U obtained with a homogeneous chain of length $L = 240$ sites.

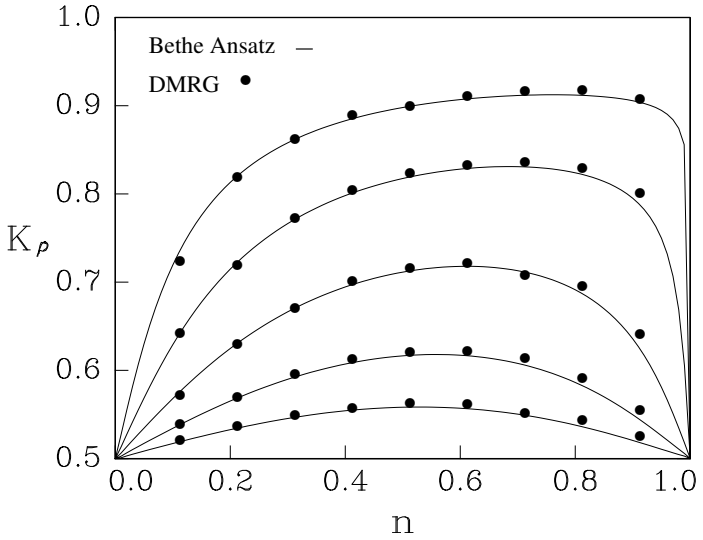

Figure 6.29: Tomonaga-Luttinger parameter as a function of the band filling n for the homogeneous Hubbard lattice compared to our DMRG data (dots). $U = 1.0, 2.0, 4.0, 8.0, 16.0$ from top to bottom.

In figure 6.30, the results for K_c are shown as a function of the band filling, including the homogeneous case with $U/t = 1.0$ for comparison. For heterostructure I $K_c < 1.0$, which indicates that spin or charge density waves are present. Let us recall that for both heterostructures I and III, for $n \leq 0.5$ the $2k_F$-oscillations were clearly observed and fitted accurately, whereas for $n \geq 0.6$, even though there are oscillations present, they do not match the $2k_F$-component as expected. Still, the power-law decay of the correlation function was confirmed. This behavior is also reflected on the values of K_c, and we observe in Fig. 6.30, two different values sets for the density intervals already mentioned, finding that there is a drop in the K_c's values for $n \geq 0.6$.

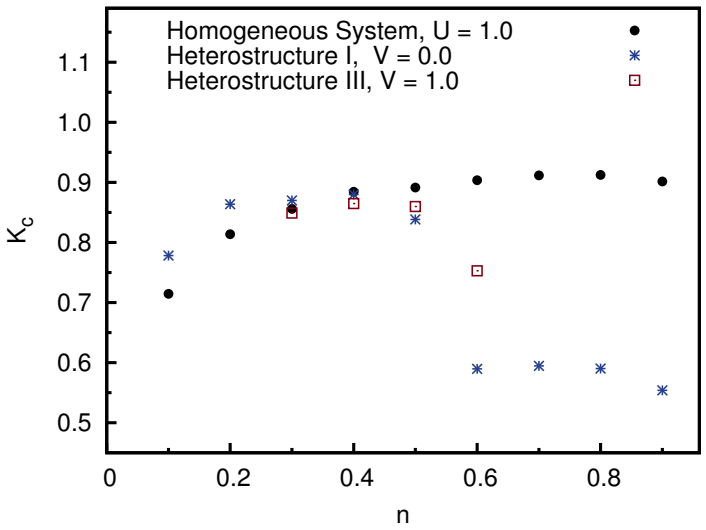

Figure 6.30: TL parameter K_c for both heterostructures as a function of the band filling as compared to the results for the homogeneous system with $U = 1.0$. For *heterostructure I* $K_c < 1.0$, indicating a Luttinger liquid behavior.

6.3 SPECTRAL DENSITY AND OPTICAL CONDUCTIVITY

Spectral density

Spectral functions are useful to understand the electronic structure of solids. Let us briefly recall what kind of information we obtain through them. The spectral function $A(q,\omega)$ is the probability that an electron has momentum q and energy ω. The spectral functions are defined by (see Eq. (5.42)):

$$A^+(q,\omega) = \sum_\alpha |\langle\alpha|c_q^\dagger|\psi_0\rangle|^2\ \delta(w-(E_\alpha - E_0)),$$
$$A^-(q,\omega) = \sum_\beta |\langle\beta|c_q|\psi_0\rangle|^2\ \delta(w+(E_\beta - E_0)).$$

Creation and annihilation operators, $c_q^\dagger$ and c_q respectively, are represented in momentum space, constructed in the way described in section 5.2.4. $|\psi_0\rangle$ is the ground state wavefunction of the N-particle system, $|\alpha\rangle$ are states of the system after adding a particle $(N+1)$, and $|\beta\rangle$ are states of the system after removing a particle $(N-1)$. A^+ can be measured in angular-resolved inverse photoemission, and A^- in photoemission experiments. $A(q,\omega)$ represents thus a quasiparticle state of the system. For non-interacting systems, the spectral function is a delta function located at $\omega = \varepsilon(q)$[3]. For interacting systems, the spectral function has a broadening $\Delta(q)$, which may be related to the lifetime $\tau(q)$ of the state by $\tau = \hbar/\Delta$. In higher dimensions, the effect of electron-electron interactions can be observed in different ways: As a broadening of the quasiparticle peak, as a shift of the energy of the quasiparticle band, or as a renormalization of the weight of the peak, due to the appearance of an incoherent background. In 1D there is no quasiparticle peak in the spectral function. Instead, one finds two divergences due to spin-charge separation located at $\pm u_{s,c}q$, where $u_{s,c}$ are spin and charge group velocities. Unambiguous experimental signatures of spin-charge separation are scarce in quasi-one dimensional materials, one exception being the organic molecule TTF-TCNQ[4] [39], whose spectrum dispersion can be mapped onto separated spin and charge excitation bands of the 1D Hubbard model away from half-filling. The case of half-filled Hubbard chains, as we mentioned, must be considered apart. Due to short-range antiferromagnetic correlations, extra weight is created near the Fermi energy, finding thus a peak with finite broadening. To calculate spectral densities following the Lanczos vector method introduced in section 5.2.2, we kept the ground state ψ_0 and $N_L = 4$ or $N_L = 8$ Lanczos vectors, with up to $m = 256$ states in the DMRG basis and a broadening factor $\eta = 0.1$.

In Fig. 6.31 we show the spectral density as function of the wavevector q for heterostructure I at half-filling. The first four Lanczos vectors were kept as well as the ground state. We observe that the peaks, shifted by the chemical potential μ, can be identified with the dispersion $\varepsilon(q) = -2t\cos(q)$.

[3] $\varepsilon(q)$ is the energy dispersion relation of the system.
[4] Tetrathiafulvalene-tetracyanoquinodimethane, TTF-TCNQ.

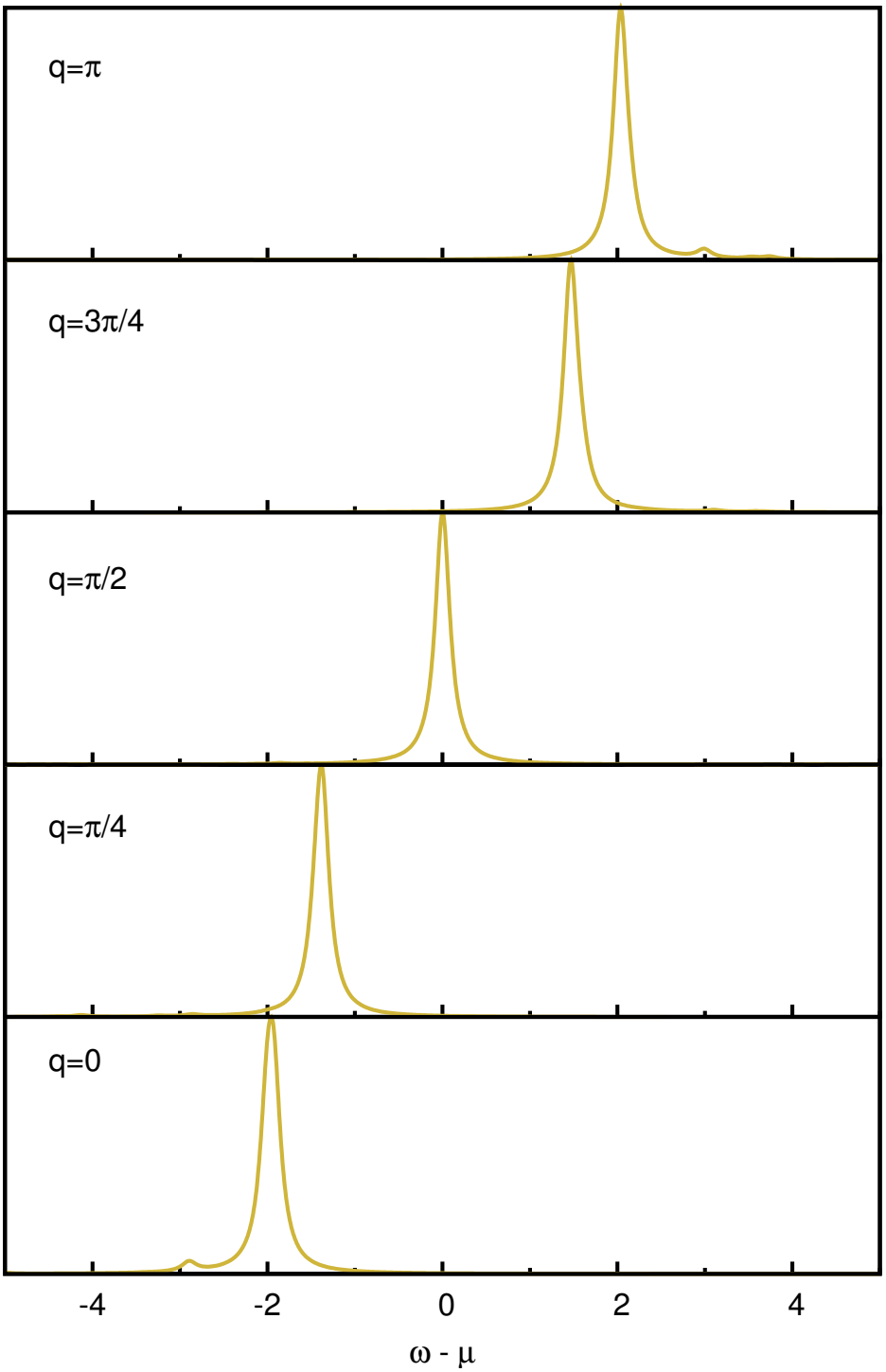

Figure 6.31: Spectral density as a function of the wavevector q of heterostructure I at half-filling. We used the ground state ψ_0 and the first four Lanczos vectors, $N_L = 4$. The broadening factor is $\eta = 0.1$ and we kept $m = 256$ states. Observe that the position of the peaks can be identified with the dispersion relation $\varepsilon(q) = -2t\cos(q)$.

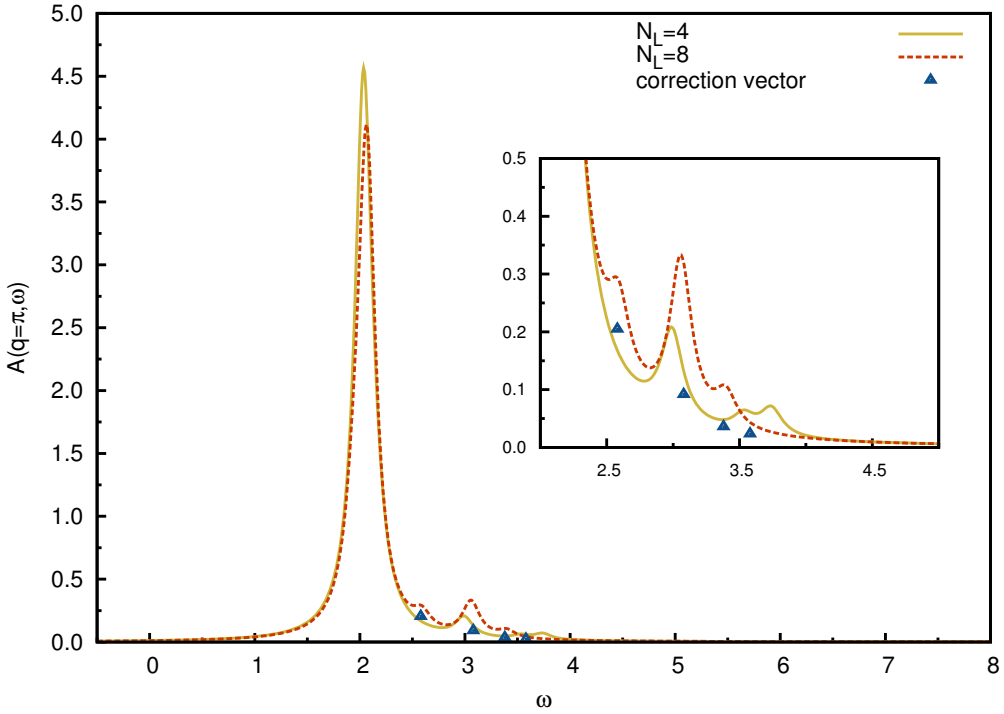

Figure 6.32: Sector of the spectral density function with wavevector $q = \pi$ of heterostructure I. We used the ground state $|\psi_0\rangle$ and the first four ($N_L = 4$), and eight ($N_L = 8$) Lanczos vectors. The broadening factor is $\eta = 0.1$. The inset shows results obtained using one correction vector, with $\eta = 0.1$ and $m = 256$ basis states.

In Fig. 6.32 we show the spectral density at $q = \pi$, with $N_L = 4$ and $N_L = 8$ Lanczos vectors. We observe that the Lanczos vector method does not converge in higher-energy regions, for which we include some points obtained using the correction vector method.

Optical conductivity

The linear optical absorption is proportional to the real part $\sigma_1(\omega)$ of the optical conductivity, which is related to the imaginary part of the current-current correlation function by

$$\sigma_1(\omega > 0) = \frac{1}{\omega} \mathrm{Im}\ \chi_{JJ}(\omega > 0), \tag{6.2}$$

and

$$\begin{aligned} \chi_{JJ}(\omega > 0) &= -\frac{1}{L}\langle\psi_0|J\frac{1}{\omega - (H - E_0) + i\eta}J|\psi_0\rangle \\ &= -\frac{1}{L}\sum_n \frac{\langle\psi_0|J|n\rangle}{\omega - (E_n - E_0) + i\eta}, \end{aligned} \tag{6.3}$$

where we introduced the set of states $|n\rangle$ with corresponding energies E_n. The current operator J is given by

$$J = -t \sum_{i,\sigma=\uparrow,\downarrow} \left(c^\dagger_{i\sigma} c_{i+1\sigma} - c^\dagger_{i+1\sigma} c_{i\sigma} \right). \tag{6.4}$$

To calculate σ_1, we constructed the momentum representation of the current operator and used the method described in section 5.2.3, with the correction vector

$$|x(\omega)\rangle = \frac{1}{\omega - (H - E_0) + i\eta} J_q|\psi_0\rangle. \tag{6.5}$$

The DMRG calculations were performed keeping $m = 128$ basis states of the Hilbert space, with a broadening factor $\eta = 0.1$. In chapter 3 we wrote the bosonization of Fermi field operators, products of such operators can be also written for current, spin or electron density operators. The current operator is given by[5]

$$J(x,t) = \frac{e}{\pi}\partial_t \phi_c(x,t), \tag{6.6}$$

$\phi_c(x,t)$ is the boson field introduced in Eq. (3.87) and e is the electron charge. In [11], the optical conductivity for a one-dimensional Hubbard chain at half- filing was studied. If only scattering states of holons[6] (h) and antiholons ($\bar{h}$) are considered, the contribution to the real part of the optical conductivity is given by[7]

$$\begin{aligned}\sigma_{h\bar{h}} =& \frac{e^2 t}{a_0}\frac{u_c}{v_F}\frac{\sqrt{\omega^2 - 4\Delta^2}}{\omega^2}\theta_H(\omega - 2\Delta) \\ & \times \exp\left[-\int_0^\infty \frac{\mathrm{d}x}{x}\frac{\exp(-x)[1 - \cos(4x\theta_0/\pi)\cosh(2x)]}{\cosh(x)\sinh(2x)}\right],\end{aligned} \tag{6.7}$$

where a_0 is the lattice spacing, θ_H is the Heaviside function, Δ is the charge gap and $\theta_0 = \operatorname{arcosh}(\omega/2\Delta)$. In the case of $U/t = 3.0$, we have $\Delta(U/t = 3.0) = 0.315687$ and $u_c/v_F \sim 1.22371$. In Fig. 6.33 we show the results after plugging these values into Eq. (6.7) and compare to the results obtained using the correction vector method.

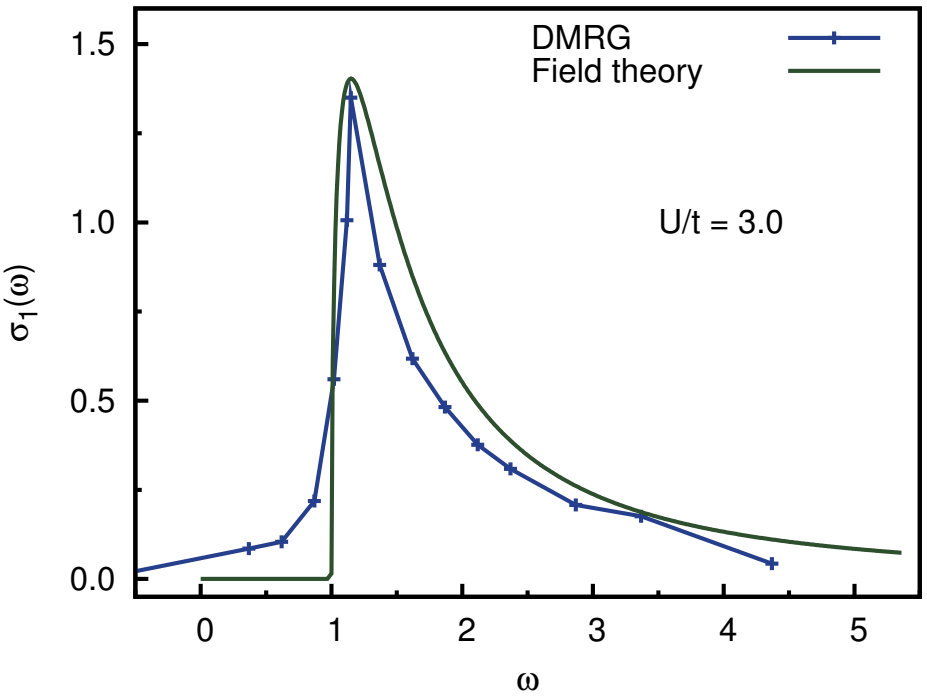

Figure 6.33: Optical conductivity for a homogeneous one-dimensional Hubbard chain for $U/t = 3.0$ compared to results from field theory. The chain length is $L = 128$ sites and we kept $m = 128$ states in the DMRG basis.

In Fig. 6.34 we show the optical conductivity of the one-dimensional Hubbard model calculated using the correction vector method for $U/t = 3.0, 6.0$. Observe that the width of the spectrum decreases with decreasing on-site Coulomb interaction. The results can be compared to those obtained in [20].

[5] This is the linear response result obtained from the conservation law for the charge, $\frac{\partial \rho(x,t)}{\partial t} + \vec{\nabla}\cdot\hat{J} = 0$.

[6] Gapped, spinless excitations carrying charge $\pm e$ are called antiholons and holons, respectively.

[7] Since the current operator is neutral, only intermediate states with equal number of holons and antiholons will contribute to the current-current correlation function.

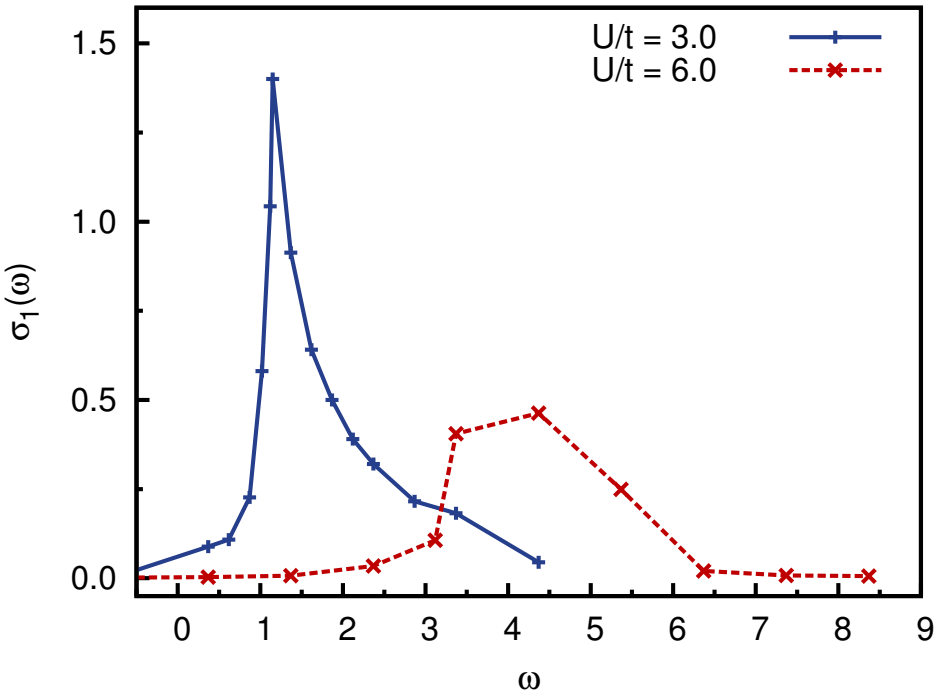

Figure 6.34: Optical conductivity for a homogeneous one-dimensional Hubbard chain for $U/t = 3.0$ and $U/t = 6.0$. The chain length is $L = 128$ sites and we kept $m = 128$ states in the DMRG basis, with a broadening factor $eta = 0.1$.

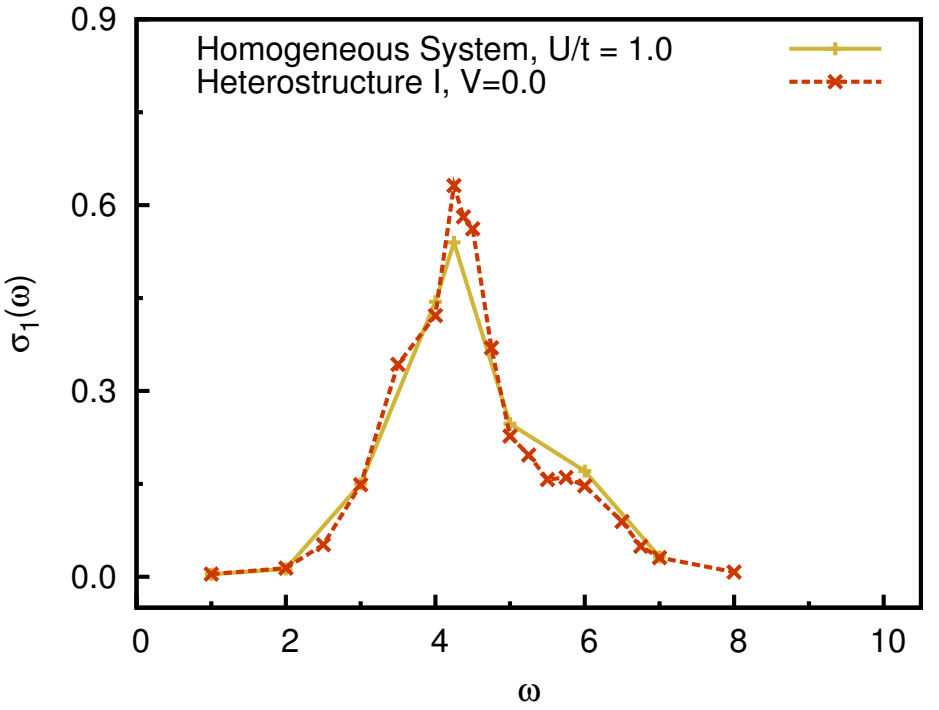

Figure 6.35: Optical conductivity for heterostructure I compared to the results for a homogeneous one-dimensional Hubbard chain of length $L = 240$ sites, with $U/t = 1.0$. In both cases we kept $m = 128$ states in the DMRG basis, with a broadening factor $eta = 0.1$..

In Fig. 6.35 we show the optical conductivity of heterostructure I and compare the results to those for a homogeneous one-dimensional Hubbard chain of length $L = 240$ sites, with $U/t = 1.0$.

SUMMARY

In this chapter we summarized our findings on homogeneous and inhomogeneous one-dimensional systems. Results for ground state properties included ground state energy values. In the homogeneous half-filling case, the results could be directly compared to those obtained using Bethe Ansatz [24]. Away from half-filling, the energies matched the results given by the approximation by Shiba [37]. In chapter 3, we found from the exact solution of the Tomonaga-Luttiger model, that the power law decay of the correlation functions is characterized by the parameter K_c, for the charge regime. K_c is determined by microscopic coupling constants which cannot be directly measured. Using the DMRG method to calculate the density-density correlation function, we estimated the value of K_c. In the homogeneous regime, our results are in good agreement with those reported by [32] and [9]. In the inhomogeneous regime, i.e., for the heterostructures, we found that a slow variation of the on-site Coulomb potential, as in the case of heterostructures I and II, does not interrupt the decay of the density-density correlation functions between the subregions and the system as a whole behaves as a TLL, with $K_c < 1$. A different behavior results from the introduction of a scattering potential at the junctions between the subregions, as was the case of heterostructure III. In this case, there is a threshold value for the height of the potential, after which the central region (with $U_C = 0.9t$) is isolated from the other components (U_L and U_R) of the system. Even though the correlation function decays within R_1, the behavior is interrupted after the point x_L (or x_R). Thus, no TLL behavior could be characterized under these conditions. For values of $V/t \sim U/t$, the corresponding power law decay was still observed for certain band fillings. The oscillatory component of the correlation function (see Eq. (6.1)) was observed for all cases. Although the $2k_F$-oscillations could only be fitted for $n \leq 0.6$. We can conclude that the TLL is not a universal feature for one-dimensional systems.

For systems at half-filling, which are Mott insulators, we calculated spectral density functions at different momenta q using the Lanczos vector method. In the high-frequency regime, the method (even if increasing the number of Lanczos vectors) does not seem to render accurate information. In that case, using the correction vector method is a better option. The optical conductivity for heterostructure I was also calculated using the correction vector method.

Conclusions

Finding parameters to tune the physical properties of electronic devices is a key aspect of the materials research. In this thesis, we have presented examples of the results of the last decades in the fabrication of nanoscopic quasi-one-dimensional systems. Carbon nanotubes, semiconducting quantum wires and organic molecules have become helpful laboratories to investigate a wide range of low-dimensional quantum effects. And while the properties of homogeneous one dimensional systems (even with disorder) are relatively well-understood, very little is known about the properties of strongly interacting inhomogeneous systems. The physics of one-dimensional systems, in the homogeneous low-energy regime, is described by the Tomonaga-Luttinger liquid model for which the relevant degrees of freedom are no longer the single particle electronic states, whose spectral weight vanishes at the Fermi surface. Instead, collective spin and charge density waves appear propagating with different group velocities. Another prediction of this model is the algebraic decay of the correlation functions, which exhibits a power-law decay specified only by the Tomonaga-Luttinger parameter K_λ. Both spin-charge separation and the algebraic decay of the correlation function are benchmarks of the Tomonaga-Luttinger liquid. The Tomonaga-Luttinger liquid can be exactly solved using the bosonization method, which was explained in this thesis. Such method states the equivalence between fermionic and bosonic degrees of freedom in the low-energy regime of one-dimensional systems. A boson representation of the problem allowed for an easier diagonalization of the Hamiltonian of the system including interactions.

In this thesis we have investigated static and dynamic properties of low-dimensional homogeneous and inhomogeneous systems (which we also called heterostructures). We described how junctions between different types of atoms influence the variation in space of the density-density correlation function. The heterostructures can be seen as unions of homogeneous systems with different coupling constants. The numerical analysis showed that a slow variation of the on-site Coulomb potential, as the one for heterostructures I and II, does not affect the decay of the density-density correlation function. In these heterostructures, the leading term predicted by the Luttinger liquid, i.e., the power-law decay, was observed for band filling smaller than half-filling (which must be considered apart). The systems also presented an oscillatory behavior in the density-density correlation function. But only for certain values of the band-filling, namely $0.1 \leq n < 0.6$, they matched the expected $2k_F$-oscillations of the charge density. A different behavior was found when introducing a scattering potential V at the junctions between the homogeneous sectors, as it was done for heterostructure III. In this case, the density-density correlation function depends strongly on the height of the potential barrier. After a threshold value, the decay of the correlation function is abruptly interrupted and is not longer possible to describe the behavior in terms of a Luttinger liquid. However, for $V \sim t$, the Luttinger liquid behavior was observed with $0.3 \leq n \leq 0.6$. Our findings show that the Tomonaga-Luttinger liquid is not a universal feature for one-dimensional systems. Similar systems were investigated where the on-site Coulomb potential was turned on and off over the subregions [38]. For such systems an effective exponent, $K_c^* = f(K_{1,c}, K_{2,c})$, was calculated considering, for example, two subchains which were assumed as independent, homogeneous Luttinger liquids.

We also considered systems at half-filling, which are no longer Luttinger liquids but Mott insulators, with a gap in the charge spectrum. We calculated the spectral density for heterostructure I, finding peaks at positions which can be identified with the energy dispersion relation for a Hubbard chain. Measurements of optical conductivity were done

on both homogeneous Hubbard chains and heterostructure I, finding for the homogeneous regime results that match those given in [11].

The systems were investigated using the density-matrix renormalization group, a method which has been particularly developed to study low-dimensional systems. Extensions of this method, such as the Lanczos vector method and the correction vector method allow for calculation of dynamic properties. Further work remains to be done concerning transport properties also at temperatures different from zero, which are significant in the designing and fabrication of properly tunable electronic devices.

List of Figures

Bibliography

[1] A pedagogical review on the subject is the collection of articles on carbon nanotubes by P. McEuen, P. Schönenberger, H. DAi and Walt der Heer-R. Martel on Physics World, June 2000. [18]

[2] A. Abrikosov, L. Gorkov, and I. Dzyaloshinski, *Methods of quantum field theory in statistical physics*, Dover Publications, INC., New York, 1975. [71]

[3] N. W. Ashcroft and N. D. Mermin, *Solid State Physics*, Saunders College Publishing, Philadelphia, 1976. [51]

[4] H. Bethe, *Zur theorie der metalle. i. eigenwerte und eigenfunktionen der linearen atomkette*, Zeitschrift f. Physik, 71 (1931), p. 205. [51]

[5] D. S. Bethune, C. H. Klang, M. S. de Vries, G. Gorman, R. Savoy, J. Vazquez, and R. Beyers, *Cobalt-catalysed growth of carbon nanotubes with single-atomic-layer walls*, Nature, 363 (1993), p. 605. [14, 15, 103]

[6] M. Bockrath, D. H. Cobden, J. Lu, A. G. Rinzler, R. E. Smalley, L. Balents, and P. L. McEuen, *Luttinger-liquid behavior in carbon nanotubes*, Nature, 397 (1999), p. 598. [18, 103]

[7] C. Bourbonaiss and D. Jérome, *Electronic confinement in organic metals*, Science, 281 (1998), p. 1155. [22, 23, 104]

[8] M. Dresselhaus, G. Dresselhaus, and A. Jorio, *Unusual properties and structure of carbon nanotubes*, Annu. Rev. Mater. Res., 34 (2004), p. 247. [18]

[9] S. Ejima, F. Gebhard, and S. Nishimoto, *Tomonaga-Luttinger parameters for doped Mott insulators*, 70 (2005), p. 492. [93, 99]

[10] V. J. Emery, *in Highly Conducting One-Dimensional Solids*, Plenum, New York, 1979. [31, 33]

[11] F. H. L. Esler, H. Frahm, F. Göhman, A. Klümper, and V. E. Korepin, *The one-dimensional Hubbard model*, Cambridge University Press, United Kingdom, 2005. [97, 102]

[12] T. Giamarchi, *Correlation Functions of One-Dimensional Quantum Sytems*, vol. 39, 1989. [49]

[13] ——, *Quantum physics in one dimension*, Oxford University Press, New York, 2004. [13, 45]

[14] F. D. M. Haldane, *'Luttinger Liquid Theory' of one-dimensional quantum fluids:i*, J. Phys. C: Solid State Phys., 14 (1981), p. 2585. [27, 41, 45]

[15] K. Hallberg, *Density-matrix algorithm for the calculation of dynamical properties of low-dimensional systems*, Phys. Rev. B, 52 (1995). [69, 74]

[16] T. Hand, *Finite-size effects in a one-dimensional Kondo Box*, PhD thesis, Universität Bonn, 2006. [73]

[17] S. IIJIMA, *Helical microtubules of graphitic carbon*, Nature, 354 (1991), p. 56. [14, 15, 103]

[18] S. IIJIMA AND T. ICHIHASHI, *Single-shell carbon nanotubes of 1-nm diameter*, Nature, 363 (1993), p. 603. [14]

[19] Y. A. IZYUMOV AND Y. N. SKRYABIN, *Statistical Mechanics of Magnetically Ordered Systems*, Consultans Bureau, New York, 1988. [51, 56]

[20] E. JECKELMANN, F. GEBHARD, AND F. ESSLER, *Optical conductivity of the half-filled Hubbard chain*, Phys. Rev. Lett., 85 (2000), p. 3910. [97]

[21] D. JÉROME, A. MAZAUD, M. RIBAULT, AND K. BECHGAARD, *Superconductivity in a synthetic organic conductor:* $(TMTSF)_2PF_6$, J. Physique Lett., 41 (1980), p. 95. [22]

[22] D. KAUFMAN, Y. BERK, B. DWIR, A. RUDRA, A. PALEVSKI, AND E. KAPON, *Conductance quantization in V-groove quantum wires*, Phys. Rev. B, 59 (1999). [22, 104]

[23] E. LEVY, A. TSUKERNIK, M. KARPOVSKI, A. PALEVSKI, B. DWIR, E. PELUCCI, A. RUDRA, E. KAPON, AND Y. OREG, *Luttinger-liquid behavior in weakly disordered quantum wires*, Phys. Rev. Lett., 97 (2006), p. 196802. [22]

[24] E. LIEB AND F. WU, *Absence of Mott transition in an exact solution of the short-range, one-band model in one dimension*, Phys. Rev. Lett., 20 (1968), p. 1445. [51, 52, 82, 99]

[25] ——, *The one-dimensional Hubbard model: A reminiscence*, arxiv:cond-matt/0207529v2, (2002). [52]

[26] J. M. LUTTINGER, *An exactly soluble model of a many-fermion system*, J. Math. Phys., 4 (1963), p. 1154. [27]

[27] R. M. NOACK AND S. R. WHITE, *in Density Matrix Renormalization: A New Numerical Method in Physics*, vol. 528, Springer, Lecture Notes in Physics, Berlin, 1999. [61]

[28] L. PFEIFFER, H. L. STORMER, K. BALWDIN, K. WEST, A. GOÑI, A. PINCZUK, R. ASHOORI, M. DIGNAM, AND W. WEGSCHEIDER, *Cleaved edge overgrowth for quantum wire fabrication*, J. Cryst. Growth, 127 (1993), p. 549. [19]

[29] Y. SAAD, *Iterative methods for sparse linear systems*, PWS Publishing Company, Boston, 1995. [65, 77]

[30] K. SCHÖNHAMMER, *Interacting fermions in one dimension: The Tomonaga-Luttinger model*, arxiv:cond-matt/9710330v3, (1997). [27, 41]

[31] H. J. SCHULZ, *Hubbard chain with reflecting ends*, J. Phys. C: Solid State Phys., 18 (1985), p. 581. [57]

[32] ——, *Correlation exponents and the metal-insulator transition in the one-dimensional Hubbard model*, Phys. Rev. Lett., 64 (1990), p. 2831. [93, 99]

[33] ——, *Interacting fermions in one dimension: From weak to strong correlation*, arxiv:cond-matt/9302006v1, (1993). [27]

[34] ——, *The metal-insulator transition in one dimension*, arxiv:cond-matt/9412036v1, (1994). [81]

[35] A. Schwarz, M. Dressel, G. Grüner, V. Vescoli, L. Degiorgi, and T. Giamarchi, *On-chain electrodynamics of metallic $(tmtsf)_2x$ salts: Observation of Tomonaga-Luttinger liquid response*, Phys. Rev. B, 58 (1998), p. 1261. [23, 25, 104]

[36] D. Senechal, *An introduction to bosonization*, arxiv:cond-matt/9908262v1, (1999). [27, 35]

[37] H. Shiba, *Magnetic susceptibility at zero temperature for the one- dimensional Hubbard model*, Phys. Rev. B, 6 (1972), p. 930. [83, 99, 105]

[38] J. Silva-Valencia, E. Miranda, and R. R. dos Santos, *Luttinger liquid superlattices: Realization of gapless insulating phases*, Phys. Rev. B, 65 (2002), p. 115115. [101]

[39] M. Sing, U. Schwingenschlögl, R. Claessen, P. Blaha, J. M. P. Carmelo, L. M. Martelo, P. D. Sacramento, M. Dressel, and C. S. Jacobsen, *Electronic structure of the quasi-one-dimensional organic conductor TTF-TCNQ*, Phys. Rev. B, 68 (2003), p. 125111. [94]

[40] B. Sólyom, *The Fermi gas model of one-dimensional conductors*, Adv. Phys., 28 (1978), p. 201. [27]

[41] M. Stone, ed., *Bosonization*, World Scientific, London, 1994. [35]

[42] S. W. T. Kühner, *Dynamical correlation functions using the density matrix renormalization group*, Phys. Rev. B, 60 (1999), p. 335. [69, 76, 77]

[43] S. Tarucha, T. Honda, and T. Saku, *Reduction of quantized conductance at low temperatures observed in 2 to 10μm-long quantum wires*, Solid State Communications, 94 (1995), p. 413. [22]

[44] K. Thomas, J. Nicholls, A. Appleyard, M. Simmons, M. Pepper, D. Mace, W. Tribe, and D. Ritchie, *Interaction effects in a one-dimensional constriction*, Phys. Rev. B, 58 (1998), p. 4846. [21]

[45] S. Tomonaga, *Remarks on Bloch's method of sound waves aplied to many-fermion problems*, Prog. Theor. Phys., 5 (1950), p. 544. [27]

[46] J. Voit, *One-dimensional Fermi liquids*, Rep. Prog. Phys., 57 (1994), p. 977. [27]

[47] J. von Delft and H. Schoeller, *Bosonization for begginers - refermionization for experts*, Ann. Phys. (Leipzig), 27 (1998), p. 225. [27]

[48] M. Walther, E. Kapon, J. Christen, D. Hwang, and R. Bhat, *Carrier capture and quantum confinements in GaAs/AlGaAs quantum wire lasers grown on V-grooved substrates*, Appl. Phys. Lett., 60 (1992), p. 521. [21, 104]

[49] S. R. White, *Density matrix formulation for quantum renormalization groups*, Phys. Rev. Lett., 69 (1992), p. 2863. [61, 63]

[50] ——, *Density-matrix algorithms fo quantum renormalization groups*, Phys. Rev. B, 48 (1993), p. 10345. [61]

[51] S. R. White and R. M. Noack, *Real-space quantum renormalization groups*, Phys. Rev. Lett., 68 (1992), p. 3487. [62]

[52] K. G. WILSON, *The renormalization group: Critical phenomena and the Kondo problem*, Rev. Mod. Phys., 47 (1975), p. 773. [61]

[53] A. YACOBY, H. STORMER, N. WINGREEN, L. PFEIFFER, K. BALWDIN, AND K. WEST, *Nonuniversal conductance quantization in quantum wires*, Phys. Rev. Lett., 77 (1996), p. 4612. [20, 103]

[54] Z. YAO, H. POSTMA, L. BALENTS, AND C. DEKKER, *Carbon nanotube intramolecular junctions*, Nature, 402 (1999), p. 273. [18, 103]

Acknowledgments

Many people deserve thanks for their contributions to this thesis: First of all I would like to thank my supervisor Hartmut Monien for suggesting such a challenging and interesting topic and making this thesis possible. His deep insight into physics, and his interest in history and other cultures always amazed me and taught me a lot. His constant care for the students is a laudable quality. I would also like to thank Herbert Dreiner for taking care of the review of this thesis. I would like to thank Xiaobin Cao, Hunpyo Lee, Gang Li, and Mauricio Trujillo Martínez for the pleasant working atmosphere. I thank Sigi Guertler, Mauricio Trujillo Martínez, and Charlie for reading this thesis and making helpful commentaries. Patricia Zündorf and Dagmar Fassbender deserve special thanks for being always willing to solve bureaucratic issues. I thank Werner Grabasch for the nice conversation every time I dropped by to pick up stationery, and Michaela Mühl for her unweary help in finding the needed literature for this thesis and for her book recommendations. Thanks also to Andreas Wisskirchen, for taking care of everything related to the computer; and to Cornelia Zapf, who had always more than a couple of minutes for me. I would like to thank Tommy Vince for the thrilling chess matches. I am also deeply grateful to Anne Welsing and Detlef Briesen, who shared so much with me. I thank Paz León Zamudio, José C. Arredondo Ruiz, Charlie, and Claudia Briones Jurado for their constant support, patience and care. And last but not least, I thank the CONACyT-DAAD cooperation project that supported financially my stay in Germany.

Yesenia Arredondo León

Agradecimientos

Muchas son las personas que contribuyeron a esta tesis. En primer lugar quiero agradecer a mi asesor Hartmut Monien por haberme sugerido un tema tan fascinante y haber hecho esta tesis posible. Su profunda visión de la física, y su interés por la historia y culturas diversas, me sorprendieron y enseñaron mucho. Su atención constante hacia los estudiantes es loable. Quisiera agradecer también a Herbert Dreiner por la revisión de este trabajo. Agradezco a Xiaobin Cao, a Hunpyo Lee, a Gang Li y a Mauricio por la atmósfera de trabajo agradable. Agradezco a Sigi Guertler, a Mauricio Martínez Trujillo y a Charlie por la lectura de esta tesis y sus comentarios acertados. Patricia Zündorf y Dagmar Fassbender merecen mi muy especial agradecimiento por su disposición para resolver asuntos burocráticos. Agradezco a Werner Grabasch por su conversación agradable cada vez que lo visitaba para proveerme de papelería, y a Michaela Mühl por su incansable ayuda para encontrar la literatura adecuada para mi trabajo. Agradezco a Andreas Wisskirchen por ocuparse de todo lo relacionado con el sistema de cómputo; y a Cornelia Zapf, que siempre tuvo tiempo para mis preguntas. Quisiera también agradecer a Tommy Vince por los emocionantes partidos de ajedrez. Estoy profundamente agradecida con Anne Welsing y Detlef Briesen, que generosos compartieron tanto conmigo. Agradezco a Paz León Zamudio, a José C. Arredondo Ruiz, a Charlie y a Claudia Briones Jurado por su apoyo ininterrumpido, por su paciencia y atención. Y por supuesto, agradezco al proyecto de cooperación CONACyT-DAAD que financió mi estancia en Alemania.

Yesenia Arredondo León